UNIVERSITY OF OKLAHOMA

GRADUATE COLLEGE

APPLICATION AND LIMITATIONS OF SEISMIC ATTRIBUTES ON 2D RECONNAISSANCE SURVEYS

A THESIS

SUBMITTED TO THE GRADUATE FACULTY

in partial fulfillment of the requirements for the

Degree of

MASTER OF SCIENCE

By

BRYCE HUTCHINSON
Norman, Oklahoma
2016

APPLICATION AND LIMITATIONS OF SEISMIC ATTRIBUTES ON 2D RECONNAISSANCE SURVEYS

A THESIS APPROVED FOR THE
CONOCOPHILLIPS SCHOOL OF GEOLOGY AND GEOPHYSICS

BY

_____
Dr. Kurt Marfurt, Chair

_____
Dr. John D. Pigott

_____
Dr. Roger Slatt

To my mother and father, you are each so unique. Thank you for guiding me to become who I am, where I am, today.

Acknowledgements

I would not have completed this research, nor learned nearly as much as I have throughout this program, without the help and guidance of the students and professors that I am lucky to be around. First and foremost, Dr. Marfurt's support was invaluable. His positivity helped me through frustrating times, and his creativity sparked many ideas in my work. My committee members, Dr. John Pigott and Dr. Roger Slatt, offered helpful advice and support whenever I required. Dr. Brad Wallet has been supportive throughout the process and has given much valuable advice. Conversations with my peers provided many ideas for improvement in my research. Their willingness to discuss and explain complex ideas has made a substantial impact on my growth as a geoscientist. Fangyu Li, Abdulmohsen Alali, Lennon Infante, Joseph Snyder, Megan Gunther, Tao Zhao, Jie Qi, Tobi Olorunsola, Tengfei Lin, Rae Jacobsen, Gabriel Machado, Thang Ha, Alexander Besov and many others all took part in enlightening discussions on different topics. I would also like to thank my roommates Niles Wethington and John Hornbuckle who helped me practice my thesis defense numerous times and offered valuable critiques.

Without the individuals mentioned above, and many others, I would not have made near as much progress as I did on this work. Their help, guidance, ideas, questions, and critiques continually motivated me to better myself and my project.

Table of Contents

List of Figures

Abstract

Reconnaissance surveys of 2D seismic data are acquired before most 3D seismic surveys to define the area of interest and regional trends. While seismic attributes are routinely applied to 3D data, they are less commonly applied to 2D data. Today's low commodity prices call for the utilization of all available data. To quantify the value of 2D attribute analysis I use attributes computed from a 3D survey covering the same area as the baseline or ideal result. Using a 2D seismic survey overlying a 3D volume offshore New Zealand in the Taranaki Basin, picked key horizons on 2D and 3D data, which were in turn used to create surfaces and isochrons. Candidate attributes included RMS amplitude, instantaneous frequency, instantaneous phase, similarity, curvature, and spectral components.

The Taranaki Basin is a Cretaceous-aged failed rift basin with a complex structural history. A poststack data conditioning workflow is constructed for 2D and 3D to suppress crosscutting migration artifacts, and sharpen discontinuity features of the structurally complicated environment. I used concepts of structural geology to validate these discontinuity features as faults rather than organized artifacts. Structure-oriented filtering deteriorates on 2D lines where out-of-the plane reflectors overprint features of interest.

I also noted an underreported observation that edge-preserving structure-oriented filtering can introduce frequencies that fall beyond the limits of the recorded seismic data.

On 2D vertical seismic lines, in the dip direction single trace attributes such as spectral components, RMS amplitude and instantaneous attributes provide images comparable to those computed from 3D. Geometric attributes computed from 2D dip lines

render useful images of apparent dip and apparent (or Euler) curvature while similarity maps the apparent dip of faults and channel edges.

Generating useful attribute maps from 2D data is more problematic, with major limitations of both software flexibility and the author skill. While I can generate good quality time structure, isochron, and horizon curvature maps from 2D data, I believe that effective interpolation of shorter wavelength anomalies as mapped by RMS amplitude and spectral components requires Kriging guided by a variogram constructed from the time-structure maps.

Motivation

In 1997, Bill Aylor of Amoco marveled at the impact 3D seismic data had on exploration success rates. One particularly striking number is the drilled success rate of oil wells during 1990-1997; with 3D seismic data the success rate was 37%, while without 3D seismic data a mere 3% (Brown, 2003). Aylor's sentiment highlights the value that the industry, as a whole, places on 3D seismic data, and rightfully so.

However, the value of 2D seismic data cannot be forgotten. Aylor (Brown, 2003) asserts that during the 1970s and 1980s 2D methods "seemed to be highly viable and capable". My goal is to determine if this viability extends to the application of modern attributes. During times of industry slowdown, all available data must be utilized in interpretation and development processes. Today, 2D reconnaissance surveys are acquired over large areas before most 3D seismic surveys in order to define an area of interest. Additionally, substantial amounts of legacy 2D seismic lines that were shot and shelved in favor of 3D surveys are available.

Geologic interpretation from 2D seismic data is often expected to be limited, which is the primary reason for the industry dependence on 3D data. However, there is significant information to be garnered from 2D data. The question is how much interpretative detail can be gathered from 2D seismic data. In 1992, Bahorich and Bridges tested the effectiveness of mapping attributes along surfaces from 2D data with the intent of better visualizing patterns related to lithology and fluid content. Bahorich and Bridges term this work Seismic Sequence Attribute Mapping (SSAM); they trumpet the value of this powerful and low cost exploration and development tool.

Bahorich and Bridges (1992) utilize attributes such as amplitude, frequency, and phase. These type of attributes are commonly referred to as “single trace attributes”, and examine properties of the seismic data one trace at a time. In contrast, “multi-trace attributes”, compare the amplitude and phase behavior of adjacent traces. Similarity is an example of a multi-trace attribute. As Marfurt (2015) discusses, the library of both single and multi-trace attributes has continued to grow. Many attributes are available now that were not available when Bahorich and Bridges (1992) created their 2D data maps, while other attributes have seen an improvement in calculation methods; visualization methods for displaying these attributes also continues to improve (Chopra and Marfurt, 2006).

The computation, display, and interpretation of attributes computed from 2D data are more limited than those from 3D data. 2D data are not simply a slice through 3D data. While single trace attributes remain largely unchanged from 2D to 3D, attributes that involve dip calculations in 3 dimensions will be limited as well as attributes calculated in 3D windows.

Seismic resolution and migration algorithms also work differently in 2D and have different hurdles to overcome. While the resulting seismic image is displayed in only two dimensions, the reflection sources are not. Reflections from out of plane reflectors and diffractors are captured in the 2D seismic image, creating “sideswipe” in the 2D seismic that must be understood in order to avoid erroneous interpretation. Sideswipe energy can disrupt reflectors and make picking a horizon a challenging task. Also sideswipe can inject further problems into the migration algorithm applied on a 2D line, because there is not a correct place for the energy to be migrated. Migration

algorithms tend to move reflectors updip, however, in a 2D line the true updip direction is unknown so energy can often be placed incorrectly.

While an ever expanding attribute library can complicate any interpretation workflow, the effectiveness of attributes for interpretation of seismic data depends chiefly on understanding how attributes are computed and best practices for implementation.

I begin this thesis with a review of the geology in the study area. Then I explore some data quality issues that could cause variability between 2D and 3D seismic data. I follow that section by investigating some of the geologic features on vertical sections through seismic attributes then on surfaces created from these attributes. Next, the data conditioning workflow is covered in depth. Finally, I discuss my conclusions, and in the appendices detailed information on the calculation of attributes and seismic resolution can be found.

Geology of Pohokura

The greater part of the Taranaki Basin is located offshore the western coast of the North Island of New Zealand with a small extension onshore the North Island in the Taranaki Peninsula and the northernmost part of the South Island of New Zealand (Hansen and Kamp, 2004). According to New Zealand Petroleum and Minerals (NZPAM), the Taranaki basin spans a total area of 330,000 km^2. The basin was formed in the Late Cretaceous as a result of a failed rift event. Since the Cretaceous extension, the Taranaki Basin has experienced several phases of extension and compression, most notably Paleocene extension and Miocene compression. Further extension during the Pliocene allowed reactivation of normal faults. Overall, the Taranaki Basin can be characterized by down-faulted grabens with intervening basement horsts caused by a complex structural history.

A collision between New Zealand and the Pacific oceanic plate as early as the Late Eocene controls much of the geologic structure east of the prominent Cape Egmont fault zone seen in Figure 2. The Cape Egmont Fault Zone consists of steep normal to reverse faults. Some of the faults in Cape Egmont have significant offset of up to 2100 m (Palmer, 1985). In the Oligocene, the Taranaki basin experienced a period of rapid subsidence and a major transgression interpreted to be related to compression and uplift occurring outside the Taranaki basin to the east as a foreland basin was initiated (Crowley and Crocker, 1989).

During the early Miocene, thrusting occurred along the Taranaki Boundary Fault and more clastic sediment was shed to the west. Throughout the Miocene, compression continued and is expressed as inversion structures of previously formed extensional

faults and thrusting onshore. The Taranaki fault zone is comprised of a narrow zone of steep reverse faults that become nearly vertical and normal at depth.

A major marine transgression beginning in the Paleocene and continuing through the Miocene governs much of the stratigraphy of the Taranaki Basin. During the late Cretaceous-Paleocene, the Taranaki Basin area was of generally low relief with a gentle westward dip. At the beginning of the Eocene the sea began to transgress onto the landmass. Continued transgression occurred through the Eocene and Oligocene; by the early Miocene, the whole basin was below sea level in bathyal environments. This transgression took place in general from the northwest to southeast.

Reservoir intervals have been discovered in a variety of lithologies and depositional environments in the Taranaki basin including Pliocene turbidites and shelf sands, Oligocene fractured limestone, and Miocene channel levee overbank and lobe deposits. An overview of common Taranaki formations of the Miocene to Pliocene is presented below. Deposits of these ages are some of the most widely studied formations of the Taranaki Basin. Following the Late Miocene to Paleocene review, there is a review of each of the formations of interest used in this study.

Late Miocene to early Pliocene formations include the Manganui Formation, Mohakatino Formation, Moki Formation, Mount Messenger Formation, Ariki Formation, Manga Formation, and Giant Foresets Formation (Hansen and Kamp, 2004). Within the Taranaki basin, the Manganui Formation is composed of fine grained clastic sediments. These fine grained sediments bound coarser grained sandy submarine fan deposits. In some areas, the Manganui Formation is indistinguishable from the overlying Mohakatino formation and at these points is referred to as the (upper)

Manganui-Mohakatino formation. According to Hansen and Kamp (2004), the Manganui displays an arcuate profile in gamma ray logs with higher readings at the top and bottom of the formation, tying back to the earlier interpretation of finer grained sediments bounding coarse grained sediments. In seismic data, the top of the Manganui formation is defined by a high amplitude reflector that is referred to the U0SB horizon in completion reports. This horizon shows interesting geologic features such as channels and slump blocks that will be investigated further in both 2D and 3D seismic data.

Overlying the Manganui Formation is the Mohakatino Formation. This formation is composed mainly of tuff or volcaniclastic content. In general, volcaniclastic content decreases upwards in the formation. Gamma ray in the Mohakatino is linear to blocky, suggestive of massive sandstones throughout the formation. The base of Mohakatino Formation consistently shows a characteristic sharp dropoff in gamma ray values, leading to the wide use of this signature as a marker for the middle Miocene throughout the Taranaki Basin. Seismic data in the Mohakatino Formation is marked by bright consistent reflectors interpreted as volcanics as well as onlap onto these reflectors.

The Mangaa formation unconformably overlies the Mohakatino and upper Manganui formations. It is deposited below the Giant Foresets formation. Sandstone beds of the Mangaa formation are latest Miocene to Pliocene in age. Generally, the Mangaa formation is subdivided into two sandstone and mudstone packages. These beds are younger than the Mount Messenger and Moki formations and not consistently present throughout the basin. Some gamma ray logs, such as that in the Mangaa-1 well, show sandstone very clearly in a clean log. However, other instances of the Mangaa

show less clean gamma ray responses and are interpreted as amalgamated deposits of high density turbidity flows (Hansen and Kamp, 2004).

The Late Miocene Mount Messenger formation has been studied in detail at outcrop, well log, core, and seismic scales. At Pukearuhe Beach, about 40 km northeast of New Plymouth in the northeastern Taranaki Basin, expansive Miocene outcrops provide a ground truth for lithologic and stratigraphic study of Miocene formations of the Taranaki Basin. Studies of core, outcrop, and well data performed by Brown and Slatt (2002) as well as Rotzien et al. (2014) provide detailed sources for interpretation. Browne and Slatt break down the slope fan strata of the Mount Messenger Formation into three distinct facies. These facies are channel fill, proximal channel-levee and overbank, and distal channel-levee and overbank. Core samples of the channel fill facies are more mud-prone when compared to the other two facies. Proximal and distal channel-levee and overbank deposits can be differentiated from one another by the amount of siltstone and the flow regime. Distal channel-levee and overbank deposits have a higher siltstone component, and sandstone facies in distal channel-levee and overbank deposits exhibit ripple lamination, indicating a lower flow regime. Browne and Slatt consider overbank and channel-levee deposits higher reservoir quality rocks than channel fill primarily due to the high mud-content of channel fills.

Rotzien et al. (2014) delve deeper into the stratigraphic architecture of the Mount Messenger formation. Particularly, Rotzien et al. focus on the Upper Mount Messenger formation, they also performed their study at Pukearuhe Beach and focused on sedimentary structures, paleocurrent indicators, and stratigraphic architecture. In this work the Upper Mount Messenger Formation's lithologic composition is interpreted as

sandstone channels, tabular sandstones, mudstone channels, and interbedded mudstone. Mud and shale often isolate channels, as such the reservoir potential of this tabular sands is touted. These sands can have a large areal expanse, and communication between many thin well sorted sand units can create a large reservoir.

The Mount Messenger Formation is made up of density flows and associated architectural elements like channel levee systems and overbank deposits.
A major regression deposited submarine fan sediments of the Mount Messenger formation. This time coincided with the onset of major compressional tectonics associated with the development of inversion and thrust structures in the Taranaki Basin.

The youngest sediments of Pliocene to Pleistocene age are dominated by the Giant Foresets Formation. Giant Foresets is the basis of the modern slope and shelf. Giant Foresets can be identified by the formation's clinoform shaped, basinward-dipping character. These clinoforms are indicative of the progradation of the continental margin basinward during the Pliocene and Pleistocene. Thicknesses of the Giant Foresets are complicated by the Turi and Cape Egmont fault zones that bound the Taranaki basin.

Formations of interest

Three formation tops are used in the following research to evaluate the use of attributes on 2D seismic data. They are the Tikorangi Formation, Maui Formation, and Manganui (U0SB) Formation. Details have been given above on the Manganui Formation, and following is a review of some of the properties that govern the quality

of the seismic data representations of the Tikorangi Formation and Maui Formation, respectively.

The Tikorangi Formation is composed primarily of limestone with a basal sandstone layer, it is classified as a deep-water, bioclastic limestone. Tikorangi is named after a North Taranaki township of the same name. This fractured limestone can be a source of mud loss and is important for drillers in the area. It was not encountered in the Okoki-1 well, but an equivalent horizon is seen on seismic in the Pohokura-1. In Pohokura-1, the Tikorangi Formation is interpreted as a claystone grading to limestone. The limestone is brownish gray and argillaceous with 20-40% clay minerals.

The Maui sands are located within the Kapuni Group, a Paleocene to Eocene succession of sandstones, mudstones and coals. The Kapuni Group is seen in wide distribution across the Taranaki Basin. The Maui sands are a shallow marine formation, whose onshore equivalent is the coastal plain Mangahewa Formation. The Maui sandstone formation is targeted in the Pohokura-1 well for testing. A gross gas column of 130 m was recorded in the upper Maui C sands. Maui sands in the Pohokura-1 well are described as fine to coarse grained sandstone with minor claystone. The location of the well was in the Pohokura structure, which is an elongate feature with obvious hydrocarbon trap potential. Unfortunately however, the hydrocarbon accumulation was determined to be uneconomic. In Pohokura-1, the Maui Formation has a gross thickness of 700 m. It consists of interbedded sandstone, claystone, and siltstone. Predominantly the formation is sandstone with a net thickness of roughly 530 m. This number is estimated from the geologic description from the Pohokura-1 completion report.

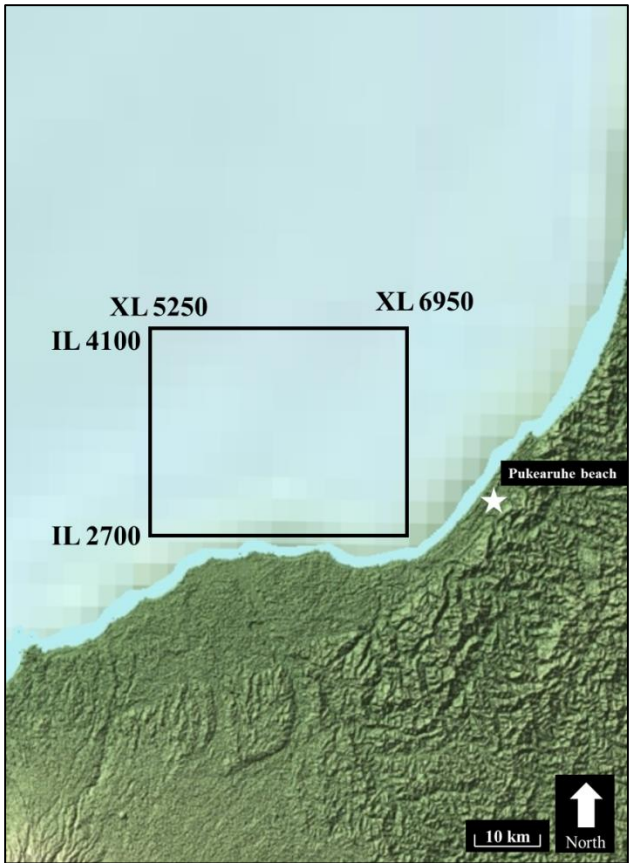

Figure 1. Map of Pohokura survey area, located offshore the west coast of the North Island of New Zealand. This area is just North of Mount Taranaki. Pukearuhe Beach is denoted by a white star and is the area of research for Browne and Slatt (2002).

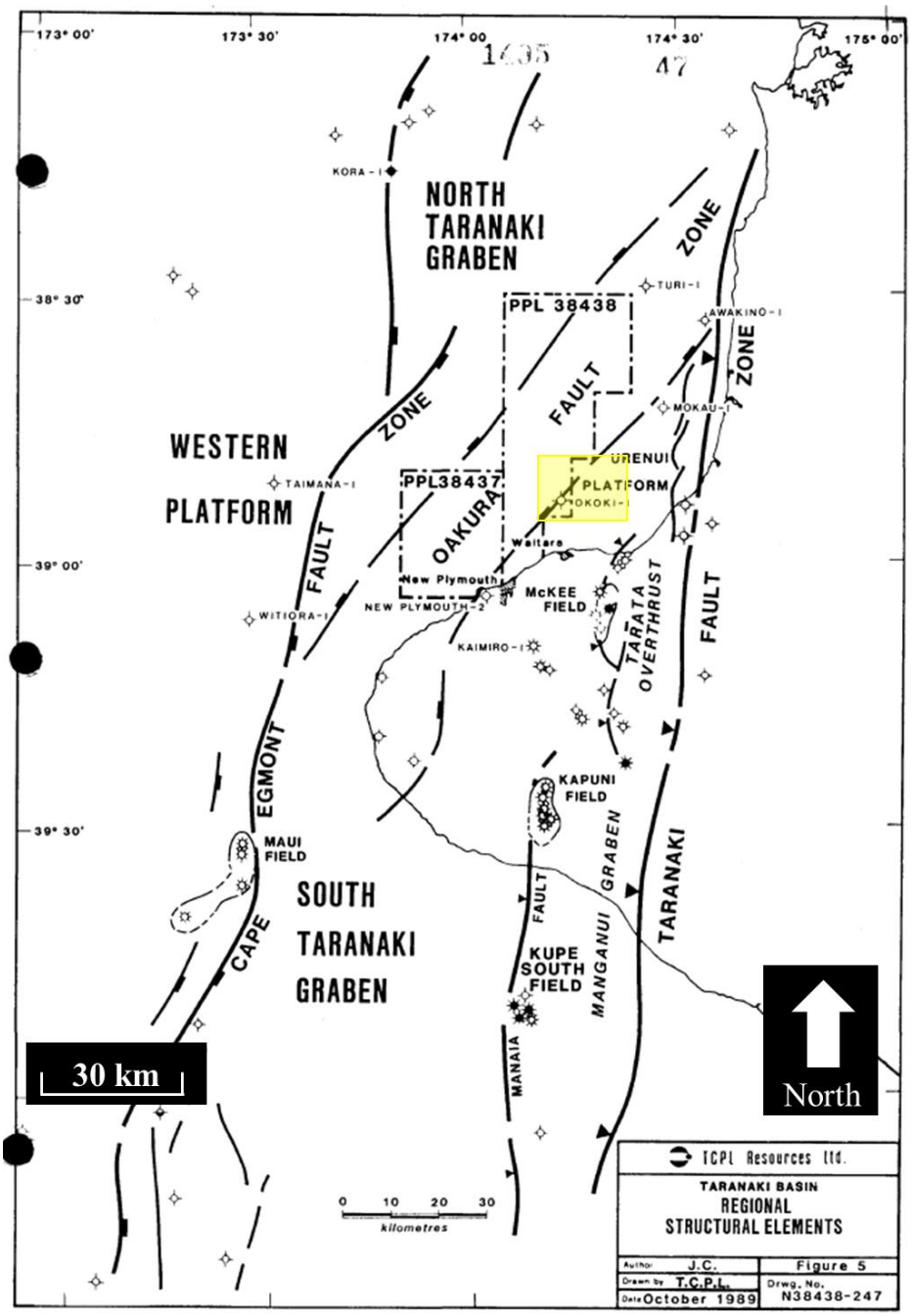

Figure 2. Regional structural elements of the Taranaki Basin. Area of interest highlighted in yellow. Crowley and Crocker, 1989.

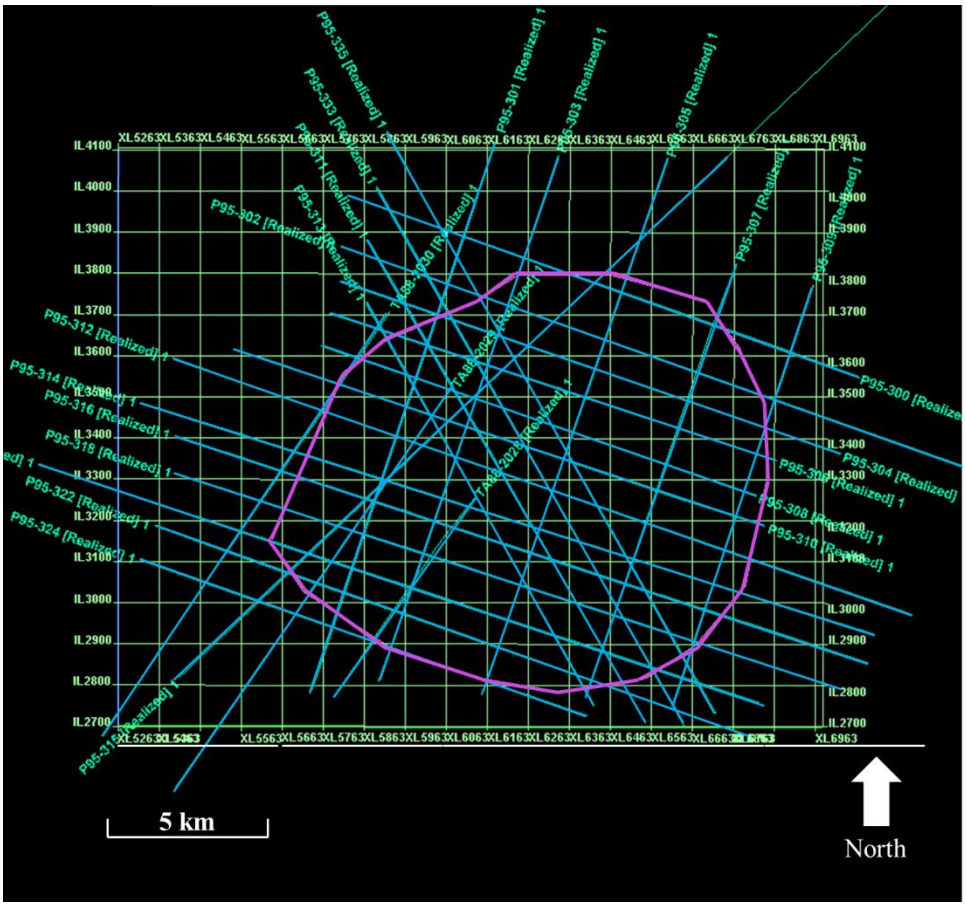

Figure 3. Pohokura 3D survey area outlined in green. Overlying 2D seismic lines are highlighted with cyan. The purple polygon is that used to create surfaces from 2D and 3D seismic.

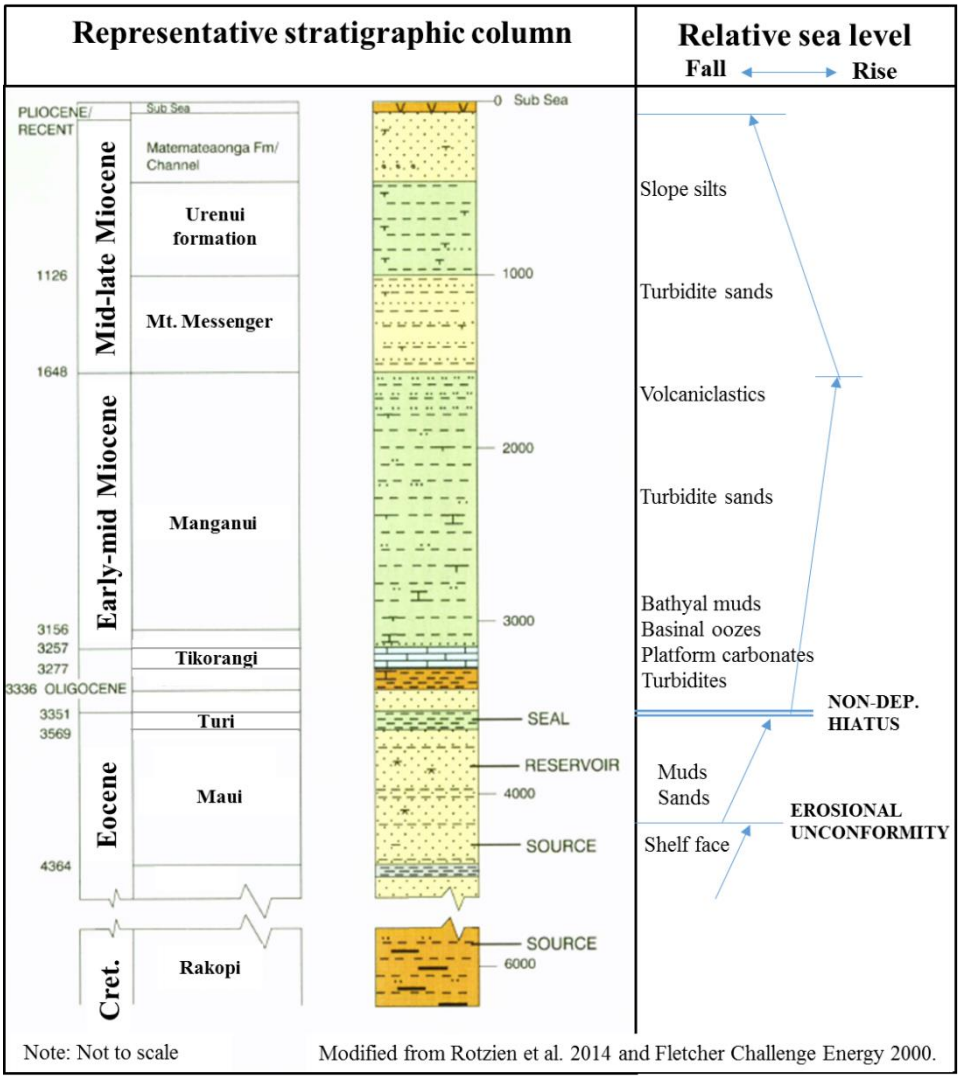

Figure 4. Representative stratigraphic column and sea level curve of the Taranaki Basin.

Data Quality Issues

The marine portion of the 3D seismic survey, which is the basis for this research, covers an area of 357 km^2 and is shown in Figure 3. Reservoir intervals in the Pohokura prospect area primarily produce gas and gas condensate (NZPAM, 2013).

Fold

Fold is the number of times a specific image point is imaged, more accurately, it is calculated as the number of source receiver midpoint that fall within an output bin. Equation 1 shows that fold is dependent on the number of receivers, spacing of receivers, and spacing of shotpoints. Fold varies throughout the data. At the edge of 3D seismic surveys there are less midpoints for the sources and receivers to image the subsurface, such that the fold is diminished.

The nominal fold of the P95 2D seismic data is 66. This fold was acquired with a 4000 m streamer cable and a shot spacing of 30.48 m. The 3D Pohokura survey has a nominal fold of 54, and a bin size of 12.5 m by 12.5 m. Pohokura also had a 4000 m streamer, however, its shot interval was 37.5 m.

$$Maximum\ Fold = \frac{1}{2}\left(Number\ of\ receiver\ stations * \frac{receiver\ station\ interval}{shotpoint\ interval}\right) \quad (1)$$

Migration Aperture and Energy placement

The migration aperture is defined in relation to the Fresnel Zone radius. Sun (1998) stated that the minimum migration aperture should be the interval where the difference between traveltimes of reflected and point-diffracted rays is equal to the duration of the recorded seismic pulse. Essentially, Sun states that for flat reflectors the minimum migration aperture is twice the Fresnel zone radius for the depth of the

formation of interest. The migration aperture becomes larger (and shifted) for dipping reflectors.

Coherent, shot-generated noise can be classified as either inline or sideswipe. Sideswipe is energy from a reflector or diffractor outside of the vertical plane of the 2D seismic line. If sideswipe is suspected in land seismic data, a “T” or “L” spread can be recorded to better image any sources of noise, as sideswipe would appear as regular linear noise in a line that is perpendicular to the source. No such crossline hydrophone arrays are possible in marine streamer data. In processing the seismic data, sideswipe events are partially suppressed by using an f-k filter. If the sideswipe is a diffraction, it will appear relatively flat in the f-k domain (Bancroft, 2009).

Figure 5 shows some of the limitations in migration. In particular, this figure shows a poorly imaged syncline around the dipping boundary of the Pohokura structure. This is likely the result of a migration velocity that was too high, unable to collapse the bowtie. A remnant of an out of plane diffractor also appears in Figure 5, where a coherent reflector overprints another clearly more continuous reflector. Validation fo these interpretations are provided through extraction of the equivalent seismic line from the 3D survey shown in Figure 6.

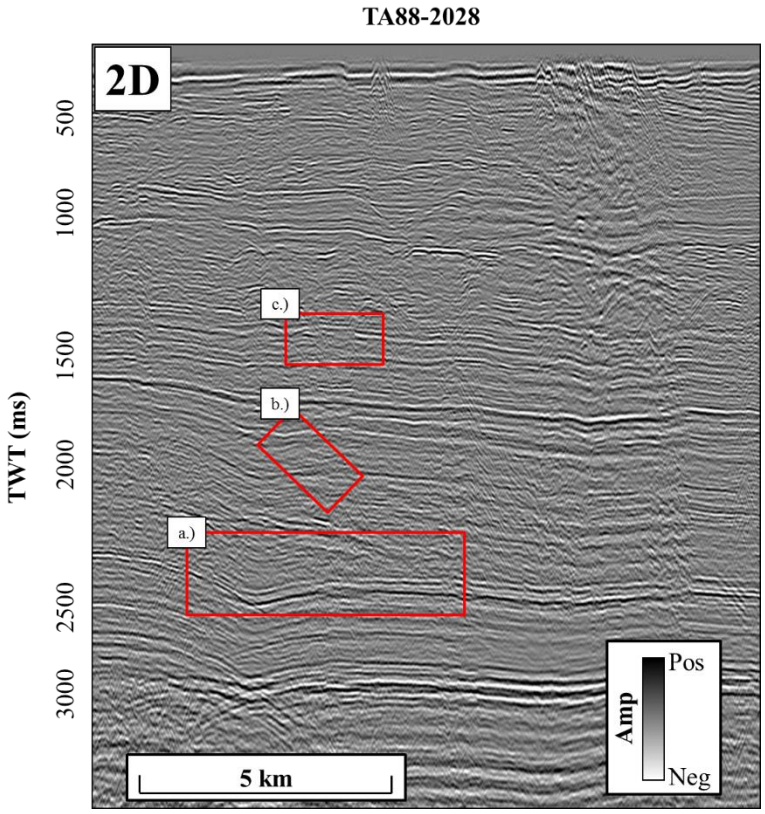

Figure 5. The effects of poor migration and out of plane energy are shown in line TA88-2029. (a) shows remnants of a bowtie associated with a syncline, suggesting the migration velocity was too high, perhaps the apparent velocity of the reflectors dipping out of the plane. In (b), out of plane energy overprints a reflector. (c) shows the tendency of a migration algorithm to move events updip, in this case making the reflector dip at a higher angle than it is seen on the 3D seismic data.

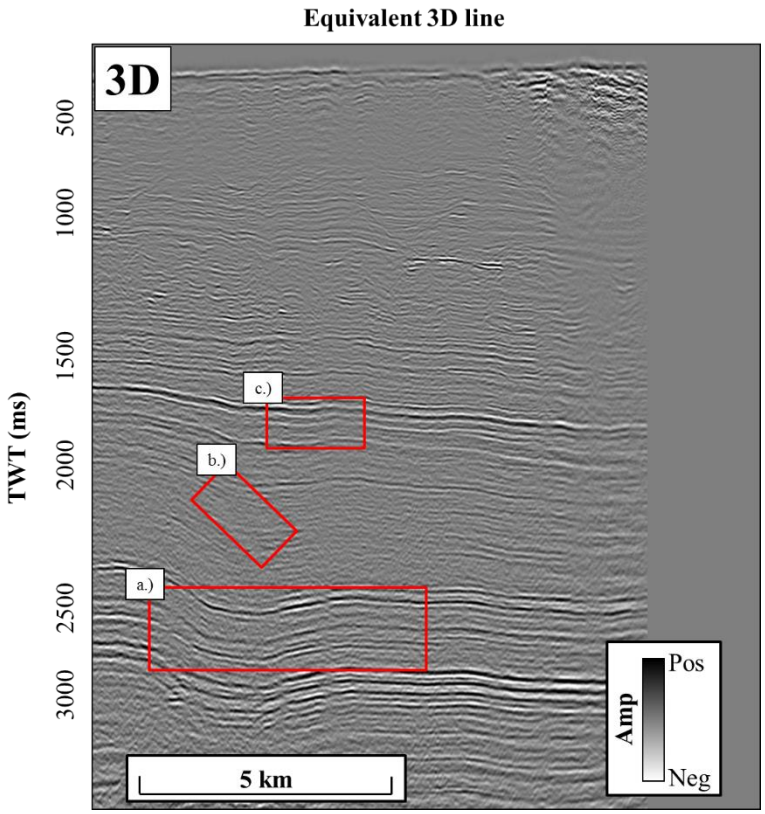

Figure 6. A line from the 3D seismic volume equivalent to the 2D line TA88-2028. In red rectangle numbered In (a) a correctly migrated reflector with collapsed diffractions from the dipping plane. Red rectangle (b) does not show any overprinted energy, and (c) shows the unexaggerated dip of a reflector.

Vertical section

Original seismic

Figure 7 shows a vertical slice through the original seismic data of 2D line P95-333. In this image there are a number of features including an interpreted MTC (mass transport complex) section in the red rectangle, reflector terminations indicated by the purple arrows, and a slump block highlighted in the yellow box. These geologic features have character preserved in both the 2D line P95-333 and the corresponding arbitrary line through the 3D data. However, the slump block in the yellow box in the 2D data appears more continuous than in in the 3D data in Figure 8. I attribute this continuity to be the result of the energy required to image the fault being scattered out of the plane, causing the slump block to appear more like a channel than a steep discontinuity feature.

2D line, P95-315 (Figure 9) shows the nose of the Pohokura structure in the left side of the image emphasized by the white box. The dip of this feature in 2D is subtler than the dip of the feature in Figure 10 which is extracted from the 3D seismic data. This change in dip occurs because the 2D line is slightly oblique to the true structure, so true dip is not imaged. An obvious, but often overlooked advantage of 2D data is also shown in comparison of the Figure 9 and Figure 10. 2D data can image areas outside of the 3D seismic cube. A more expansive area is imaged by 2D data and regional trends can be better understood from this expansive imaging.

Attributes of interest

According to Pigott et al. (2013), practical seismic attributes are indicative of quantitative or qualitative aspects which describe a seismic response in relation to an underlying geologic reality. With this in mind, attributes for this study were chosen on the basis of their usefulness in accentuating features from the geologic model not clearly interpretable in the original seismic data. In this case, those features include faults, stratigraphic terminations, and mass transport complexes.

I will review the results of the chosen attributes in two sections below, first in the vertical section, then in map view in the following chapter. These sections are single-trace (Appendix A) and multi-trace (Appendix B). Single-trace attributes were chosen under the hypothesis that their lack of spatial dependency would allow for the creation of a more detailed map. I calculated RMS amplitude, instantaneous frequency, instantaneous phase, and cosine of instantaneous phase on 2D and 3D seismic volumes for comparison. These attributes are chosen because they have known relationships to hydrocarbon accumulations as well as structural and stratigraphic features. Multi-trace attributes, with their trace by trace comparison, were thought to yield a less reliable image when attribute surfaces are created from 2D data because of the three dimensional trace comparison required in calculating these attributes. Energy ratio similarity and curvature are used for multi-trace attribute comparisons. These attributes convey structural relationships in the seismic data.

Single-trace attributes

RMS amplitude is shown in Figure 13 and Figure 14. The vertical sections from 2D and 3D may appear different upon initial glance, but that is an effect of amplitude

scaling. Amplitude of 2D seismic data is in the range of ± 40000, while 3D seismic amplitudes vary between ±2000. Overall, the RMS amplitude attribute creates a very similar image whether it is calculated from 2D or 3D data. Instantaneous frequency can also be useful, in mapping a hydrocarbon accumulation. Hydrocarbon accumulations cause attenuation of seismic waves and often exhibit low frequency anomalies below the accumulation where high frequencies have been attenuated (Taner, 2001). Figure 17 and Figure 18 display instantaneous phase. Not much information can be taken from these attributes, except for the understanding that they are very similar whether calculated on 2D or 3D seismic data. Figure 19 and Figure 20 show the cosine of instantaneous phase. This attribute is often used in seismic stratigraphic interpretation (Pigott et al., 2013). The cosine of phase causes terminations to appear more sharply and with the lack of amplitude information strong and weak reflections are displayed similarly.

Overall, single trace attributes do not add much insight beyond that taken from the original seismic data. However, these attributes do work very similarly when calculated on 2D data or 3D data, providing near identical images. Because they are only computed with regards to a single complex trace, they have no spatial dependency.

Multi-trace attributes

Vertical slices through multi-trace attributes provide information that can accelerate the interpretation. The energy ratio similarity computed from 2D data (Figure 21), shows two prominent fault features captured just as well as they are from the 3D data. Comparison of Figure 21 to Figure 22 also shows how crosscutting noise not present in the 2D data has negatively impacted the 3D seismic data. Crosscutting noise

is seen as an effect of improper migration. In the Pohokura survey the migration operator has failed to properly collapse diffractions, thus diffractions are still present in the data and overlap the reflectors and each other causing the crosscutting features. The presence of the crosscutting artifacts means that the inline and crossline dip volumes as well as subsequent volumes calculated using the inline and crossline dip, such as energy ratio similarity, could be contaminated by steeply dipping noise. One method used to combat the crosscutting noise was the implementation of a large vertical window size in the calculation of the dip and similarity volumes to statistically reduce the effects of the crosscutting noise. The large window size causes a loss of resolution in the energy ratio similarity volume. Relatively less crosscutting noise is shown in the 2D seismic data as compared with the 3D seismic data. The difference in noise can likely be attributed to different processing workflows. Comparing the 2D seismic data to an equivalent line from the 3D seismic volume, the image is much sharper and shows discontinuities sharper as well.

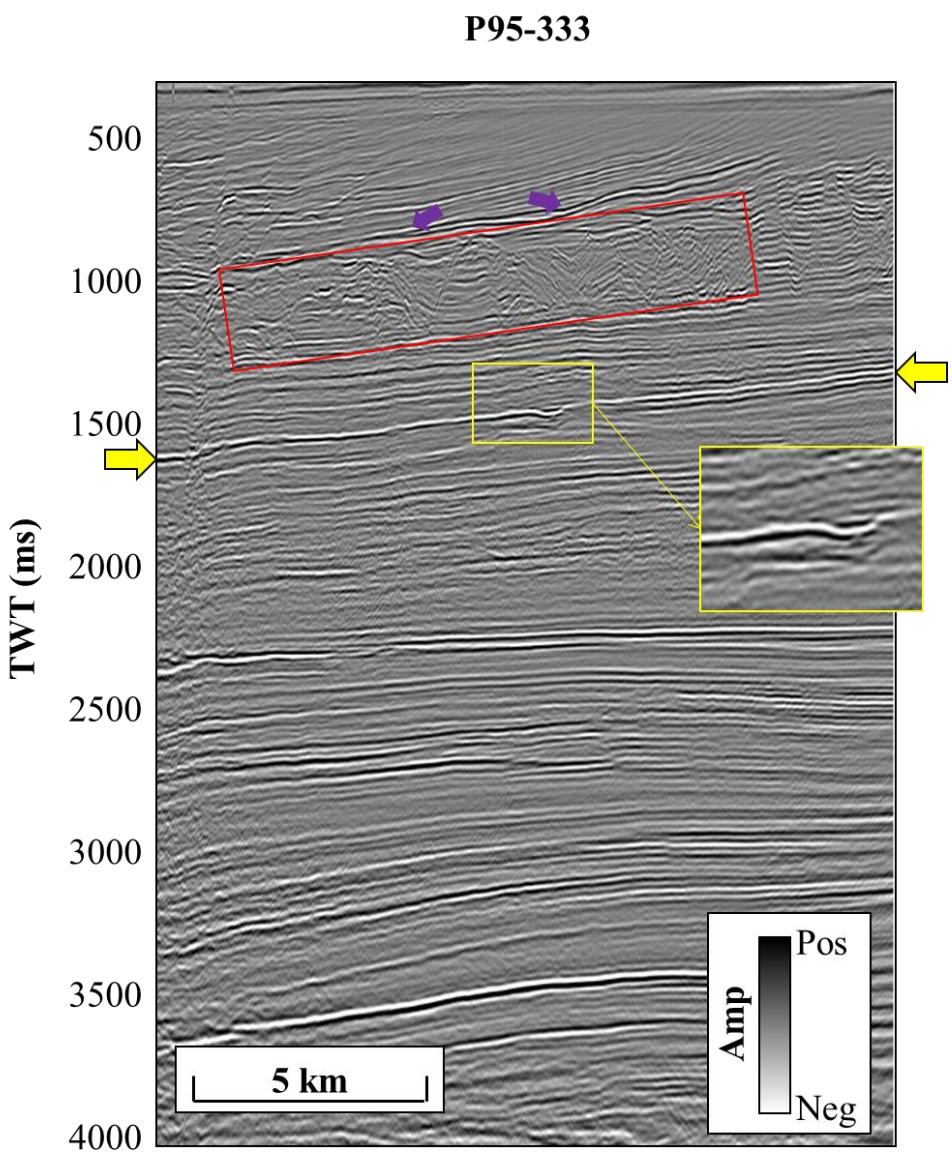

Figure 7. The original seismic data of 2D line P95-333. Yellow arrows indicate the U0SB surface. The yellow box highlights a discontinuity feature which appears more continuous in 2D than 3D. The red box shows a mass transport complex. Purple arrows show reflector terminations.

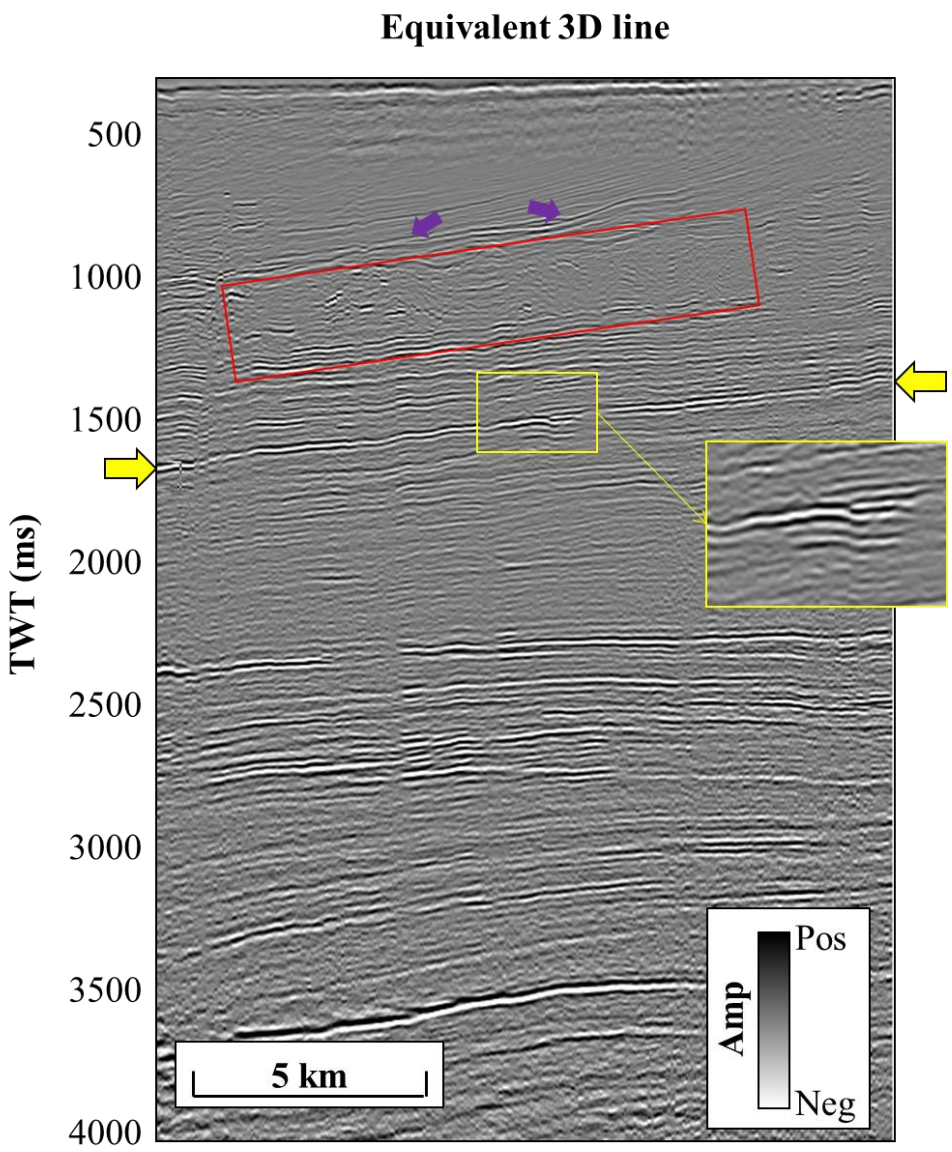

Figure 8. An "arbitrary" line through 3D seismic volume coincident with 2D line P95-333 showing the same CDP range. Yellow arrows indicate the U0SB horizon in this image, and the yellow rectangle shows a discontinuity feature that is imaged more sharply in 3D data than 2D.

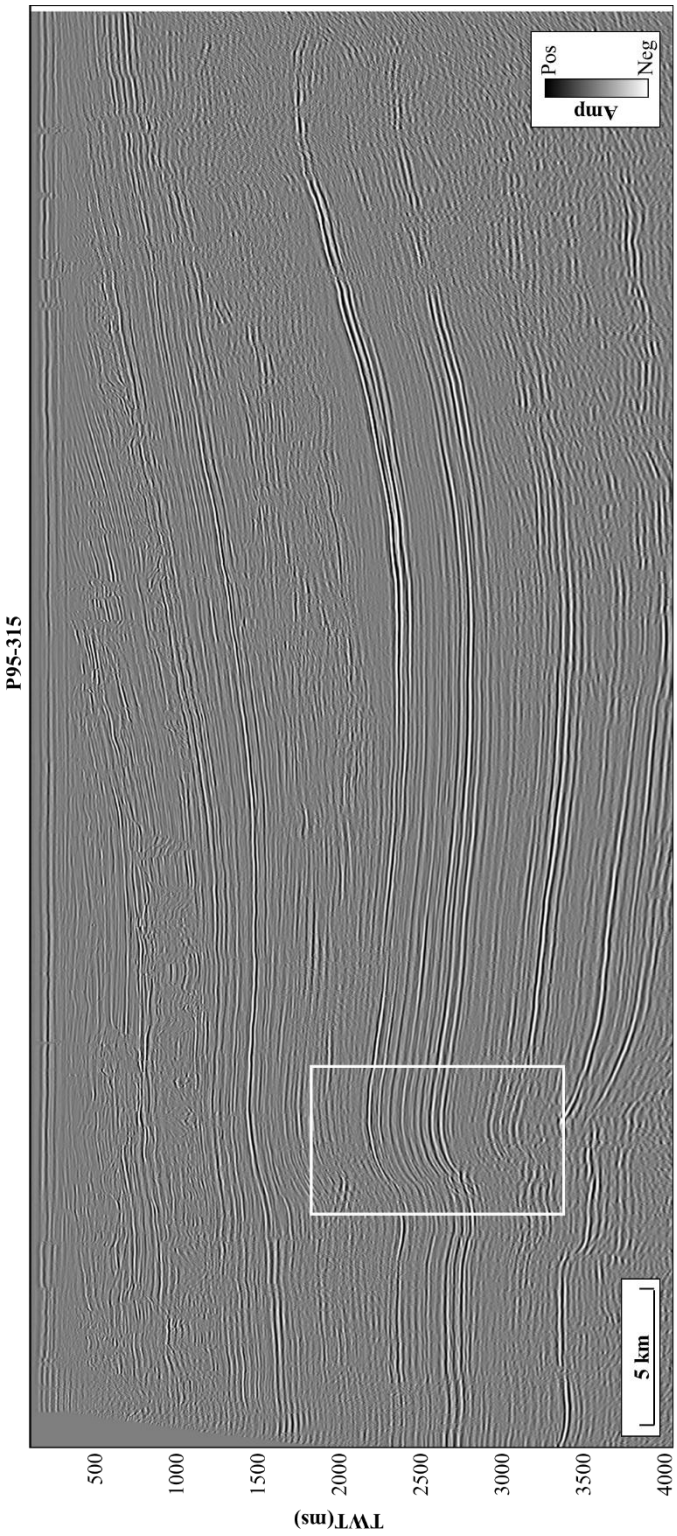

Figure 9. 2D line P95-313 shows an advantage of 2D seismic, the ability to better understand the regional structure beyond the limits of the 3D survey (shown in **Figure 10**). The white box highlights the dipping extent of the Pohokura structure. This apparent dip is not as steep as in the 3D data.

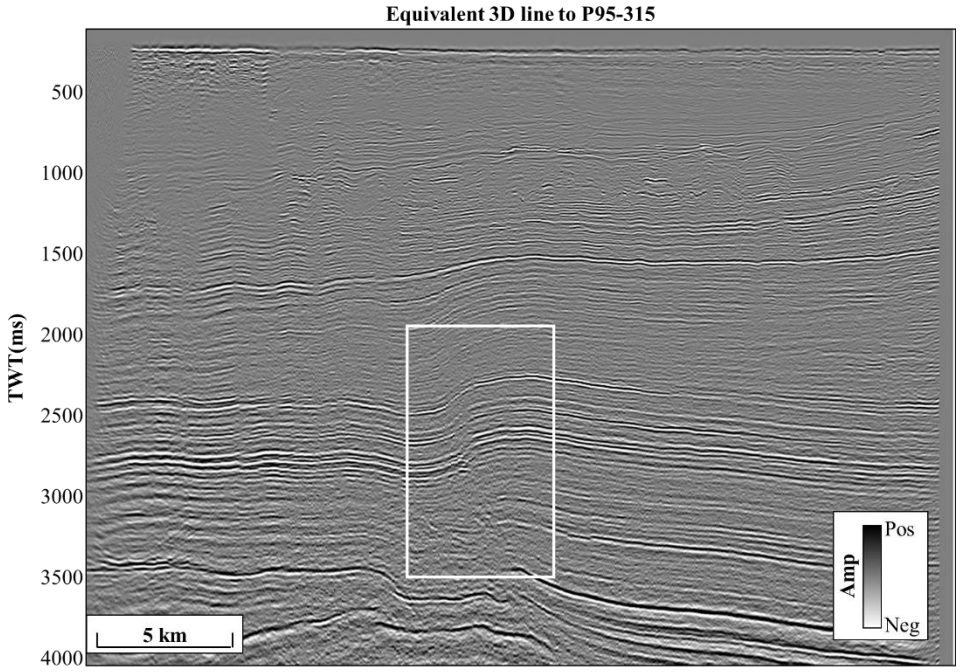

Figure 10. The equivalent arbitrary line, shown in **Figure 9**, through the 3D seismic data. Note the extent of the 3D survey is shorter than that of the 2D line. The white box highlights the dip, which is higher in 3D and likely more accurate than 2D due to the wide azimuth of coverage.

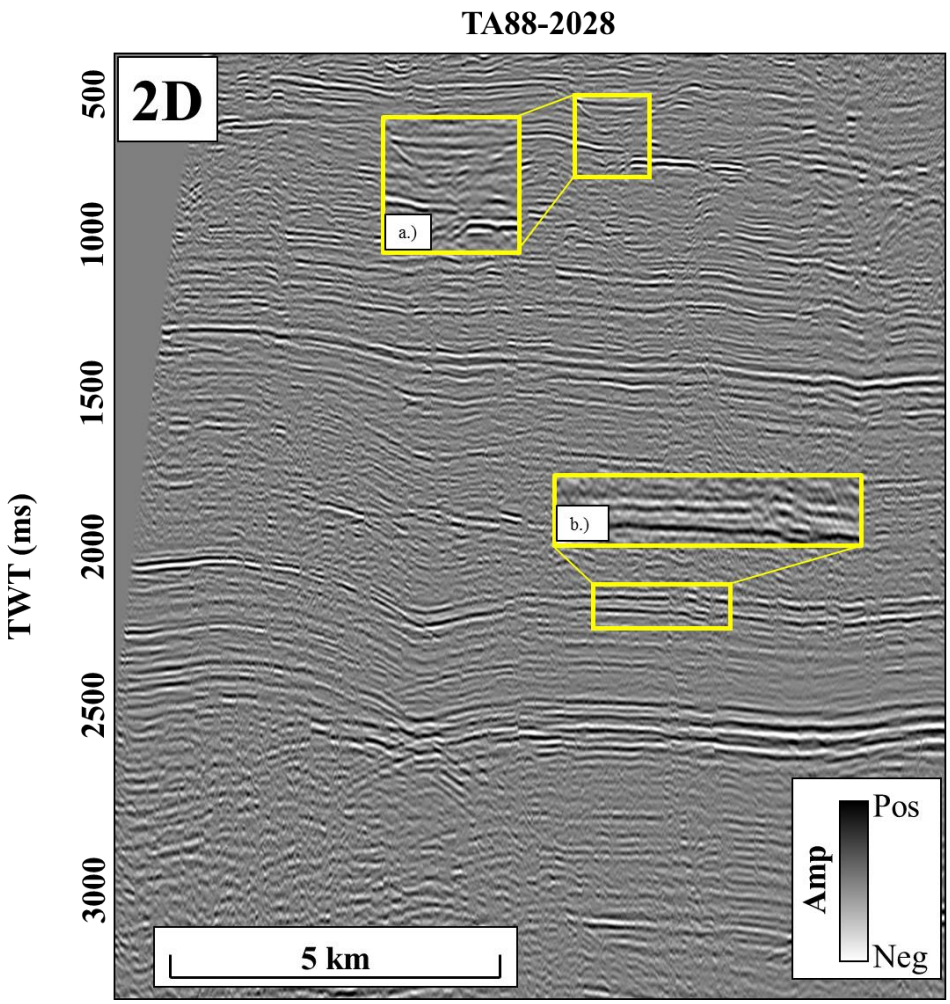

Figure 11. 2D line TA88-2028 shows how resolution varies in 2D seismic data, in (a) reflectors appear as tighter packages with a high contrast between peak and trough. In (b) there is lower contrast between peaks and troughs and reflectors are less continuous. The resolution in the 2D seismic line diminishes with depth, as would be expected since the Earth acts as a filter. However, when compared to the next image from 3D seismic data, the resolution of 2D shallow is greater than that of 3D seismic data shallow. This could be due to more data being stacked in a higher fold at shallower depths in 2D seismic data.

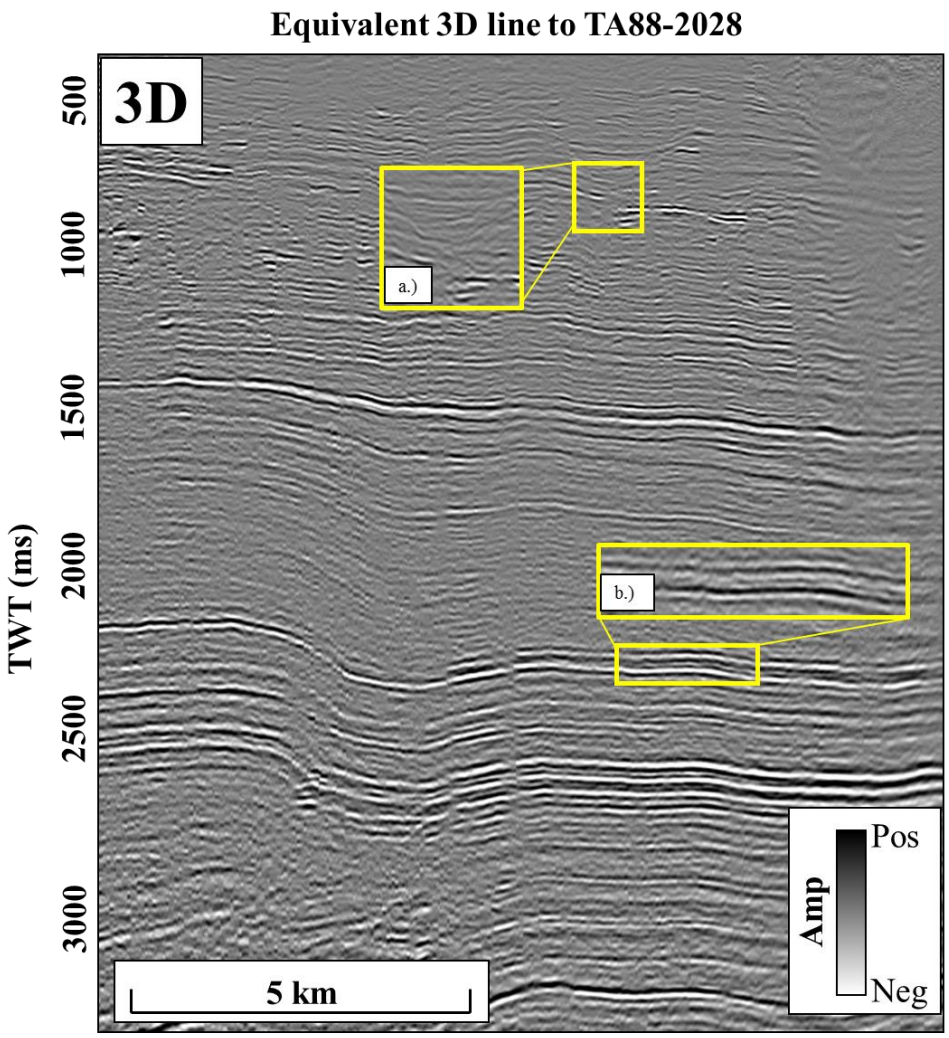

Figure 12. Zoomed in image (a) shows lower amplitude reflectors in 3D than in 2D. Additionally, terminations are not imaged as clearly. In (b) reflectors are higher amplitude and more continuous than in the 2D seismic data.

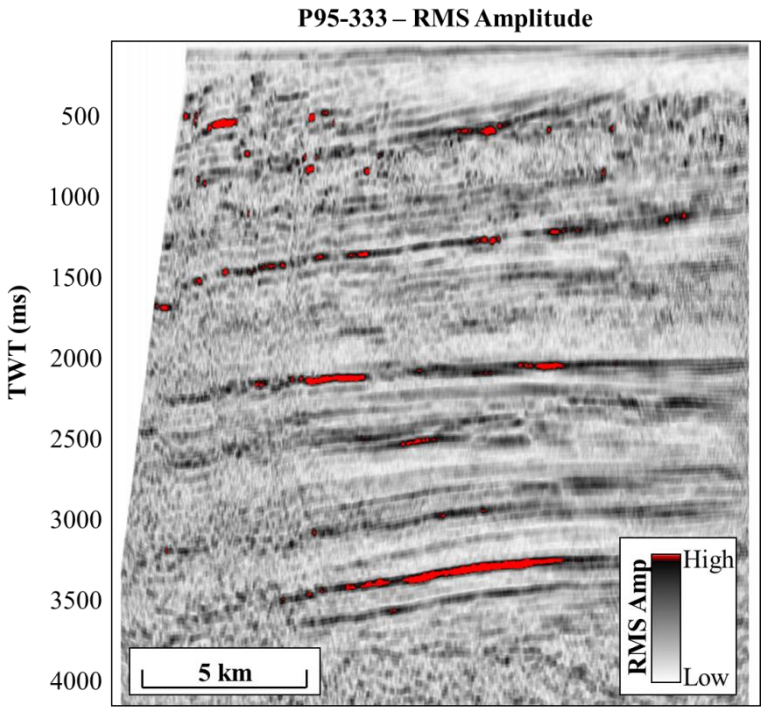

Figure 13. RMS amplitude of the 2D seismic line P95-333. Strong reflectors are imaged equally well in 2D and 3D. The range of amplitude for 2D data is much higher than that of 3D.

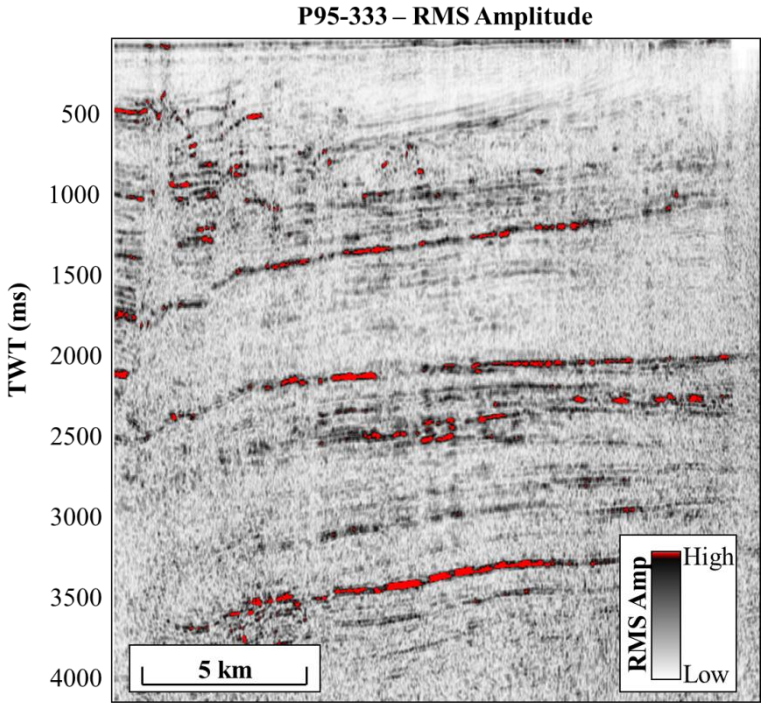

Figure 14. RMS amplitude of the equivalent 3D seismic line to P95-333. Overall, this line shows a much lower amplitude than the 3D seismic data.

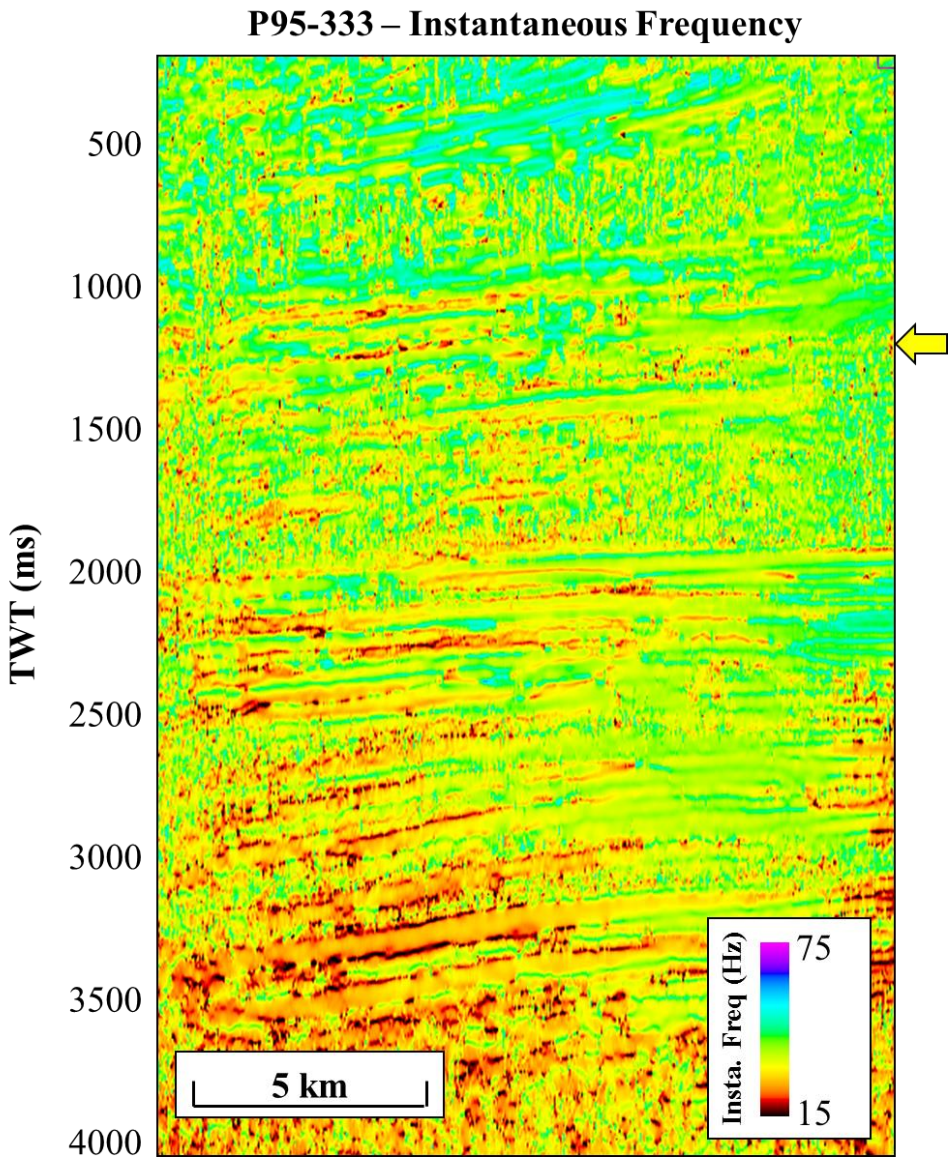

Figure 15. Instantaneous frequency calculated along 2D line P95-333.

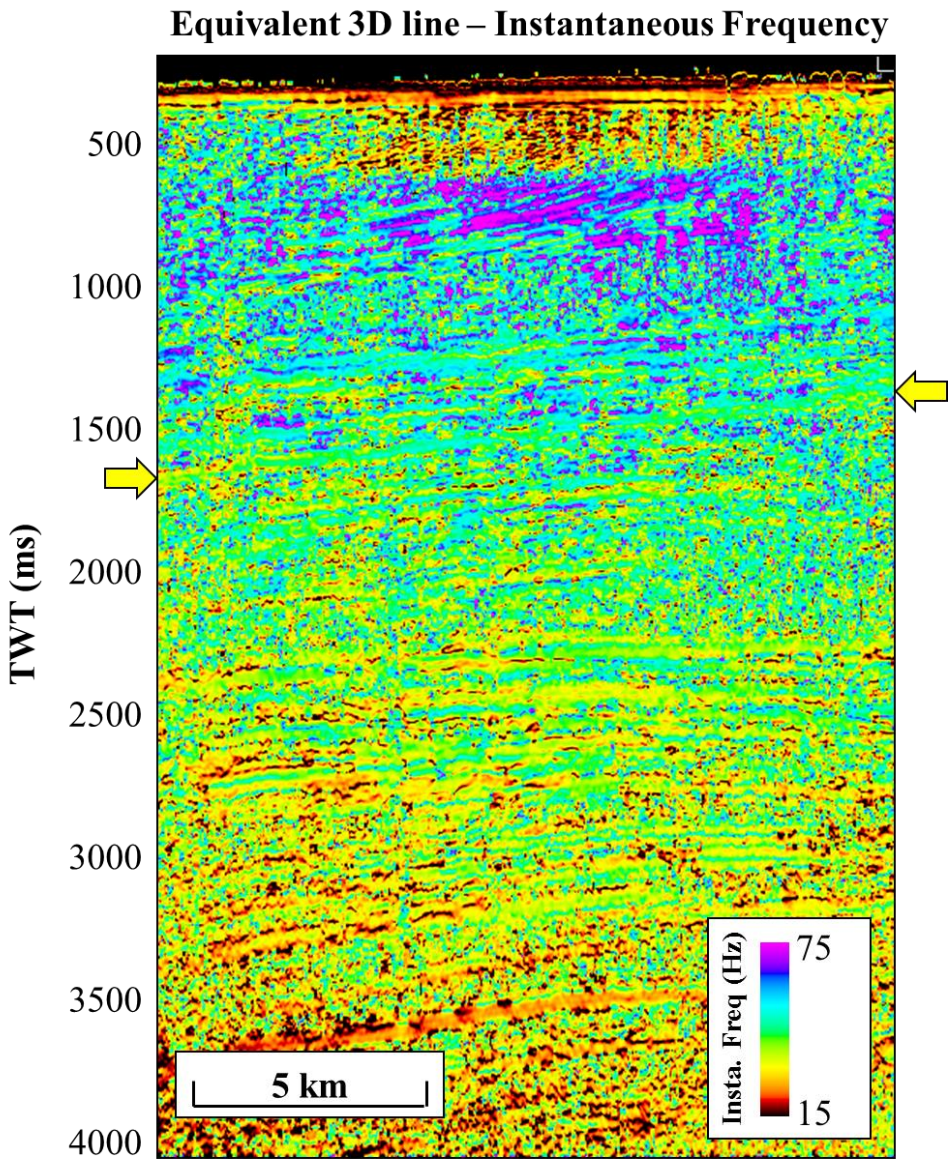

Figure 16. Instantaneous frequency calculated on the 3D Pohokura survey displayed on an "arbitrary" line coincident with the 2D P95-333 line. In comparison with the previous figure, this image highlights the noise that obstructs the image of the 3D. Discontinuous noise patches are seen throughout the 3D data.

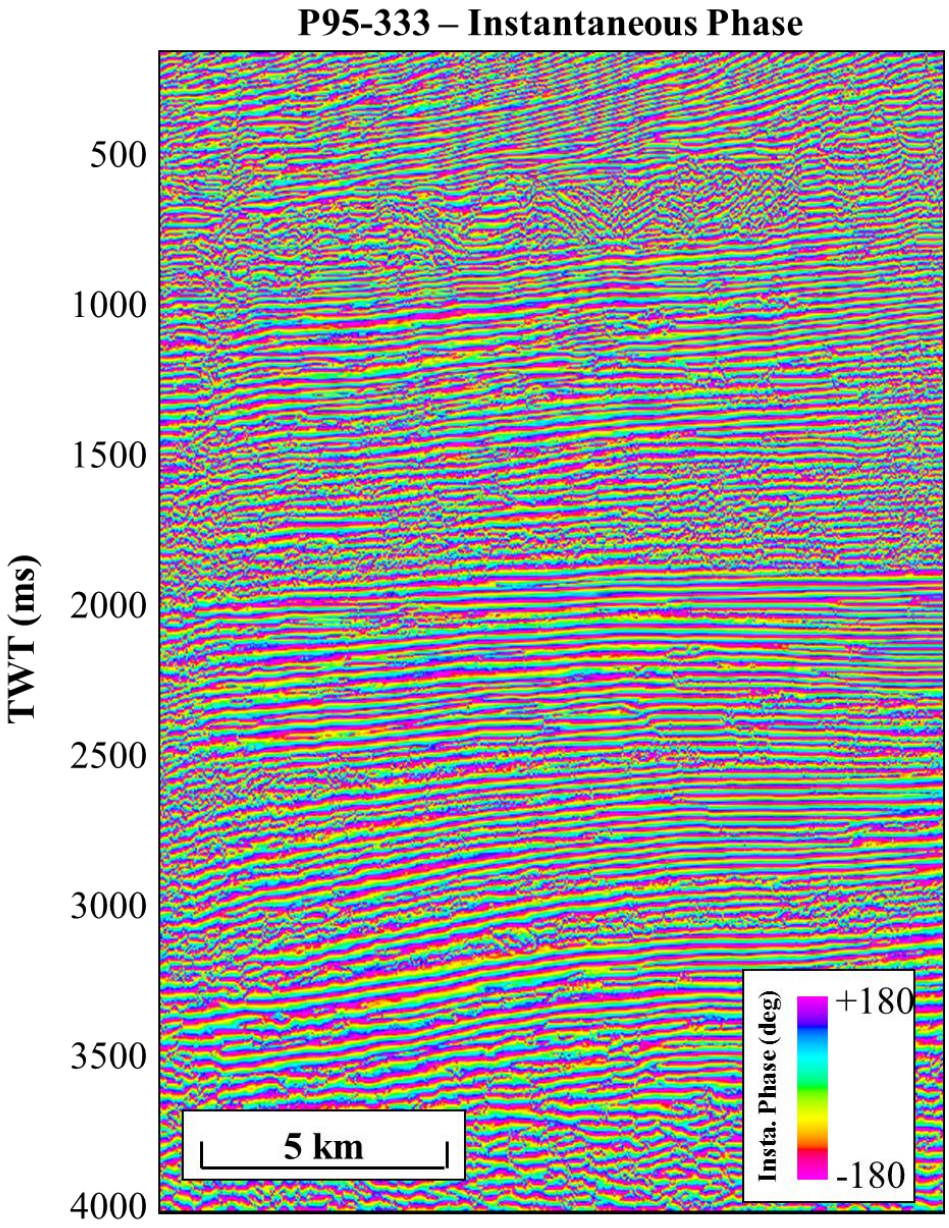

Figure 17. Instantaneous phase calculated on the 2D line P95-333.

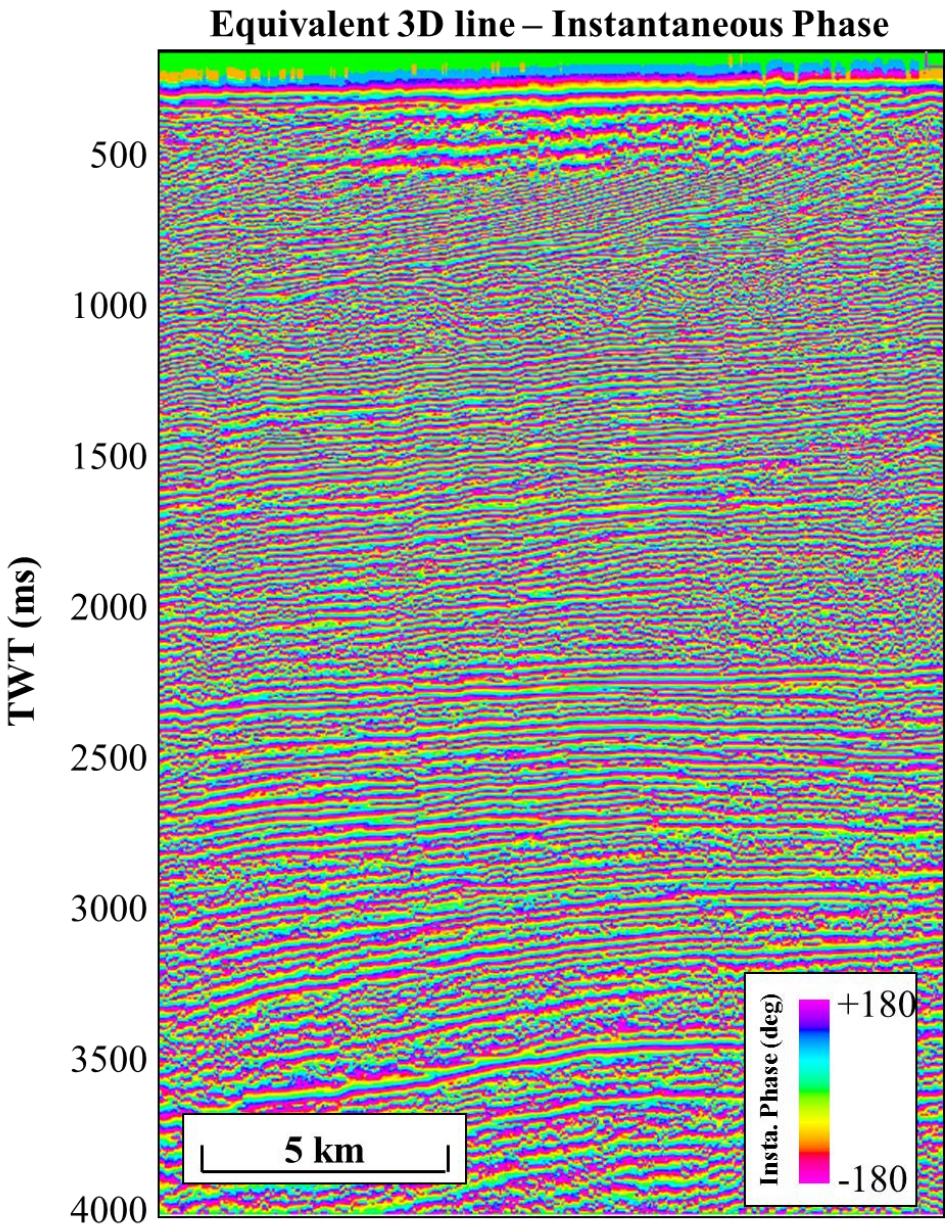

Figure 18. Instantaneous phase on an "arbitrary" line coincident with the 2D line P95-333. Instantaneous phase visualizes a very similar image between both 2D and 3D data, this shows that whether in 2D or 3D, phase information is captured consistently.

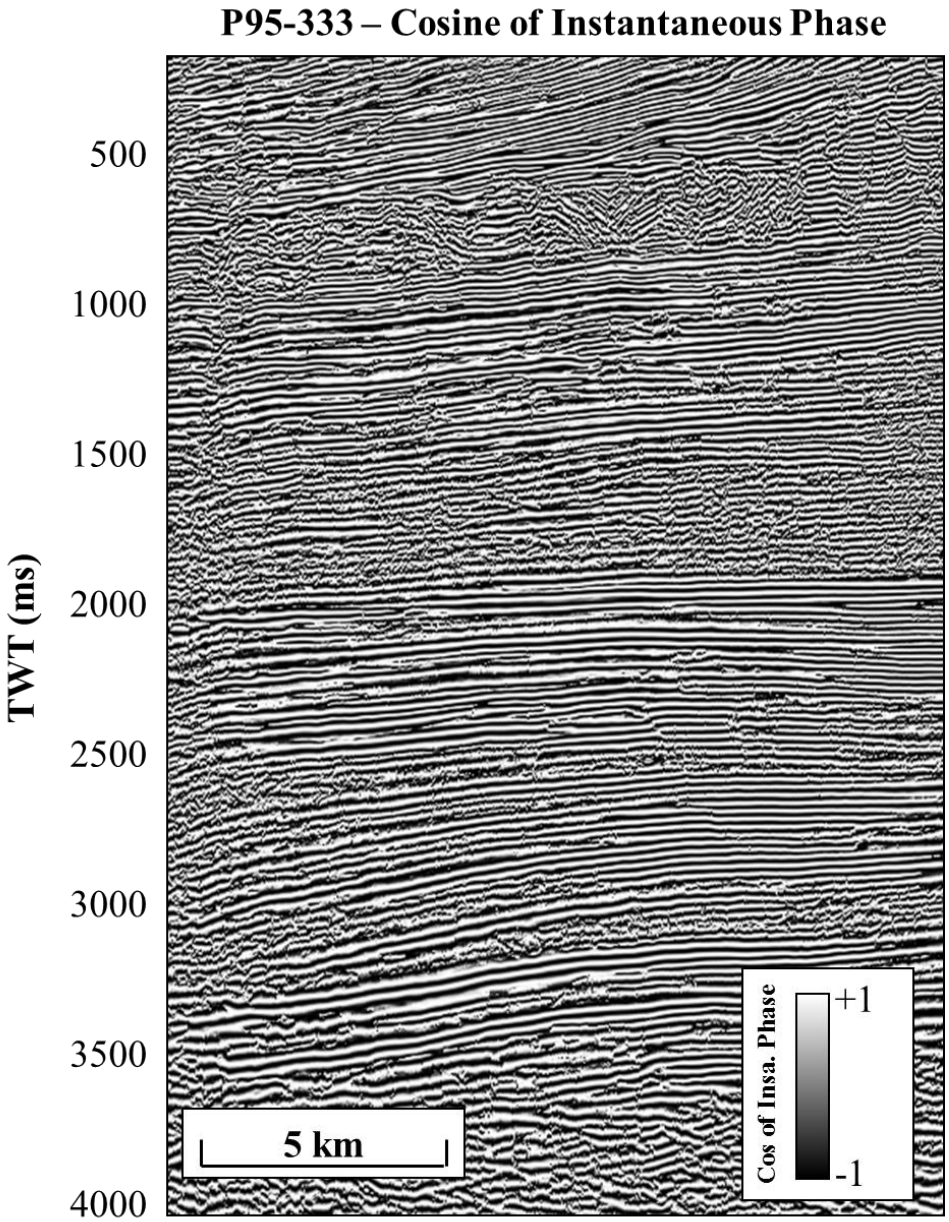

Figure 19. Cosine of the instantaneous phase calculated on the 2D seismic line P95-333. In this line, reflector terminations are visible at 600 ms. A mass transport complex is identifiable from 700 to 1000 ms, and deeper reflector terminations can be seen around 2500 ms.

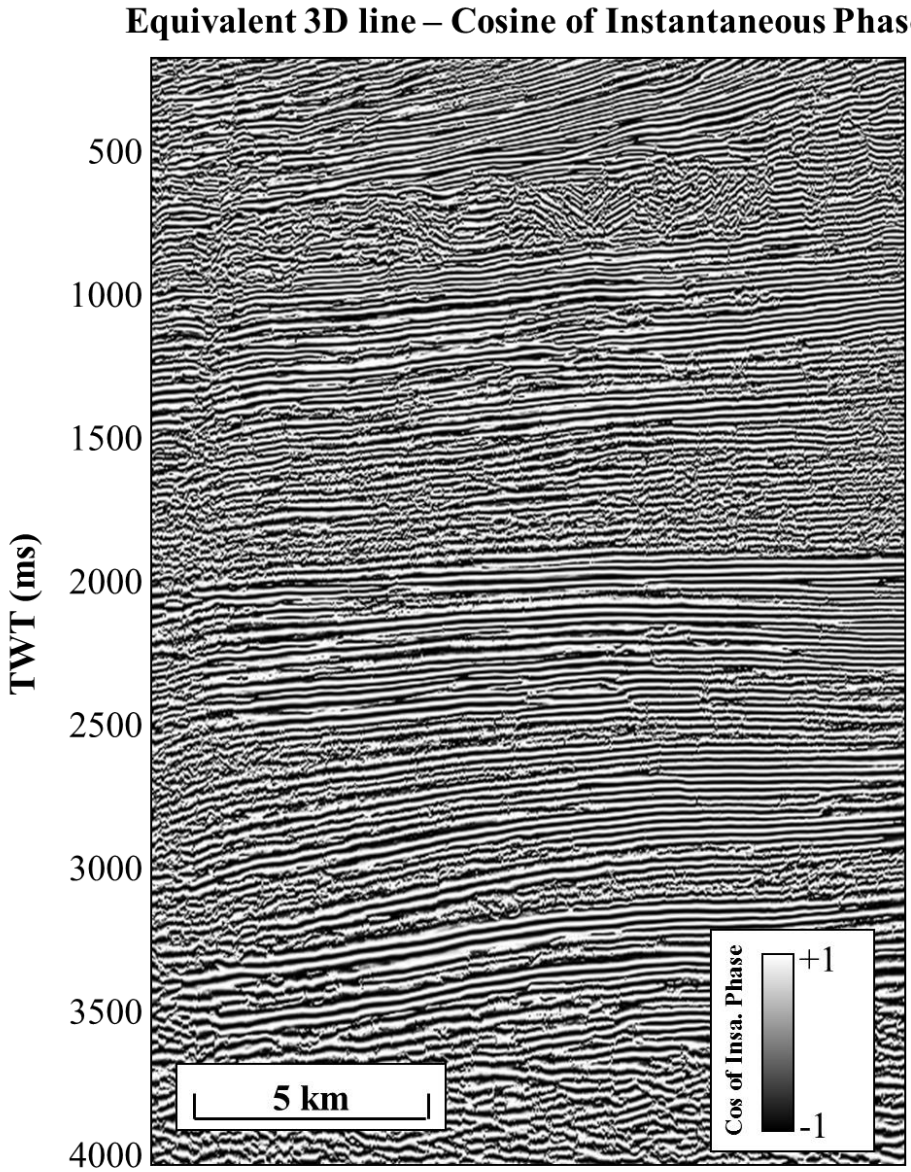

Figure 20. Cosine of instantaneous phase on an "arbitrary" line coincident with 2D line P95-333. On both 2D and 3D data, cosine of instantaneous phase can be used to isolate reflector terminations of stratigraphic significance.

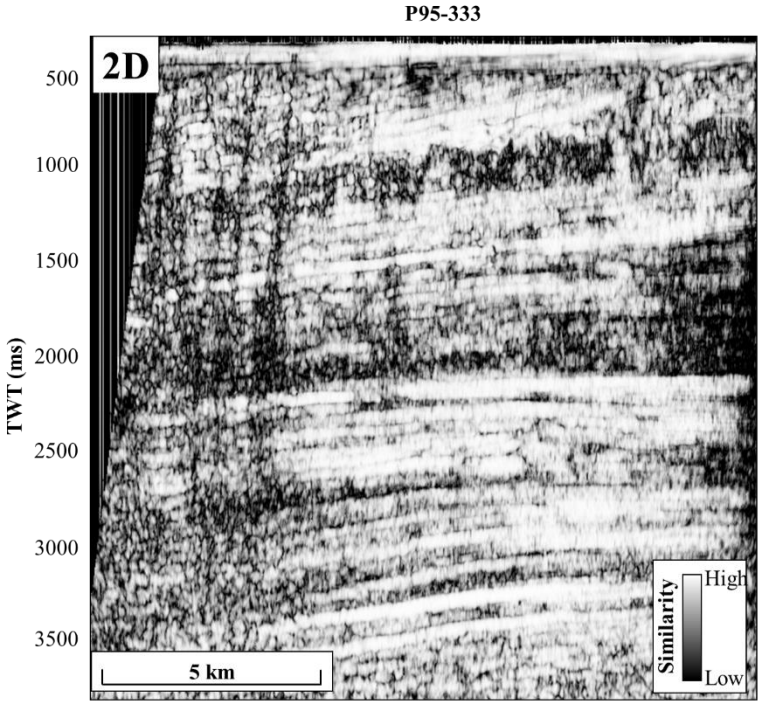

Figure 21. Energy ratio similarity on line P95-333. Fault features on the left side of the vertical cross section are shown well using this attribute.

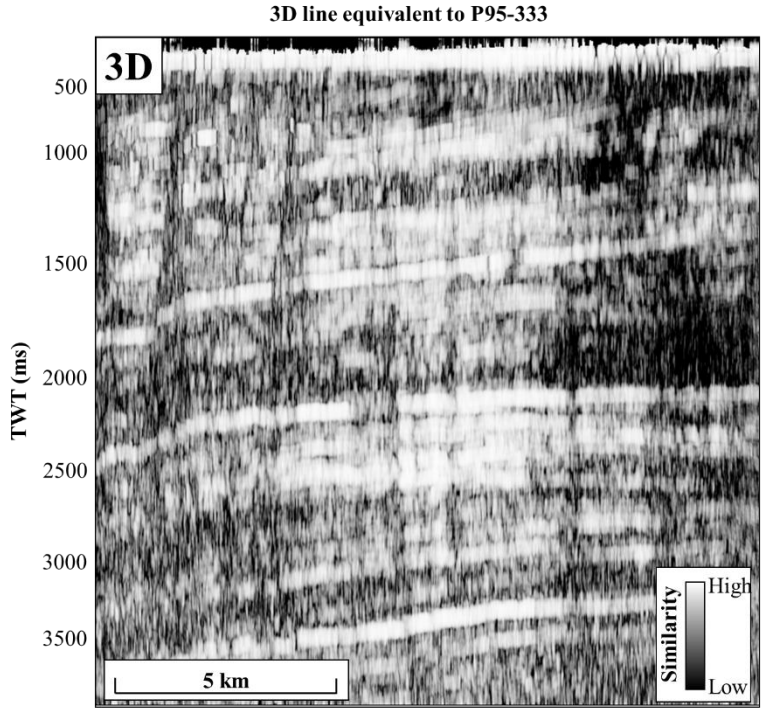

Figure 22. Energy ratio similarity through an arbitrary 3D line equivalent to P95-333. The image is smoothed because of the large window used in dip calculation to overcome noise in the 3D data. However, it is important to note that the same fault features are seen in this image created from 3D data and the previous image from 2D data.

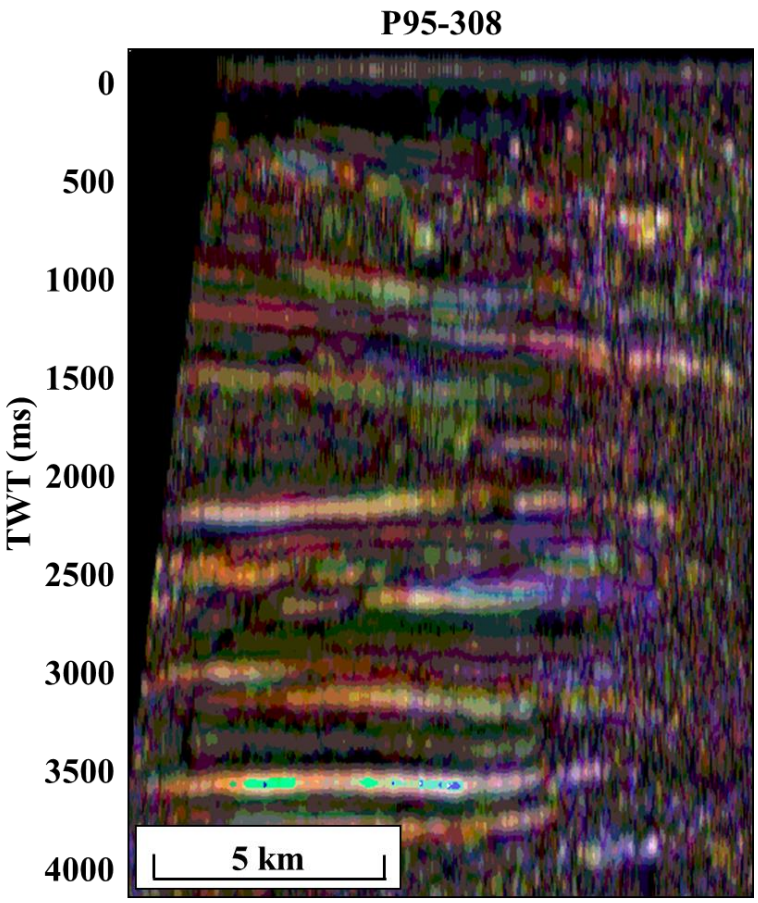

Figure 23. Spectral decomposition on 2D line P95-308. RGB blending of data with red corresponding to 20 Hz, green to 25 Hz, and blue to 30 Hz. White portions of the data are where all three spectral components are represented equally. Magenta is the most common color in section indicating that 20 and 30 Hz dominate this 2D line.

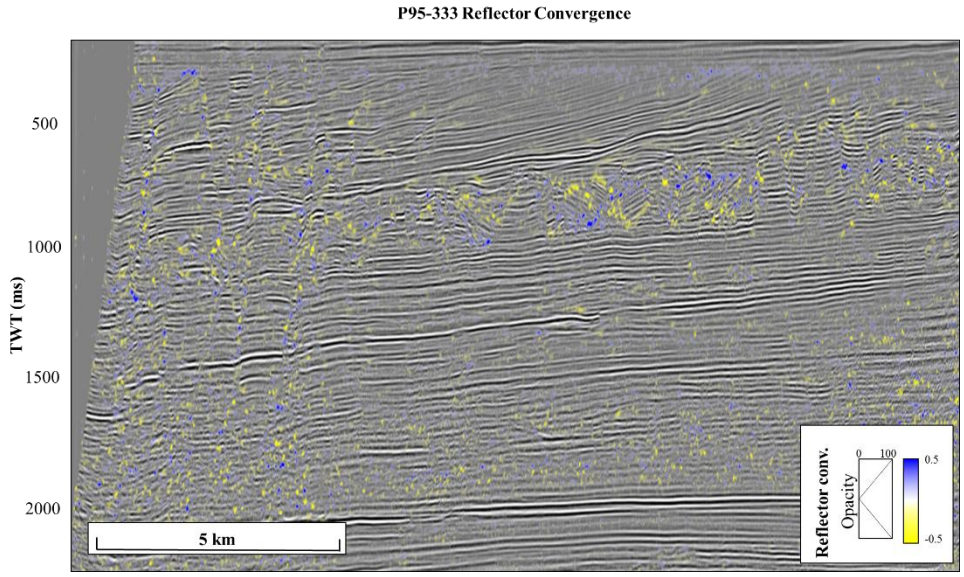

Figure 24. Reflector convergence overlaying 2D seismic data. Reflector convergence is a vector, such that here we only illuminate the apparent reflector convergence in the inline direction. Note that one can highlight reflector terminations such as those seen around 900 ms in the mass transport complex.

Current limitations of mapping surfaces from 2D data

In contrast to software used by Bahorich and Bridges (1992) modern commercial software packages are geared towards 3D seismic data, rendering the process of making surfaces from 2D seismic lines more complicated than it used to be. 2D seismic surfaces are made using the workflow shown in Figure 25. In the commercial software used in this work, a workaround was required to produce a surface from 2D seismic data. A two way time surface must first be created from 2D seismic data. Next, another surface is created from attributes. However, the attribute surface will appear incorrectly as attribute values in the program are assumed to be in time rather than as an attribute value. Thus, those attributes must be copied and pasted onto the TWT surface for proper display.

As Herron (2016) states, 2D migration is unable to account for dip of reflections out of the vertical plane of the migrated section. 2D seismic lines are only able to show apparent dip. Energy will be migrated differently in each seismic line because apparent dip is unique to each seismic line. As a result, in the presence of structure migrated 2D seismic lines will almost always mistie because of differences in the dip direction. Misties of 2D seismic lines along a surface can be seen in Figure 26. Misties in 2D seismic lines appear as “wrap-up”, these features visibly cause irregularities in the contours of Figure 26. Figure 27 shows an image with only the non-intersecting inlines used as input. A surface created from only subparallel dip lines is smoother, avoiding the inherent mistie between intersecting 2D lines. Wrap-up effects are not seen in this image. The strike lines are used to correlate picks on the dip lines.

Another major limitation of mapping surfaces from 2D data is the interpolation of the sparse data. Average spacing between 2D seismic lines in the P95 survey is roughly 1 km. One useful method for interpolating this day would be azimuthal variation through the implementation of a variogram and Kriging. Unfortunately, a consistent application of this technique is not available in the commercial software used in this study.

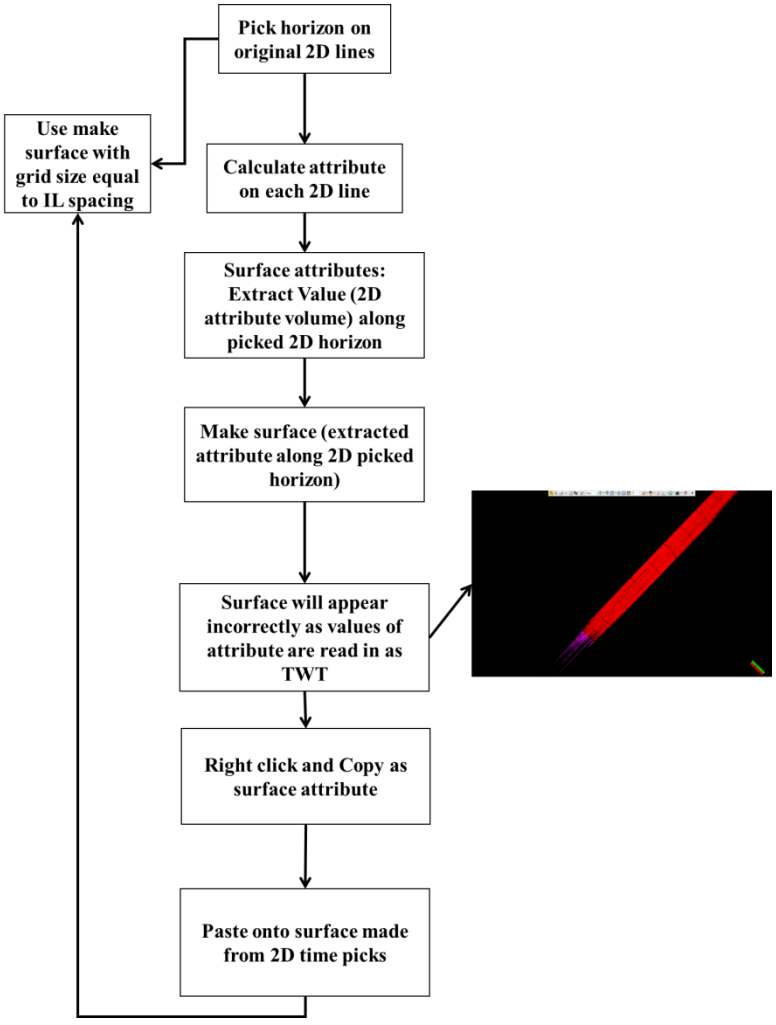

Figure 25. The workflow for creating 2D attributes showing the work around required with creating attributes from surfaces from 2D seismic data. Attribute values must be pasted onto a TWT surface, instead of simply calculating the attributes on the surface as would be the case in 3D seismic data.

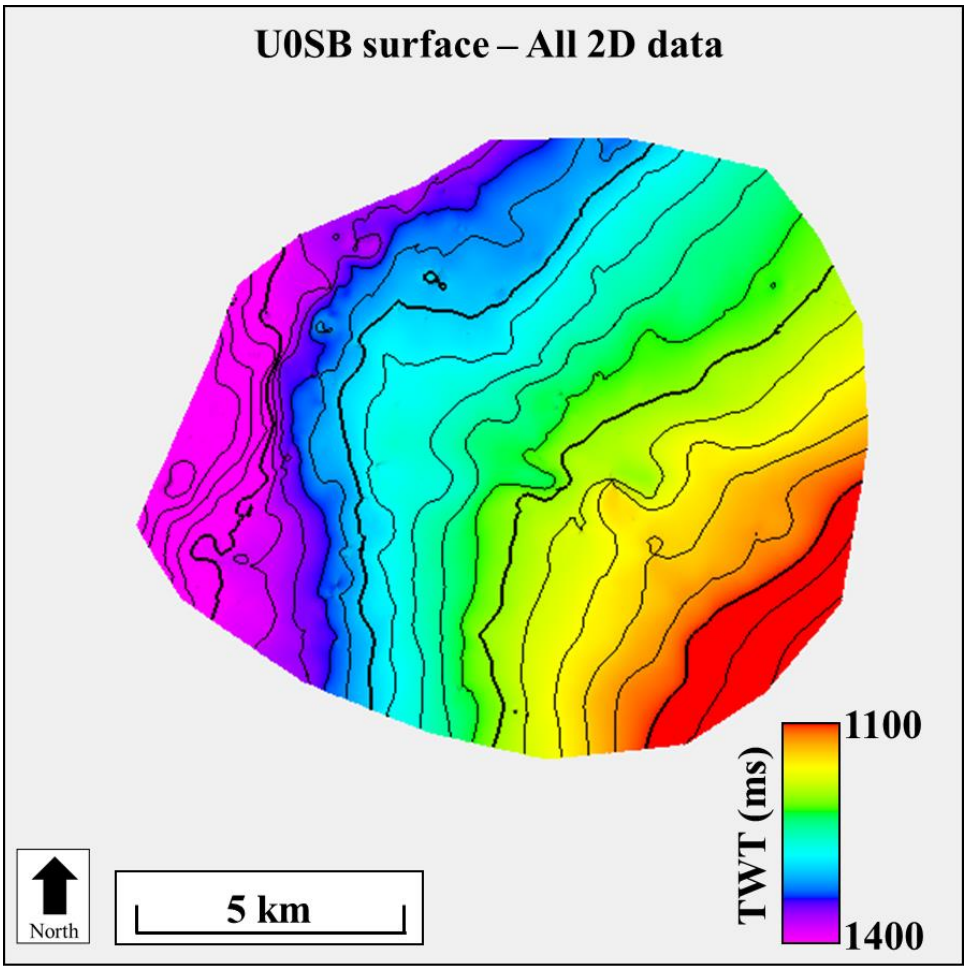

Figure 26. Intersecting 2D dip and strike lines were used to create this surface. Contour lines are erratic due to the misties between 2D lines.

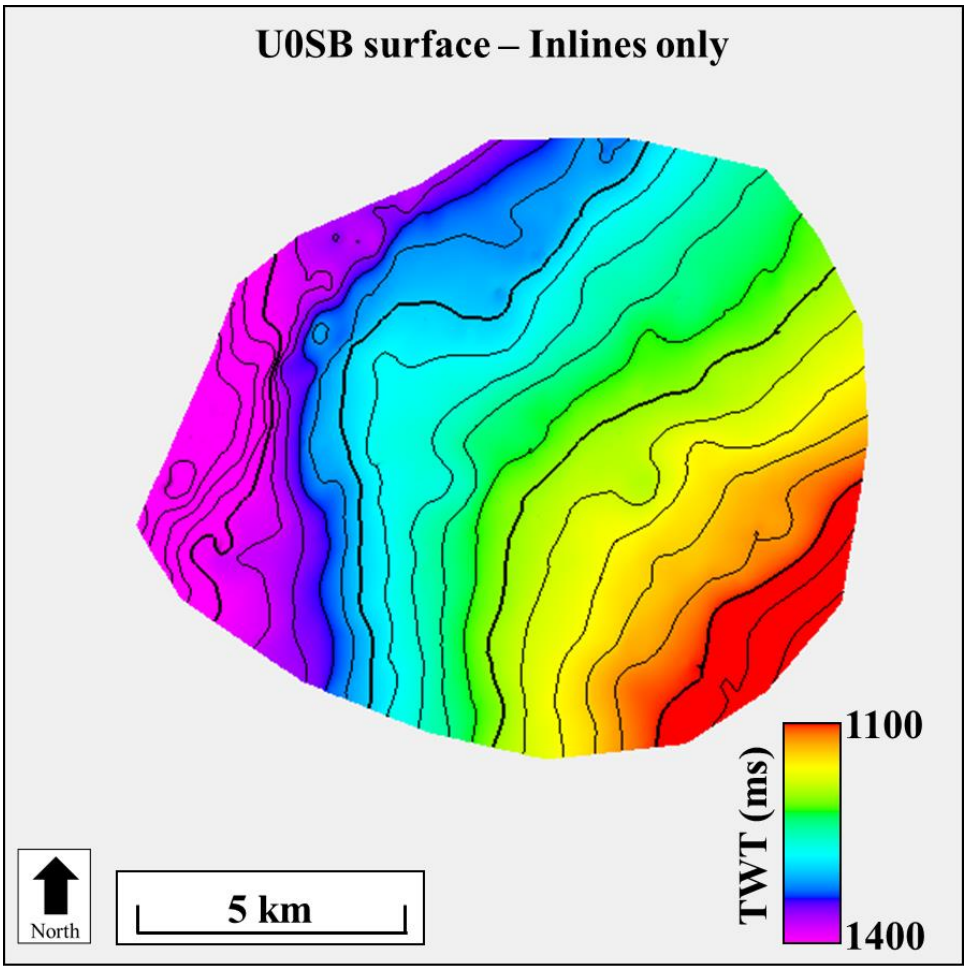

Figure 27. Surface created only using 2D subparallel dip lines show a smoothly dipping structure. Contour lines still display some irregularities, but overall are smoother than using mistied intersecting 2D lines.

Surface comparison

The Pohokura structure is an anticlinal inversion structure that has been targeted by multiple wells as a hydrocarbon trap. Determining a correct size for the feature is important in regards to calculating accurate hydrocarbon estimates, seen in Figure 28 and Figure 29 with the same northwest trending dip of a northeast striking plane. Figure 28, which was created purely from 2D data, makes the dip appear subtler to a rounded-out shape at greater depths and a more expansive size, likely due to fewer 2D dip lines in the upper left portion of the polygons. Hilterman (1981) uses a seismic model to show how 2D seismic surveys can overestimate the size of geologic features as compared to the dense coverage of 3D seismic surveys. Specifically, he analyzed dip and strike line in imaging a geologic feature. Lines oblique to a structural or stratigraphic trap create an image that is too wide, while those 2D lines in the principal direction of dip create a more accurate image.

Original Seismic

Time surfaces created from 2D seismic data are inherently smoother than 3D surfaces. Average spacing between 2D lines is roughly 1 km. The coarse spacing causes subtle features to be distorted and sometimes missing all together. Figure 33 shows a time-structure surface created from 3D data along the U0SB surface. An interpreted mass transport complex (MTC) is indicated by an orange arrow. Its high amplitude seismic response can be seen in the associated seismic line. The eastern edge of the MTC corresponds to a slump block fault indicated by a white dashed line. The model for this interpretation can be seen in Figure 35. Thrust blocks are also visible in the 3D, a further validation of the interpretation. When we turn to the 2D surface, things

become less clear. The start of the MTC is still visible as a high amplitude response in seismic amplitude, and a concave surface. However, the limits of the MTC are not as clear. Because of the coarseness of the data, the slump blocks on the eastern bound of the MTC appear smooth, and the boundary migrates eastward making the MTC appear larger than it is, while the western bound is not visible at all.

Figure 32 shows the effects of using the default gridding size of 50 m by 50 m when creating a surface. Geologic details are smoothed, but so is some noise as shown in the white circle of Figure 31 and Figure 32. This figure was created to show how important detail can be lost by falling into the pitfall of using too large of a grid size. A grid size of either the inline and crossline increment or bin size measurements should be used when gridding, whichever is smaller. In 2D seismic data, through testing it appears that the CDP spacing is optimal for gridding of surfaces.

Single-trace attributes

Instantaneous frequency on 3D surface does a very good job of delineating a MTC. High frequencies extracted from the complex trace outline the bounds of the MTC very closely. This also shows that some of the bounding slump blocks on the MTC may be associated with higher frequencies. The cosine of phase, while useful in vertical section, is not of much value along a surface. Low values and short discontinuities are near impossible for this commercial software to interpolate.

Multi-trace attributes

Several types of curvature were extracted along 2D and 3D surfaces below. Figure 40 shows k_1 curvature extracted along the 3D horizon. The detail of this horizon

cannot be matched by 2D. However, some long wavelength structures can be interpreted in both 2D and 3D horizons. Figure 41 shows a curvature attribute computed from a surface created from 2D data. The surface is heavily biased towards the lines it was picked on. However, the surface also shows some curvature patterns consistent with the 3D surface. Yellow and green arrows highlight positive and negative curvature anomalies that are associated with the faulting that occurs on this horizon. These faults can be seen because they are large regional features. They are recorded in multiple lines and as such can be interpolated from line to line, unlike smaller stratigraphic features or less continuous faults.

One common multi-trace attribute used here for comparison is similarity. Similarity (Figure 42 and Figure 43) is interesting here because it shows it can be valuable for large en echelon fault features, but it cannot image the MTC in the lower portion of the image. The MTC is bounded by discontinuity features just as the en echelon faulting, but a single linear discontinuity feature cannot be seen in 2D the way that several discontinuity features lined up can be imaged.

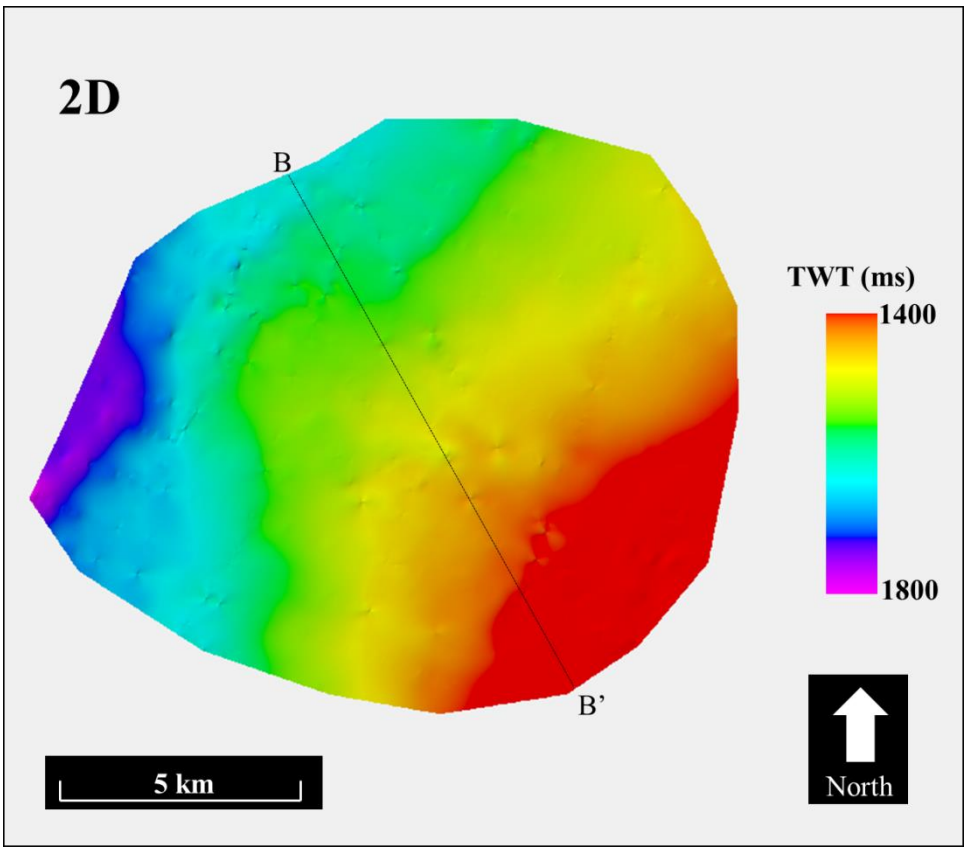

Figure 28. A time structure surface of the U0SB horizon showing the same regional trends that are seen in the time structure surface made from 3D data.

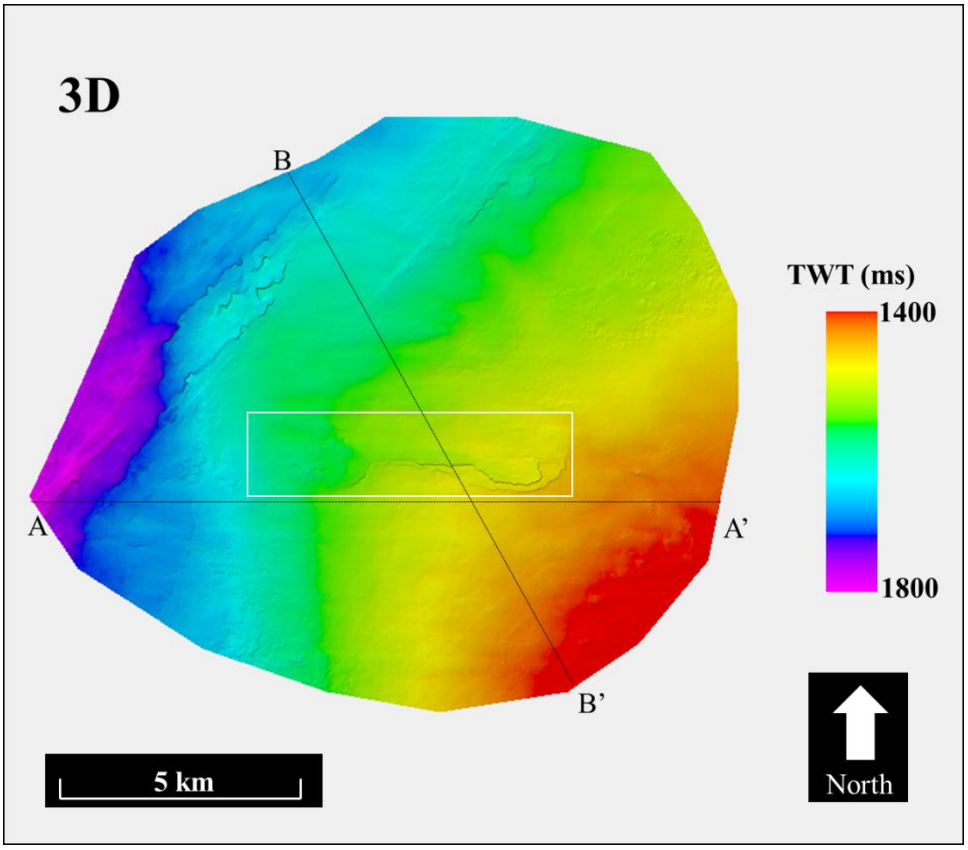

Figure 29. A time surface on the U0SB horizon created from only 3D seismic data of the Pohokura survey. A geologic feature that is not visible in **Figure 28** is highlighted with a white rectangle.

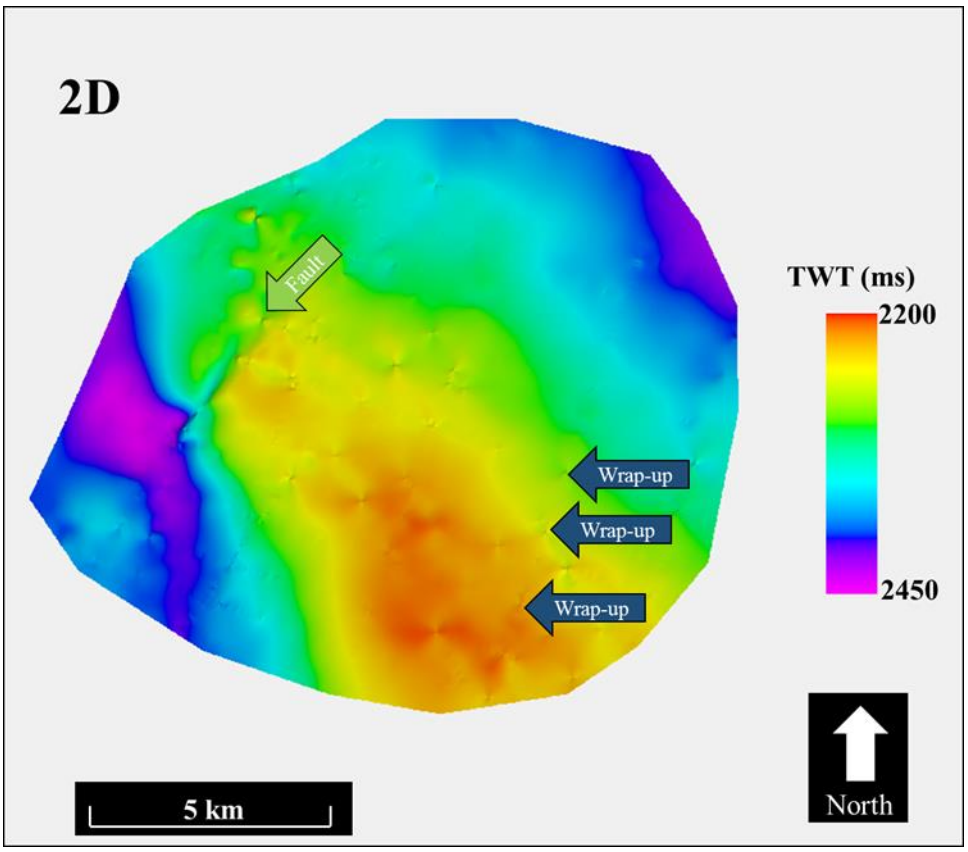

Figure 30. Time structure surface of the Tikorangi surface created from 2D seismic data. The green arrow indicates the cut of a fault through the horizon. Lineations of the 2D seismic lines can also be seen as "wrap-up" points caused by interpolation of sparse data.

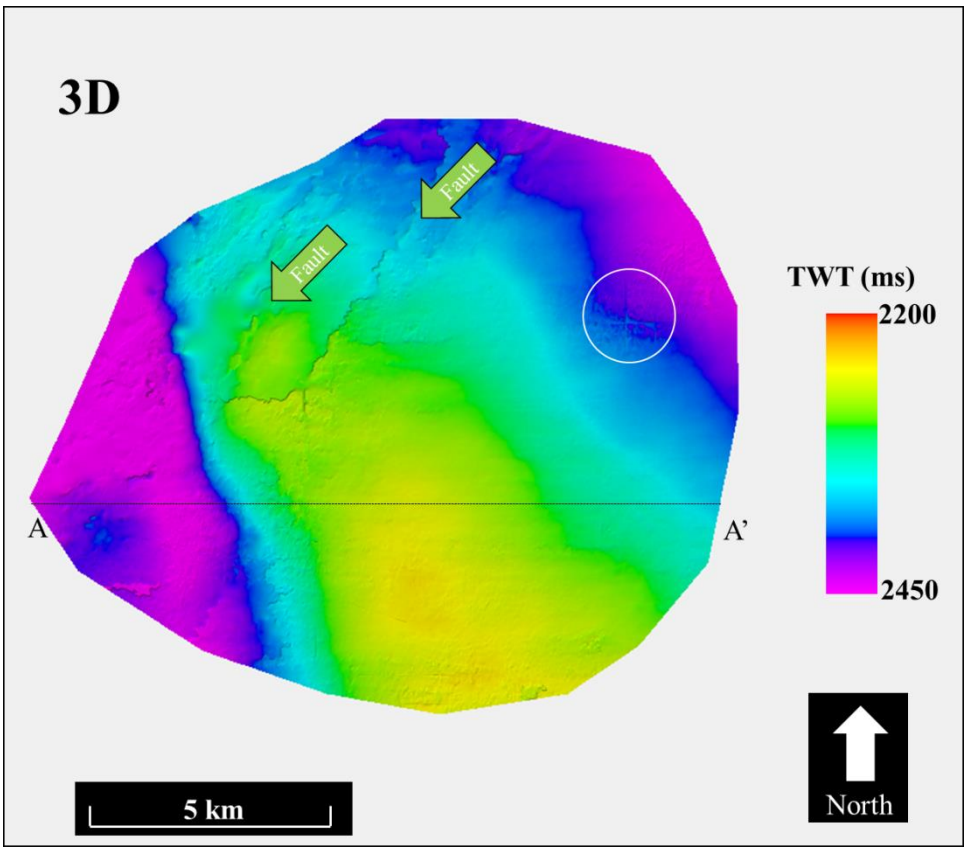

Figure 31. The time structure surface of the Tikorangi formation from 3D data shows two faults that do not appear in the 2D data. Also, an artifact from the seismic processing, which does not appear in the 2D data surface, is shown in the white circle.

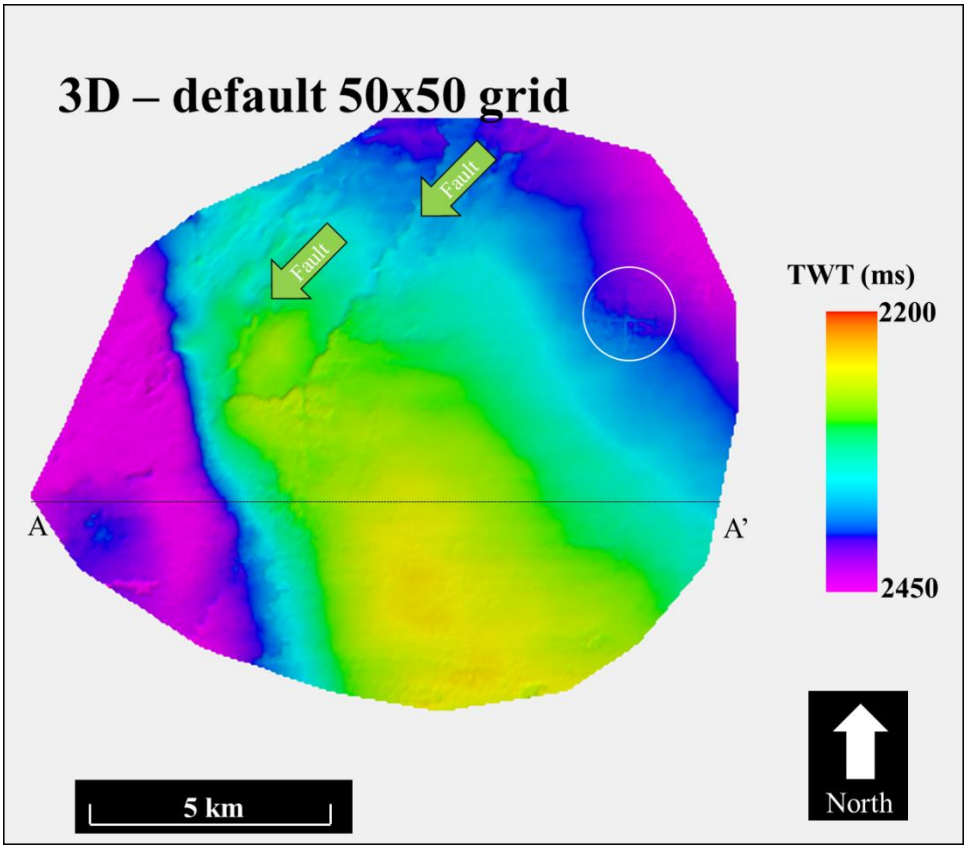

Figure 32. Results of interpolating the time structure surface from the 3D data on the default, sparse 50 by 50 grid. Detail of the faults is lost, but effect of the noise is also slightly diminished in the white circle.

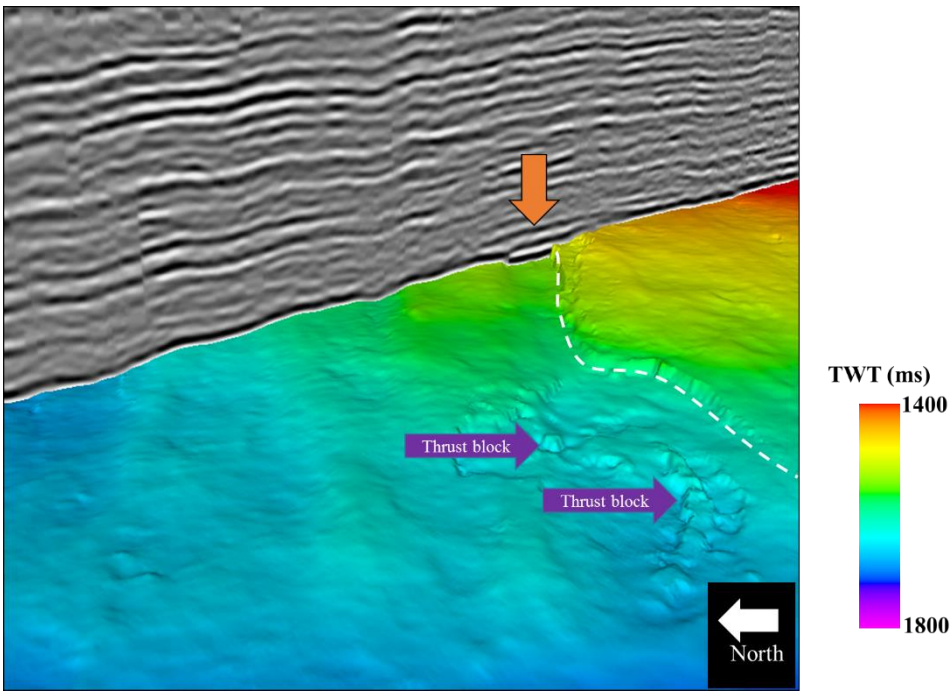

Figure 33. U0SB horizon accompanied by an arbitrary line equivalent to 2D line P95-333. The orange arrow indicates the upper region of a mass transport complex bounded to the East by slump block faulting emphasized by the white dashed line. Thrust blocks are also visible at the end of the mass transport complex.

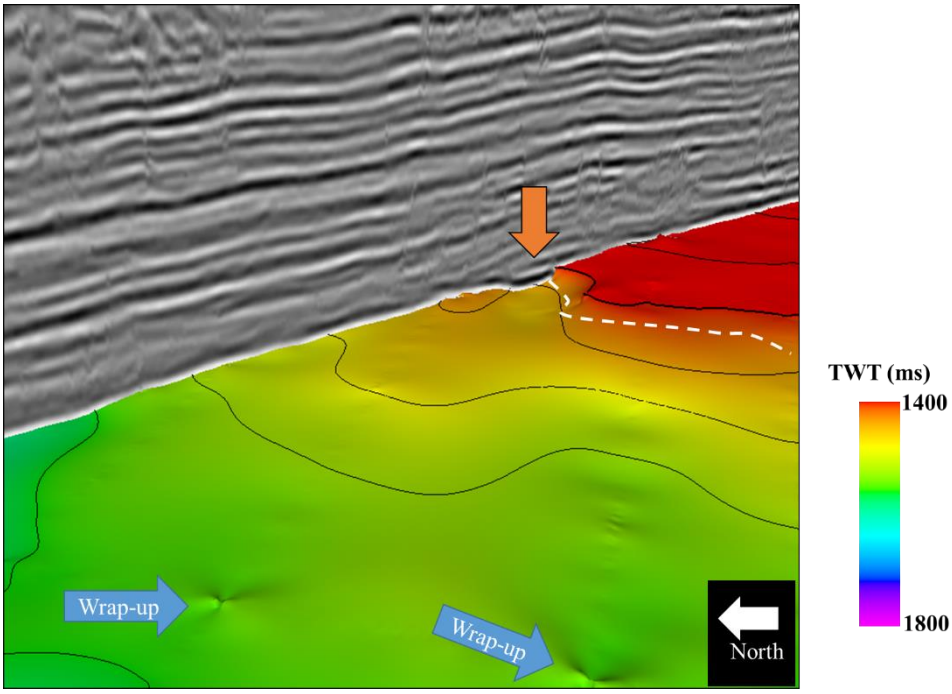

Figure 34. U0SB surface picked on 2D seismic. The beginning of the mass transport complex (MTC) is identified with the orange arrow and imaged well at that point on the surface. The white dashed line indicating the bounds of the MTC is much less accurate than on the 3D data surface. Blue arrows indicate wrap-up, a common artifact from 2D interpolation.

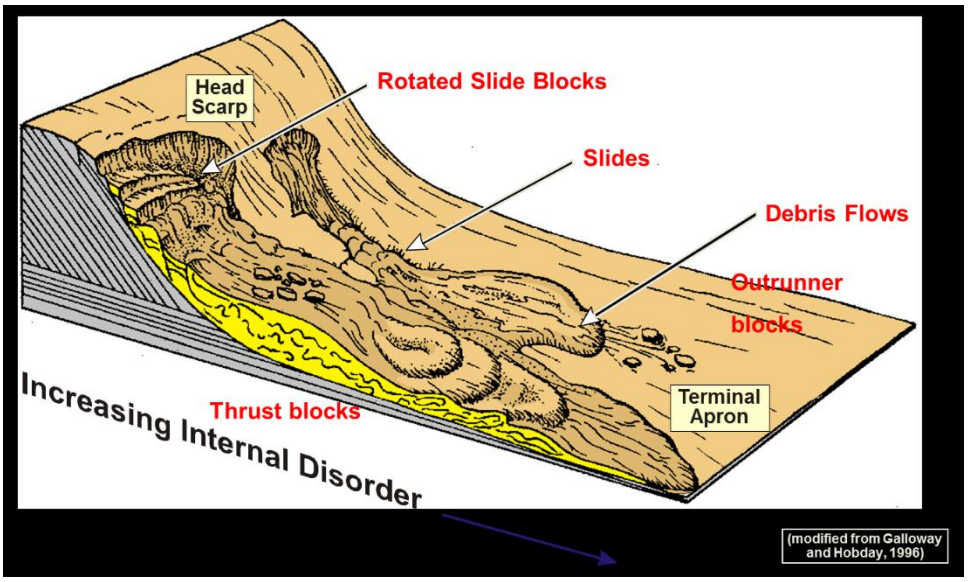

Figure 35. Model for interpretation of feature on U0SB surface. Slump block faulting, thrust blocks, and head scarp are all identifiable in 3D surface. Modified from Galloway and Hobday (1996).

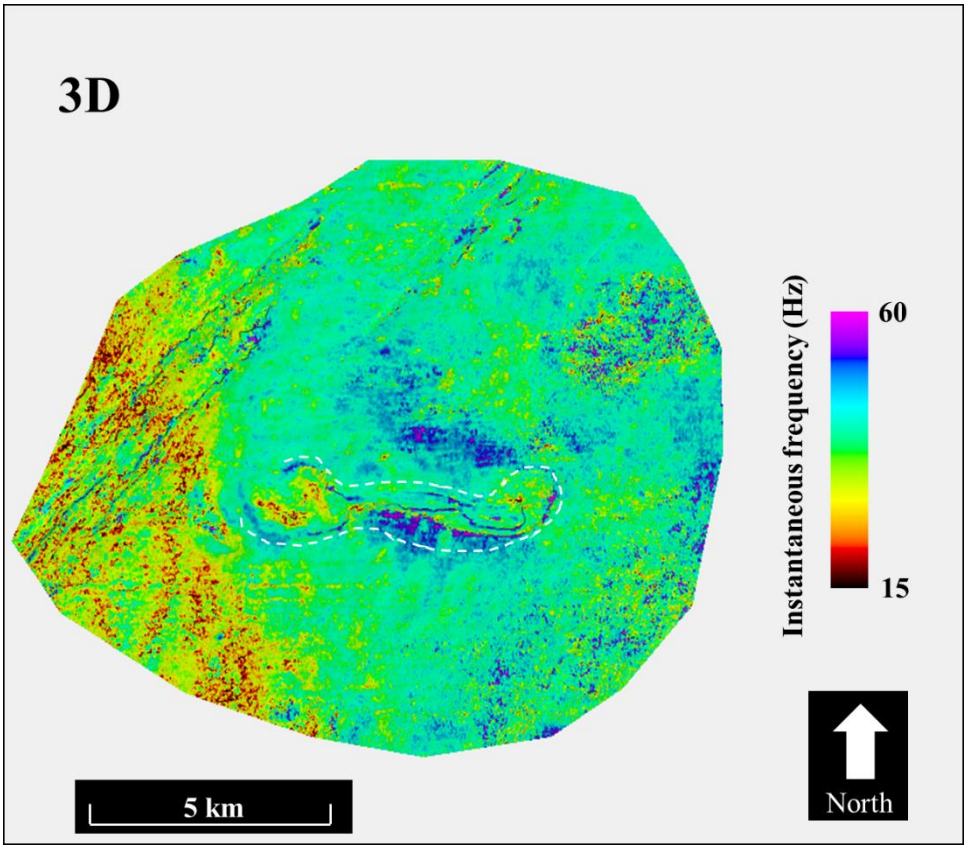

Figure 36. Instantaneous frequency of the U0SB surface extracted on a 3D horizon shows a very detailed outline of an MTC structure. High frequencies bound the edge of the structure and a white dashed line is used to outline the general shape of the feature.

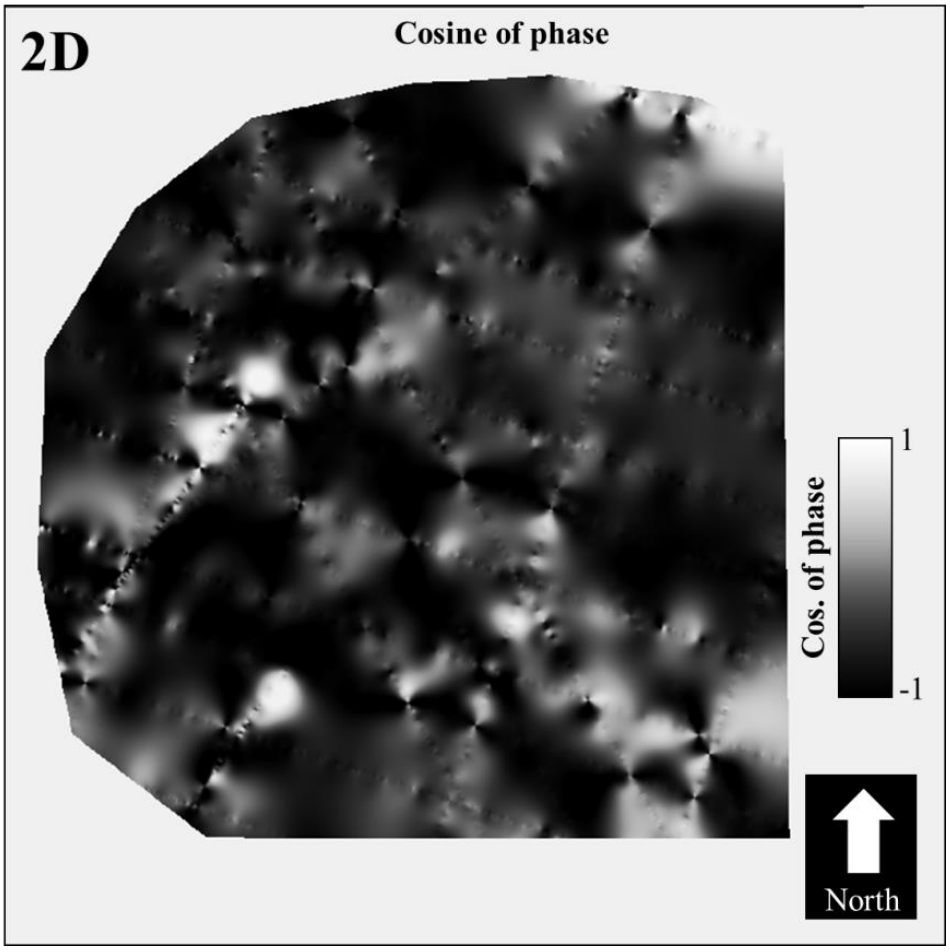

Figure 37. Cosine of instantaneous phase on 2D seismic shows relatively little information.

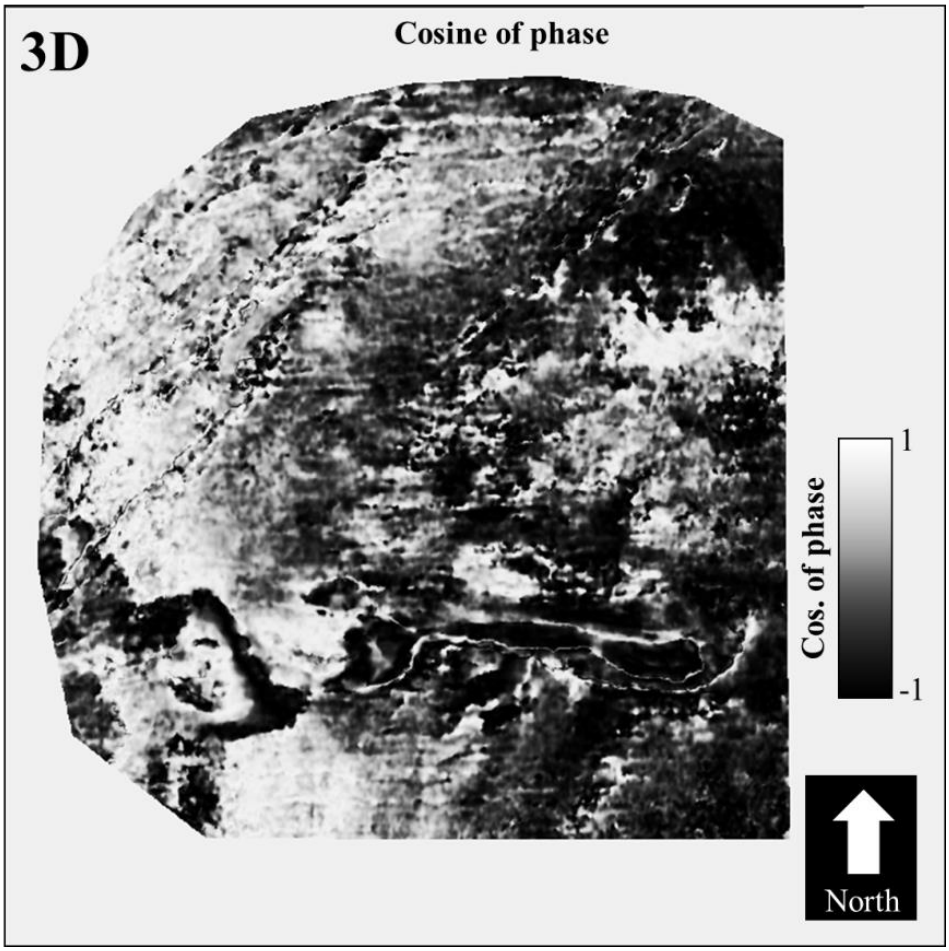

Figure 38. Cosine of instantaneous phase on a surface from 3D seismic data does an excellent job of emphasizing terminations.

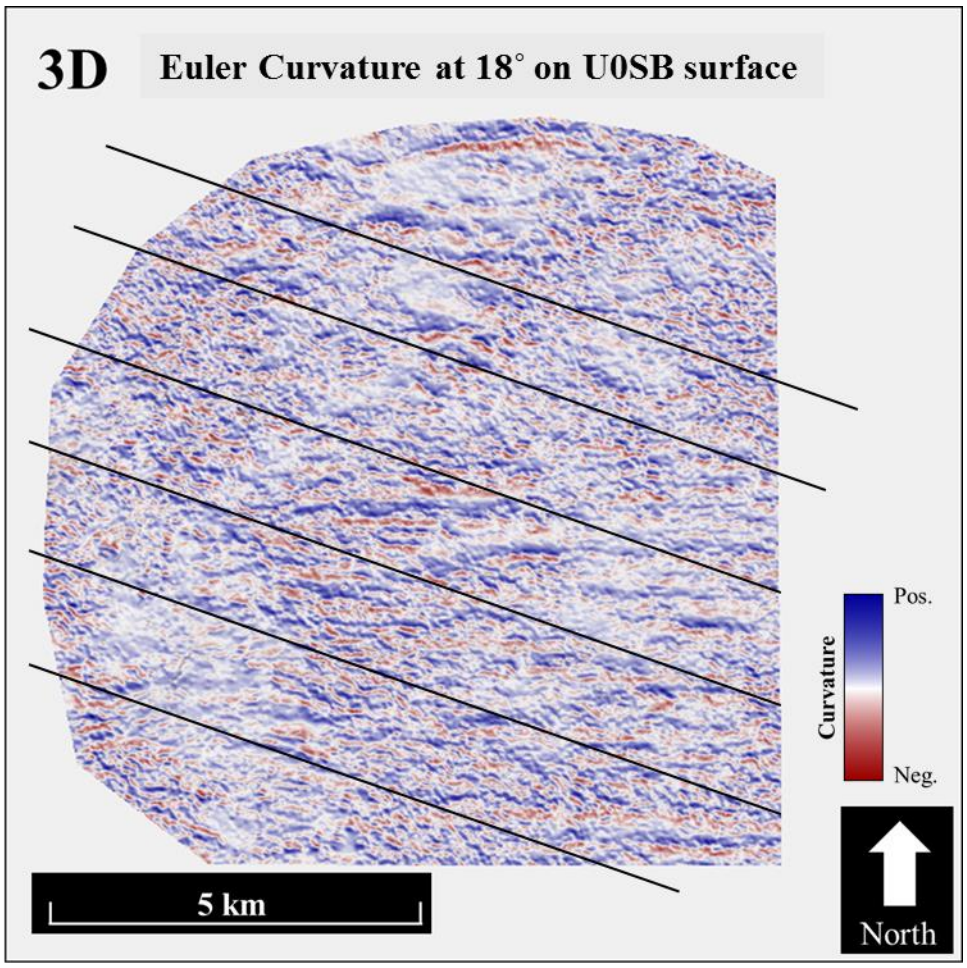

Figure 39. Euler curvature with a strike of 18˚ along the U0SB surface. Black lines show the orientation of subparallel 2D dip lines. This curvature emulates an idealized 2D curvature.

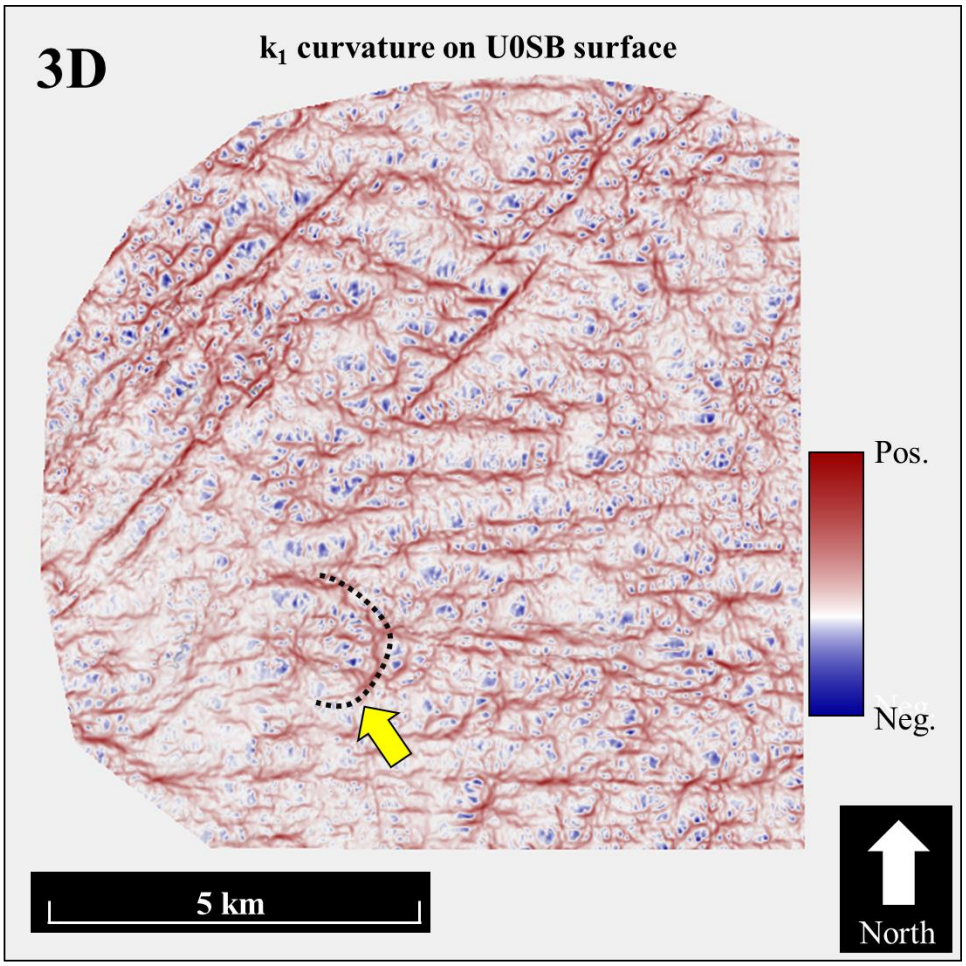

Figure 40. k_1 most positive curvature along the U0SB horizon. A yellow arrow points to a black dotted line which outlines the terminal apron of the MTC.

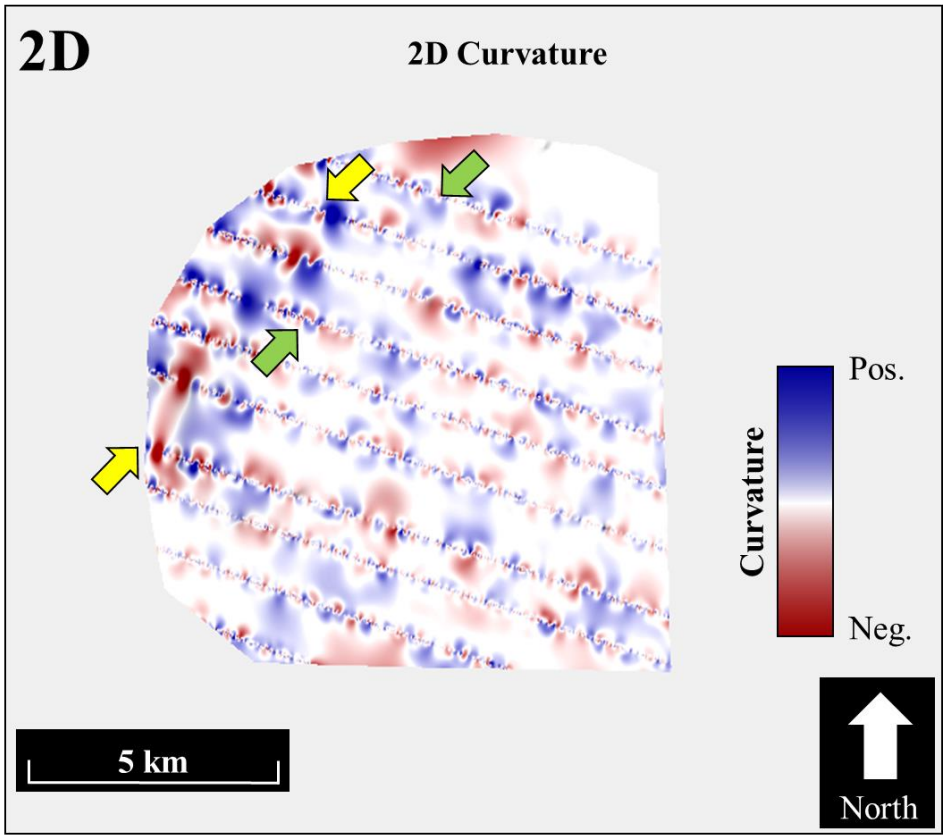

Figure 41. 2D curvature from the P95 lines. Yellow arrows indicate a positive curvature fault feature that aligns with the same feature in a 3D surface. The green arrows indicate an area where a linear curvature anomaly that appears in surfaces from 3D is not captured in the 2D surface.

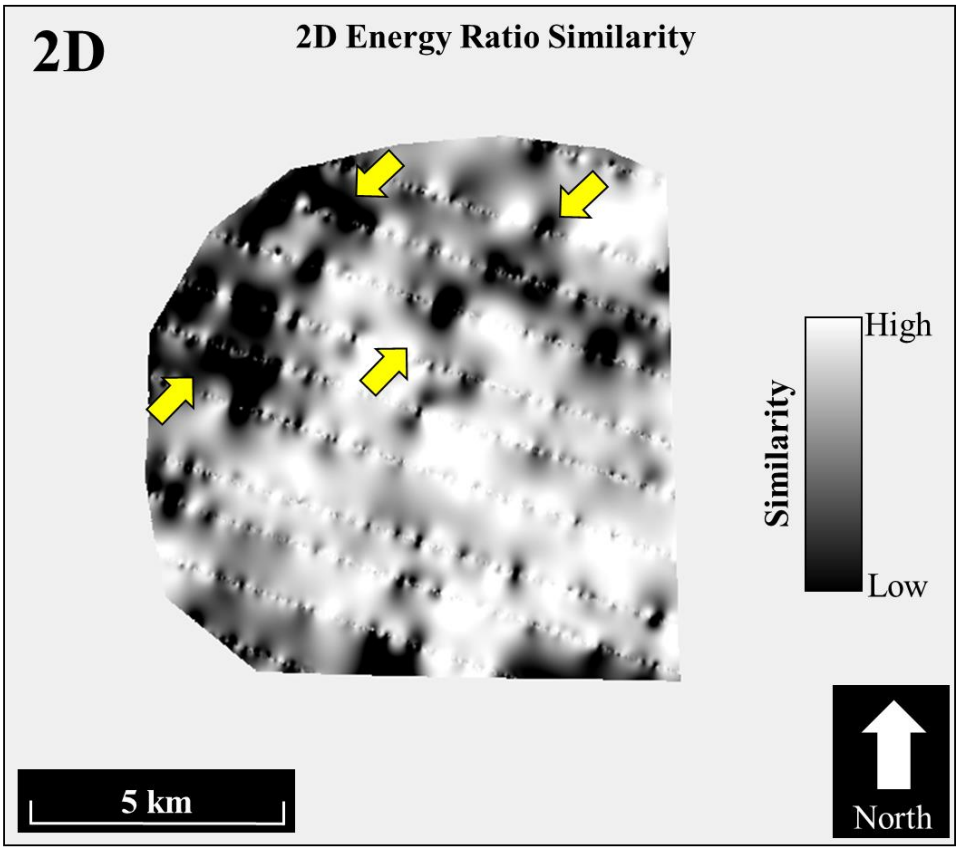

Figure 42. Energy ratio similarity along the U0SB surface. Yellow arrows indicate a fault lineament that is captured in 2D. Unfortunately the 2D surface misses the parallel fault feature to the East.

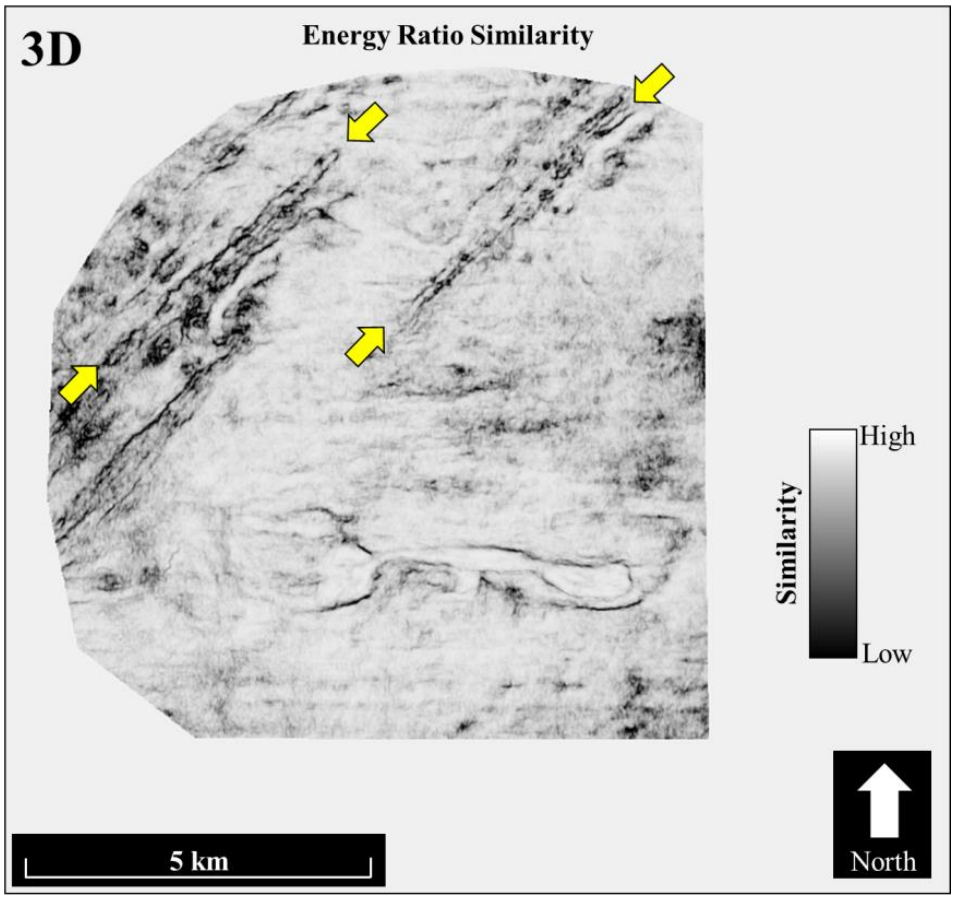

Figure 43. Yellow arrows highlight fault lineations that are highlighted in both 2D and 3D. Unfortunately, the mass transport complex outlined by slump faults in the southern portion of the 3D surface is not imaged in the 2D surface.

Data Conditioning

Crosscutting noise of high and low frequency contaminate much of the seismic survey (Figure 50). With no access to the prestack seismic volume, the true source of the noise cannot be investigated further. The crosscutting nature of the noise suggests it is related to migration aliasing artifacts introduced in the Kirchhoff prestack time migration implemented in the processing workflow (Biondi, 2007). Since attributes enhance subtle features, this crosscutting, not-so-subtle noise needs to be suppressed.

Spectral Balancing

Crosscutting noise from migration and poor reflector continuity in the 3D Pohokura 3D survey create the need for data conditioning. The steeply dipping crosscutting nature of the noise suggests migration aliasing artifacts are due to insufficient surface sampling of the data. Furthermore, towards the lateral edges of the migration operator the wavelet is rotated, resulting in very low vertical wavenumber that in time migration appears as very low temporal frequencies, outside the acquired spectrum to the data.

Chopra and Marfurt (2016) describe a methodology for amplitude-friendly spectral balancing. In their technique, one first decomposes the data into time-frequency spectral components. In a given time window, and over all the traces of the spatial volume, the power of the spectral magnitude is computed. The power of the spectral magnitude is then averaged and results in a smoothed average power spectrum. Next the peak of this average power spectrum is computed, and the average spectral magnitude and the peak of the average power spectrum are used to design a "single time-varying spectral-balancing operator"

$$m_j^{bal}(t,f) = \left[\frac{P_{peak}(t)}{P_{avg}(t,f)+\varepsilon P_{peak}(t)}\right]^{\frac{1}{2}} m(t,f) \quad (2)$$

which is applied to every trace in the data. In equation 2, ε is used to represent a prewhitening parameter. Whitening is a way of balancing and boosting the frequency spectrum. Harsh applications of the spectral prewhitening parameter (overwhitening) can boost noise and introduce ringing into the seismic data. The interpreter needs to carefully examine the data after spectral balancing to determine if the data are overwhitened.

An example of the effect of spectral balancing is shown in Figure 44, Figure 46, and Figure 48 below. Figure 44 shows the unbalanced seismic volume. In this figure, low frequency crosscutting energy can be seen at two way travel times greater than 3 seconds. Figure 46 shows the results of applying spectral balancing to the data. In the algorithm used to reconstruct the spectral data, an Ormsby filter is used. The low end of the Ormsby filter defines the lowest frequencies that will be included in the output image. Figure 48 is a separate iteration of spectral balancing that had a lower frequency for the Ormsby filter; 5 and 10 Hz were used. This allows low frequency to enter the data and the spectrum becomes overbalanced. Low frequency overbalancing is especially noticeable at depth, which likely means the low frequencies of overbalancing are “balancing” the low apparent frequency, steeply dipping noise.

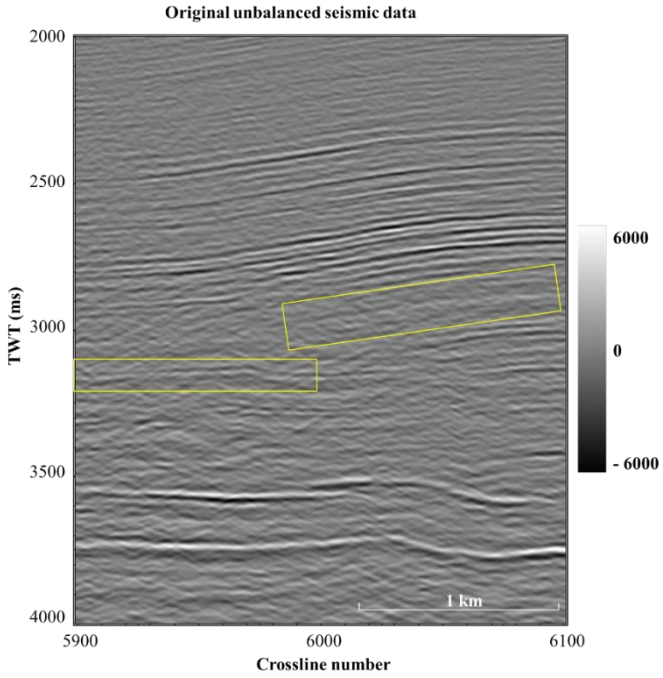

Figure 44. Inline 3130 through the original seismic data volume shows noise from 2 to 4 seconds of variable frequency, crosscutting energy of low frequency is prominent in this zone. Low frequency noise is also low amplitude and somewhat more challenging to see in the image.

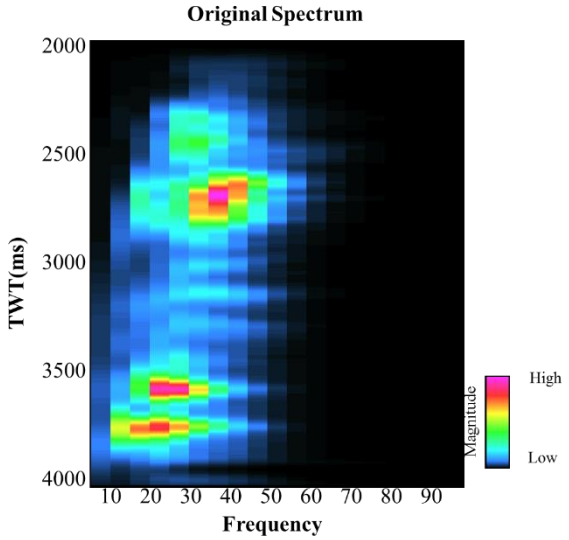

Figure 45. Time variant frequency spectrum of the original seismic data.

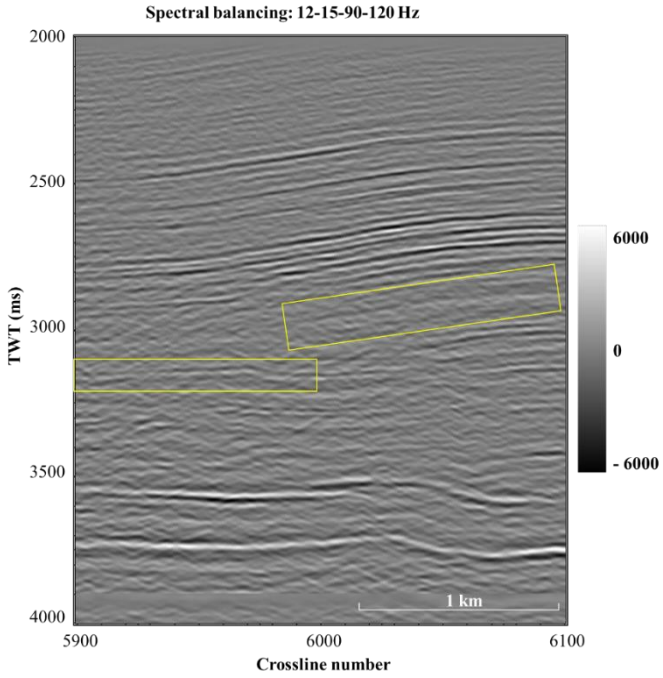

Figure 46. The spectrally balanced seismic data, with crosscutting low frequency noise reduced. A spectral balancing percentage of 1% was applied to the data. The reduction of low frequencies can best be seen when comparing the broad reflectors in the yellow rectangles. The low amplitude noise is represented by a very subtle change in the amplitude spectrum.

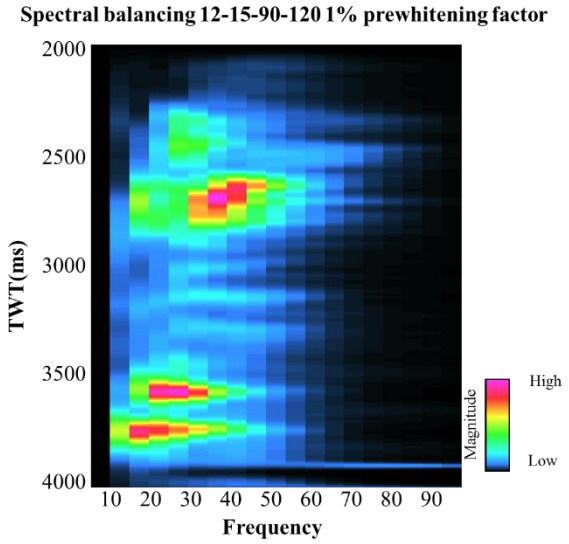

Figure 47. The seismic spectrum of the 12-15-70-120 Hz data shows a higher range of high frequencies, and higher magnitude of frequencies around 20 Hz.

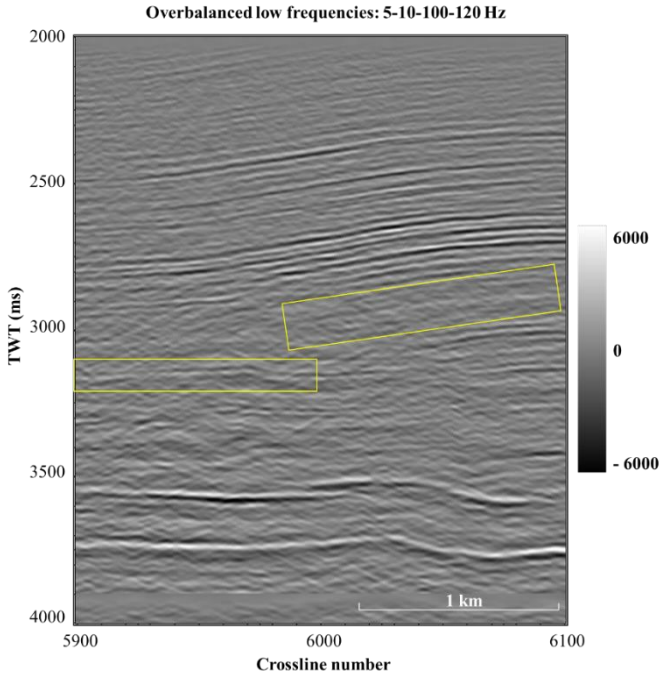

Figure 48. Seismic has overly boosted the low frequency migration aliasing noise. It is clear that I will need to apply a structure-oriented filter to suppress noise prior to spectral balancing.

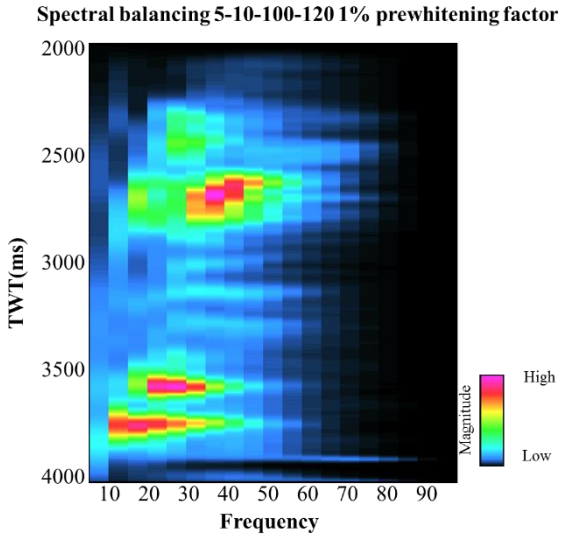

Figure 49. Seismic spectrum overbalanced towards low frequencies

Structural Oriented Filtering (SOF)

Structural oriented filtering is used to enhance the continuity of reflectors as well as otherwise obscured geologic features. Separating the dip azimuth of a reflector

from the dip azimuth of overlying noise is of utmost importance in performing structural oriented filtering. A combination of anisotropic diffusion (Hoecker and Fehmers, 2002) and Kuwahara filtering (Luo et al., 2002) provide the basis for SOF in this implementation. Several methods of filtering could also be used in conjunction with SOF including mean, median, and α-trimmed mean. However, principle-component, or Karhunen-Loeve (KL), filtering displayed the most desirable results.

Anisotropic Diffusion

Anisotropic diffusion (Hoecker and Fehmers, 2002) is the basis of structural oriented filtering algorithms. In Hoecker and Fehmers' work, they orient the filtering of seismic data along a seismic reflector, thus the anisotropic nature of the filter is defined by the filtering only parallel, and not perpendicular to reflector dip. Through iteration of the filtering, a "diffusive" element is implied in the algorithm.

Accurate dip and azimuth calculations are required to define the reflector plane upon which to smooth. Hoecker and Fehmers estimate dip and azimuth using a gradient structure tensor method. In this method, Hoecker and Fehmers compute the outer product of a gradient with itself then the elements are smoothed by a spatial dependent low-pass filter. The resulting matrix has three corresponding eigenvectors; the eigenvector with the largest corresponding eigenvalue will best represent the variability of the data and accordingly, will be aligned with the normal to the seismic reflector.

Kuwahara Filtering

Smoothing around discontinuities is done using Kuwahara filtering (Luo et al., 2002). The work of Luo et al. is based upon the research in the biomedical field of Kuwahara et al. (1976). A statistic such as standard deviation is calculated in

overlapping analysis windows in the data. The window with least semblance is understood to have the least noise, and is then used to guide smoothing. This minimum standard deviation value replaces the value of semblance at the original analysis point contained by the overlapping windows. Whereas a single window smoothing method such as a median filter could completely smooth a discontinuity feature, the overlapping windows of the Kuwahara filter allow the character of a discontinuity feature, in this case possibly a fault, to remain intact. Luo et al. (2002) also show how their filter can be used to suppress acquisition footprint, but warn of the adverse side effects of smoothing geologic features that are smaller than the required large window size.

Marfurt (2006) generalized on Luo et al.'s (2002) method by 1) using coherence rather than the standard deviation of the amplitude to find the optimum window, 2) using a principal component (KL) filter rather than an average, and 3) filtering along volumetric dip. A KL filter is applied to the window containing the analysis point that exhibits the highest coherence.

A Hybrid SOF Algorithm

In order to compare the alternative strategies of the Fehmer and Hoeker (2003) and Marfurt (2006) algorithm, Davogustto et al. (2011) implemented a hybrid algorithm that provides both options of not filtering (Fehmer and Hoeker) or shifting the filtering (Kuwhara) window depending on user defined coherence thresholds. This hybrid algorithm was tested on both modern and legacy data volumes and reasonable defaults set. However, none of these data volumes were as noisy as Pohukura3d, requiring significant investigation as to which parameters work best.

Application to the 3D Volume

Crosscutting noise affects the dip volume that was used to guide the structural oriented filtering. Multiple half window sizes were tested when computing the dip volume, including 0.006 s, 0.02 s, 0.03s, 0.04 s, and 0.05 s. A window size of 0.04 seconds was used to reduce the effects of the highly dipping noise; this window size smoothed the data but still maintained the dipping reflectors character. The larger window size allows more reflectors to contribute to a smoother dip image.

In the Pohokura 3D survey, after rigorous testing, the threshold similarity (used in place of coherence) values used in SOF and as well as the vertical window size for strongly impacted the resulting continuity of reflectors while preserving edges. Similarity ranges between 0 and 1, with 1 being coherent and 0 being totally random. Given the high noise level in these data, it is difficult to discriminate between low similarity anomalies due to steeply dipping faults and low coherence anomalies due to steeply dipping migration aliasing artifacts. For this reason, the Hoecker and Fehmer's fault preservation construct (do not smooth over low values of coherence) fails. I therefore lower the default threshold values of similarity, and apply the Kuwahara filtering for all values $c>0.3$ (details in the appendix). To avoid the "patchiness" of Kuwhara filtering, Davogustto et al. (2011) also introduced a threshold value of coherence above which a centered window will be used in smoothing. I set this value to be $c=0.8$, lower than default value to account for the noise in the data.

Parameters described in the previous paragraph are "Kuwahara aggressive". The result is evident in Figure 51 which shows the first iteration of structural oriented filtering on the seismic data. This filtering does cause the data to appear somewhat

patchy in certain areas, however it also sharpens geologic features. The blue ellipse in Figure 51 shows the appearance of listric fault-like features. In Figure 52, the features in the blue ellipse are sharpened further and a fault block is delineated as highlighted by the yellow arrows. Figure 53 shows the third iteration of SOF on the original seismic data. Figure 57 is the Sobel filter similarity of the original seismic data, fault lineaments are visible, but somewhat smooth. Figure 59, showing a timeslice of the Sobel filter similarity of the 2nd iteration of SOF, is an excellent example of the sharpening that aggressive SOF parameters produce. This image sharpens discontinuity features further, but as highlighted by the red and purple ellipses, this sharpening may not be of purely geologic features. In the purple ellipse regular periodic noise is highlighted. This could be related to acquisition or the survey design, or it could be a periodic feature caused by the dip of the reflector that is being enhanced inaccurately. Polygonal discontinuity features in the red ellipse in the upper right corner of the timeslice could be interpreted as polygonal faulting. Polygonal faulting is closely linked to shale dewatering. However, these features also closely resemble “paint-by-numbers” artifacts associated with Kuwahara filtering. Qi et al. (2015) identifies this artifact in his work using the Kuwahara filter (Figure 62). Not much change is apparent in either timeslice or inline from the second iteration to the third iteration which is a good indication that no more iterations are necessary. The discontinuity features are still enhanced and highlight in some areas what could be geologic features. While these faults may appear somewhat suspicious, it is important to remember that after multiple iterations of structural oriented filtering data from outside of the specific inline is being used in the edge enhancement. Additionally, the trace window is only including 49 traces after 3

iterations. This size is indicated by the yellow square in the last image. The size of this window implies that interpreted fault lineation is indeed geologic. Noise from such a small window would not organize in such a geologic pattern as the one seen in Figure 60.

In Figure 54, I spectrally balance the structure-oriented filtered data shown in Figure 52. Suprisingly, the sharp fault edges are muted. Further investigation indicates that these enhanced edges include spectral components beyond 100 Hz, that is, components that were created by the Kuwahara filter. Since such sharpening is very useful in subsequent fault enhancement and manual interpretation, I modify my filtering workflow to that shown in Figure 55.

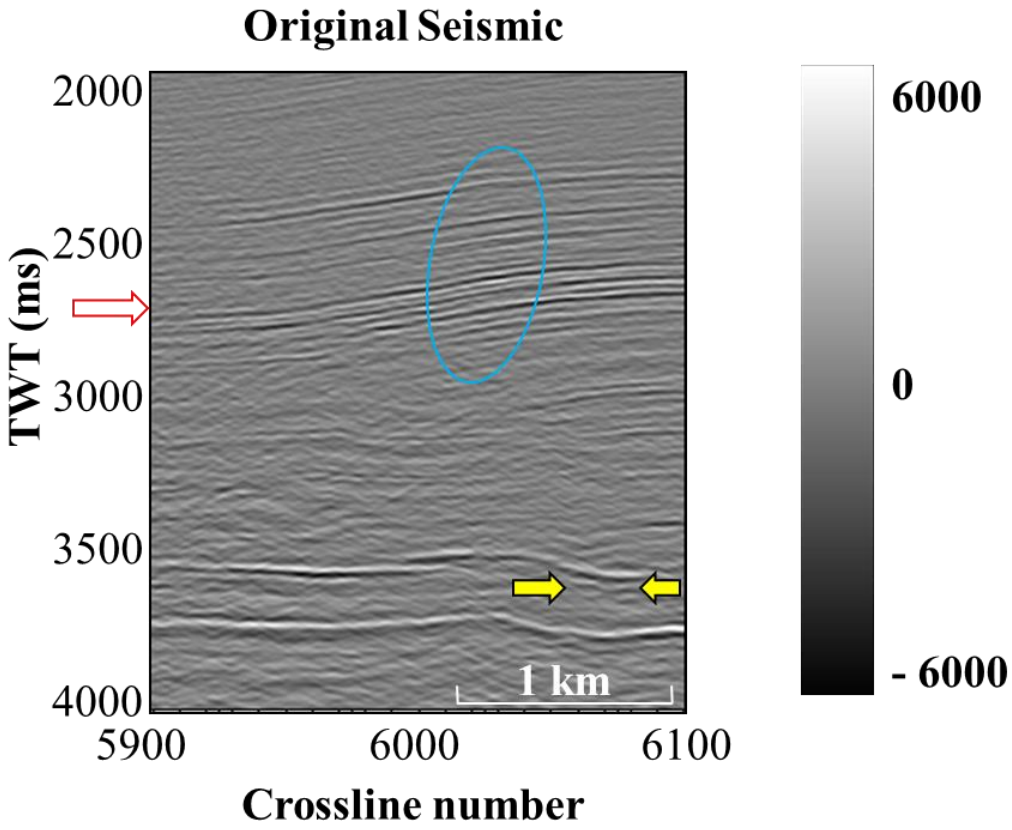

Figure 50. Inline 3130 through the original 3D seismic data volume. The blue ellipse is highlighting an apparently unfaulted zone of interest that becomes more discontinuous in subsequent iterations of SOF shown in the next images. Yellow arrows highlight another area in which more structural complexity is imaged with further iterations.

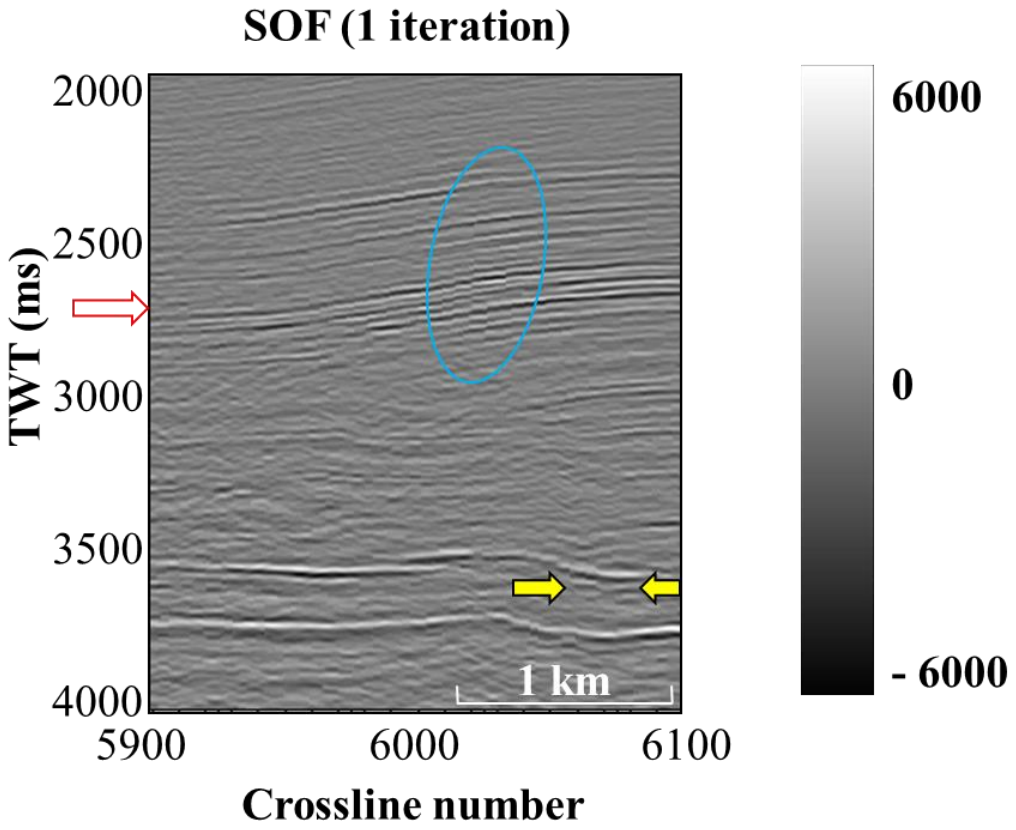

Figure 51. Inline 3130 through the seismic volume, after 1 run of structural oriented filtering. Crosscutting artifacts below 3 seconds are reduced. The discontinuities through the reflectors in the blue ellipse become apparent. In between the yellow arrows, curved discontinuities are present in the reflector.

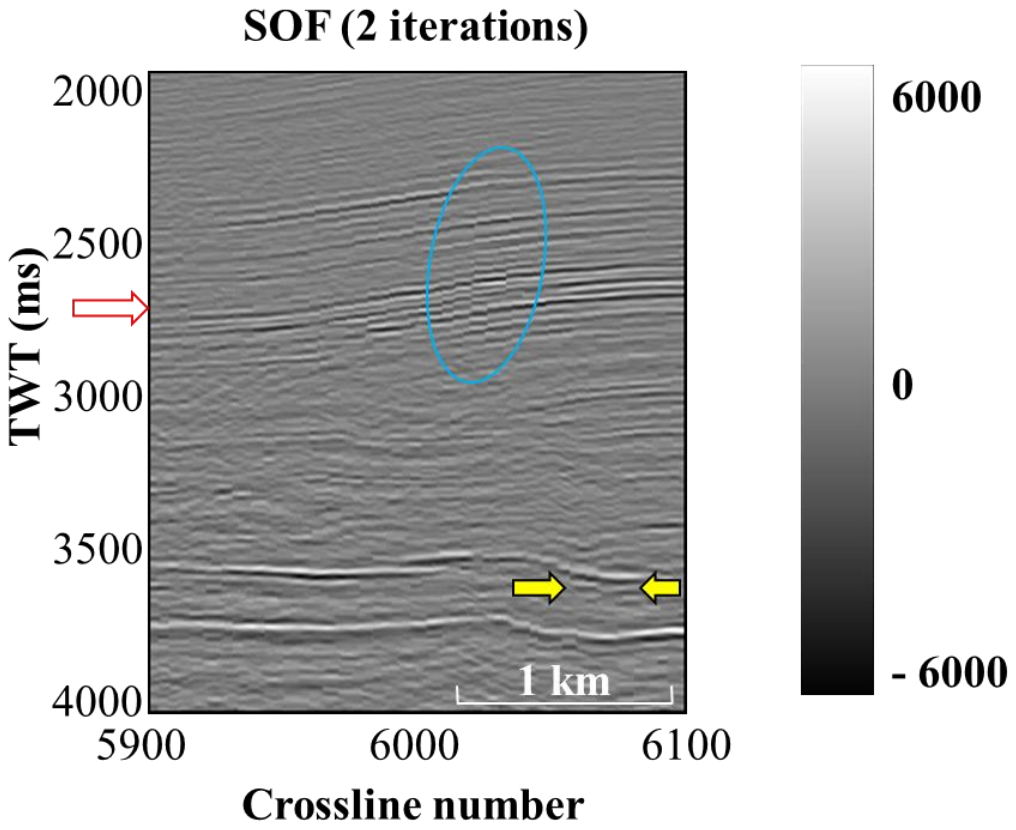

Figure 52. Inline 3130 through the second iteration of structural oriented filtering. Discontinuities in the blue ellipse that first became apparent in the previous figure are sharpened further. Between the yellow arrows, a rotated fault block is imaged between two listric faults.

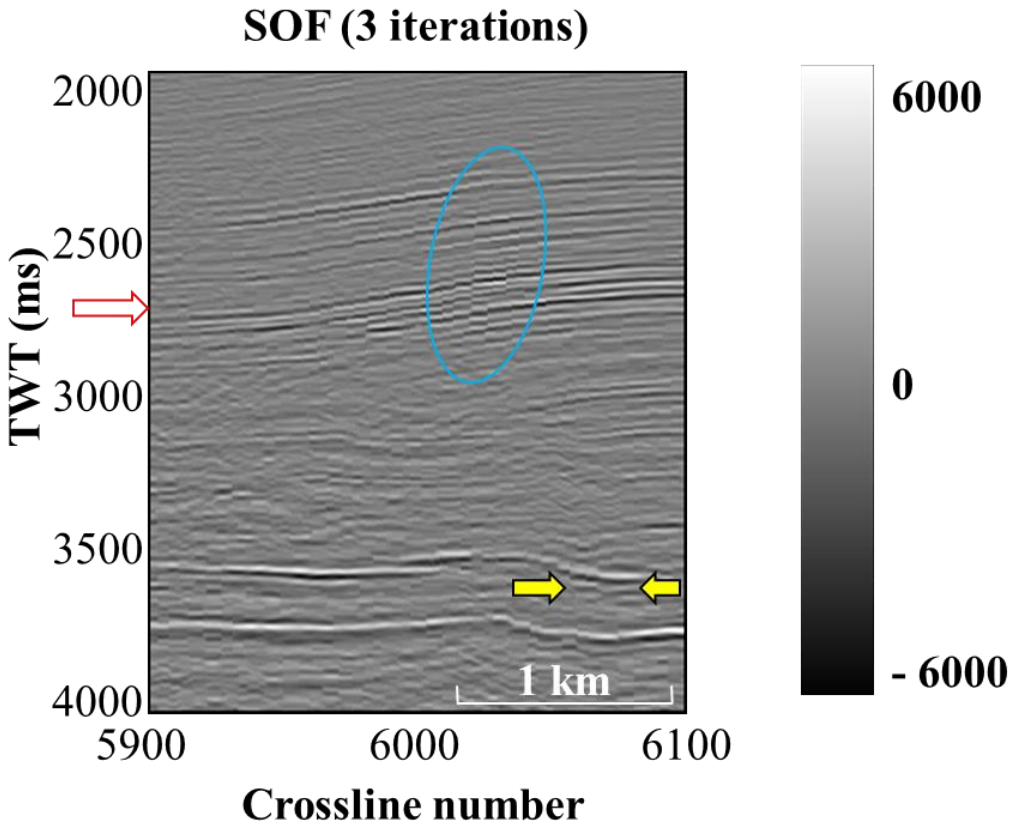

Figure 53. Inline 3130 through a third iteration of structural oriented filtering. Overall not much change occurs between iteration 3 and iteration 2, this indicates that 2 iterations is likely a good interpretation volume to use.

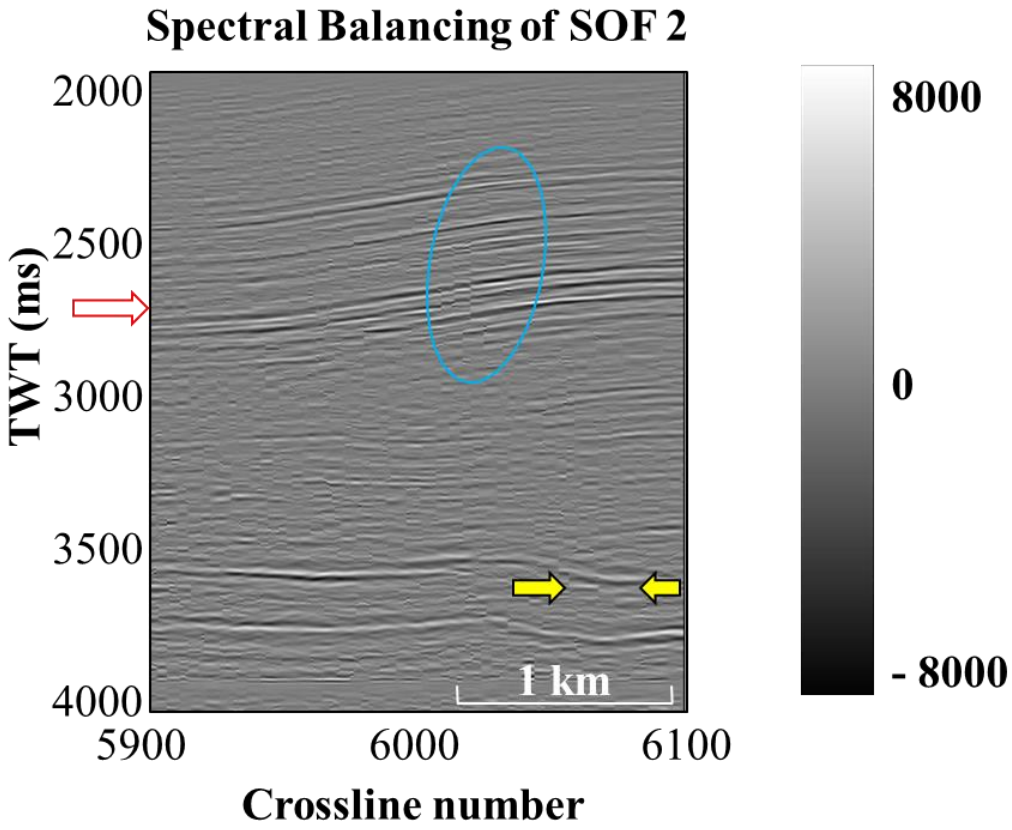

Figure 54. Spectral balancing on the third iteration of structural oriented filtering. The lower points of the Ormsby filter applied are 8 and 12 Hz. Computing spectral balancing exposes some of the 'faults' that began appearing in the first iteration of SOF as noise. It is interesting to note that because of these features were removed by spectral balancing they were associated with specific frequencies outside the bandwidth of the spectral balancing, either below 12 Hz or the upper point of the Ormsby filter, 100 Hz.

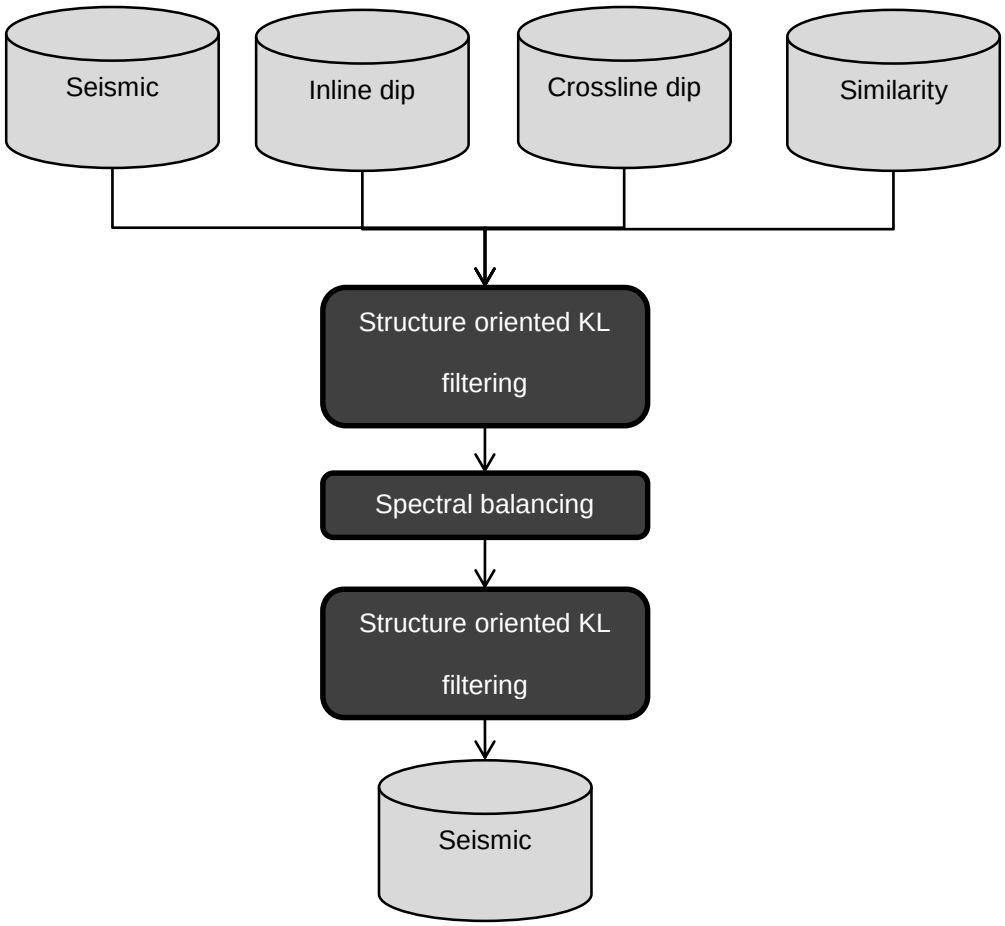

Figure 55. The final data conditioning workflow applied to the Pohokura 3D volume.

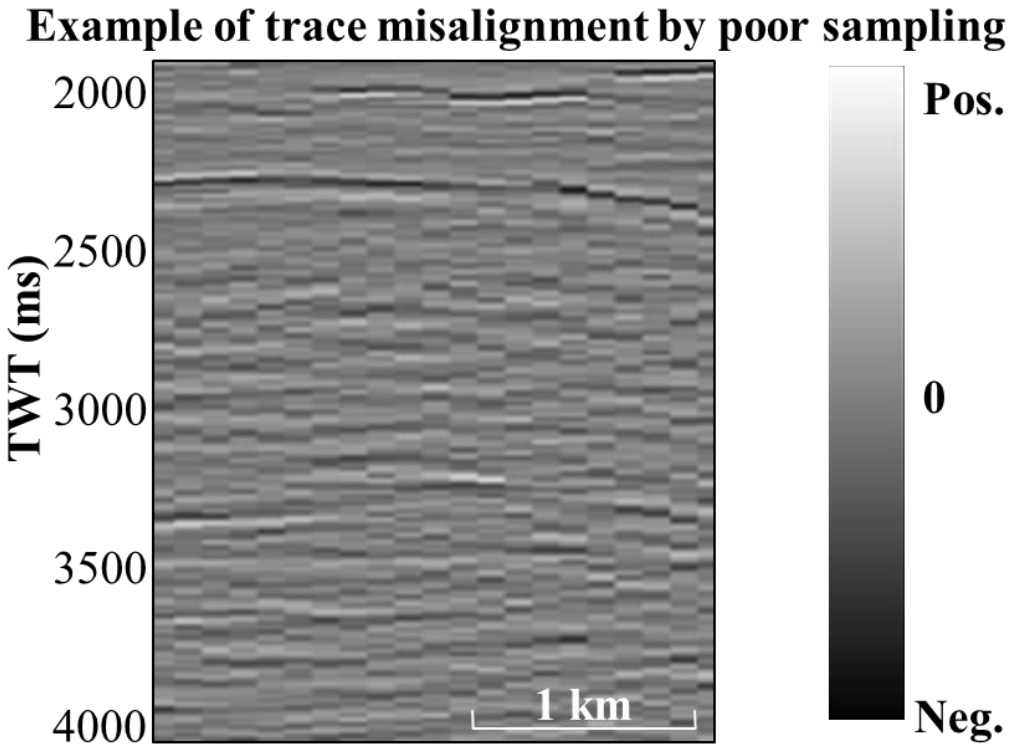

Figure 56. An example of noise from poor sampling of the data. For this 2D line, traces were sampled every 10 CDP instead of every CDP. The result is strictly vertical lineations through the data exaggerating the discrepancy between every ten traces. If discontinuity features sharpened by SOF were not real, we would expect them to appear strictly vertical like this.

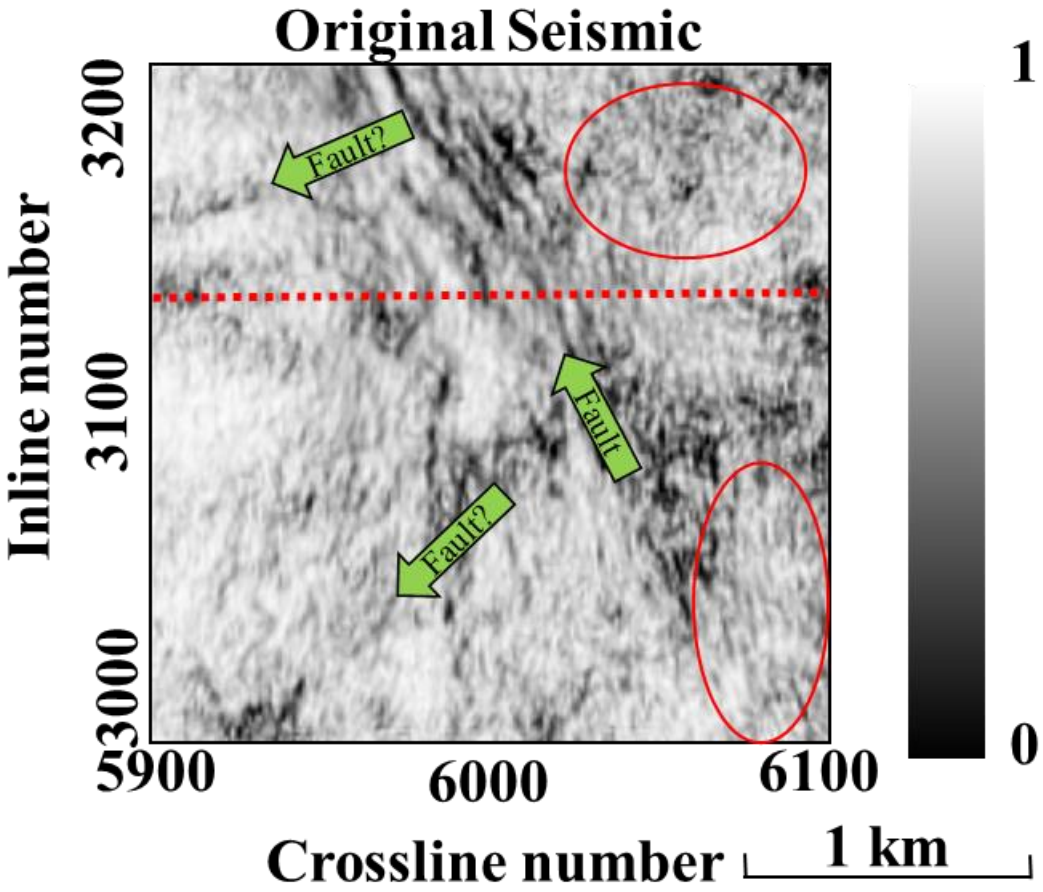

Figure 57. Timeslice through the original seismic data volume at 2.8 seconds. Faults or possible faults are featured with green arrows. In the red ellipses zones of noise are outlined. The dotted redline shows the orientation of inline 3130 used in previous figures.

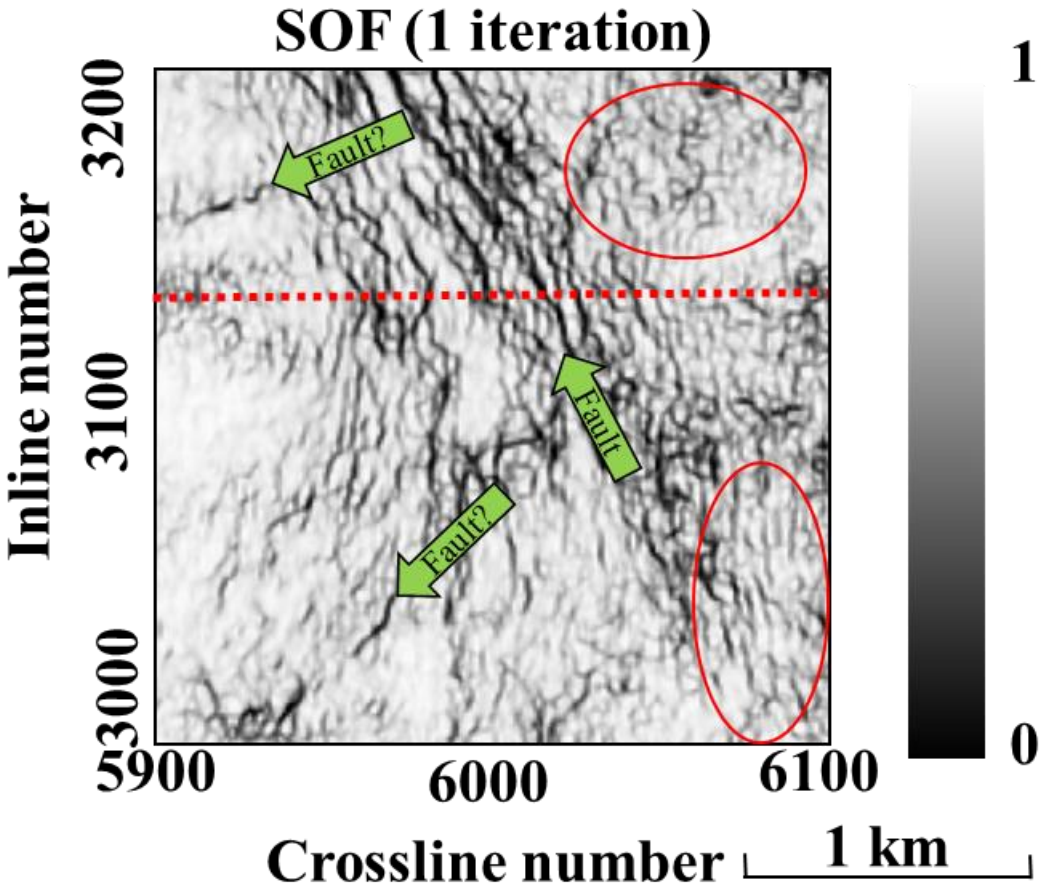

Figure 58. Timeslice through the variance of 1 run of structural oriented on the filtering at 2.8 seconds. Sobel filter similarity is used in this image instead of seismic amplitude of the SOF volume, because it does a sufficient job of emphasizing discontinuities that are sharpened by SOF.

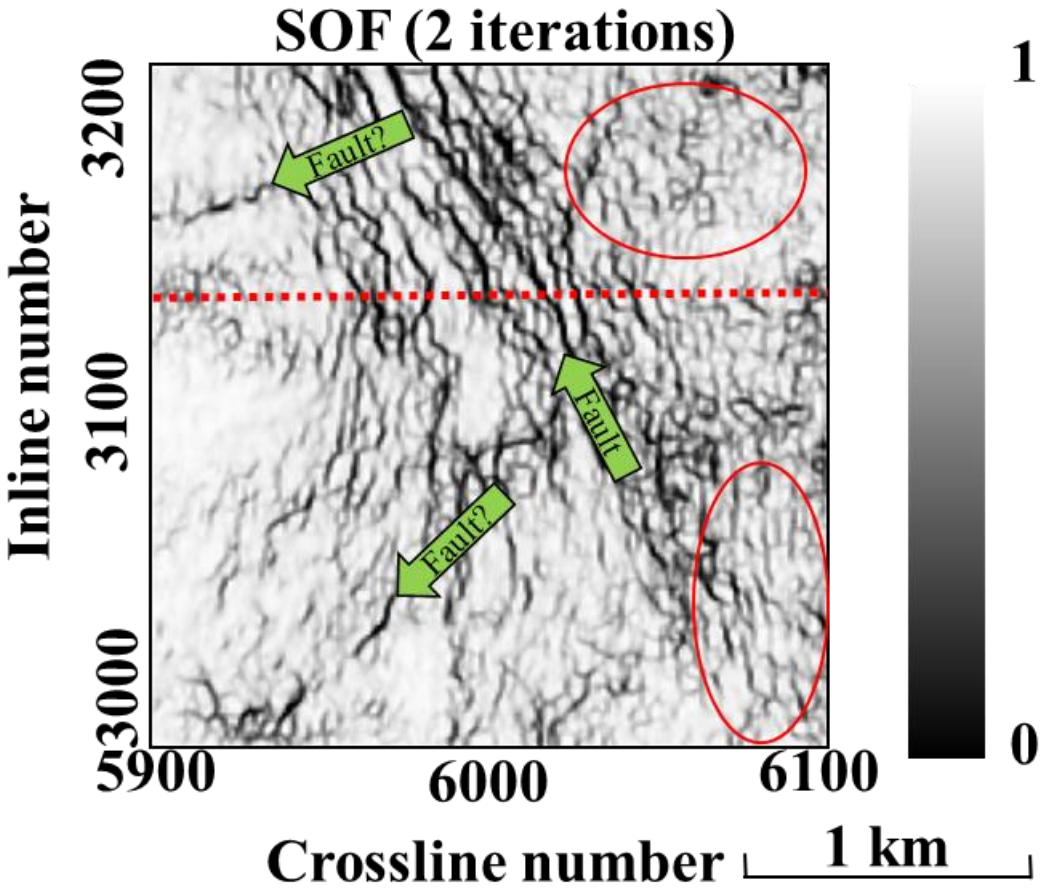

Figure 59. Timeslice through 2 iterations of structural oriented filtering at 2.8 seconds. Discontinuity features are becoming further sharpened and laterally discontinuous features indicated by the green "Fault?" arrows are becoming more continuous. The "Fault" arrow indicates a long continuous fault lineation which is also becoming more continuous with successive iterations. The red ellipse in the upper right of the image highlights "paint-by-number" features, a known side effect of Kuwahara filtering. In the bottom right ellipse, another possible artifact is sharpened. Periodic lineations along the inline direction are exaggerated.

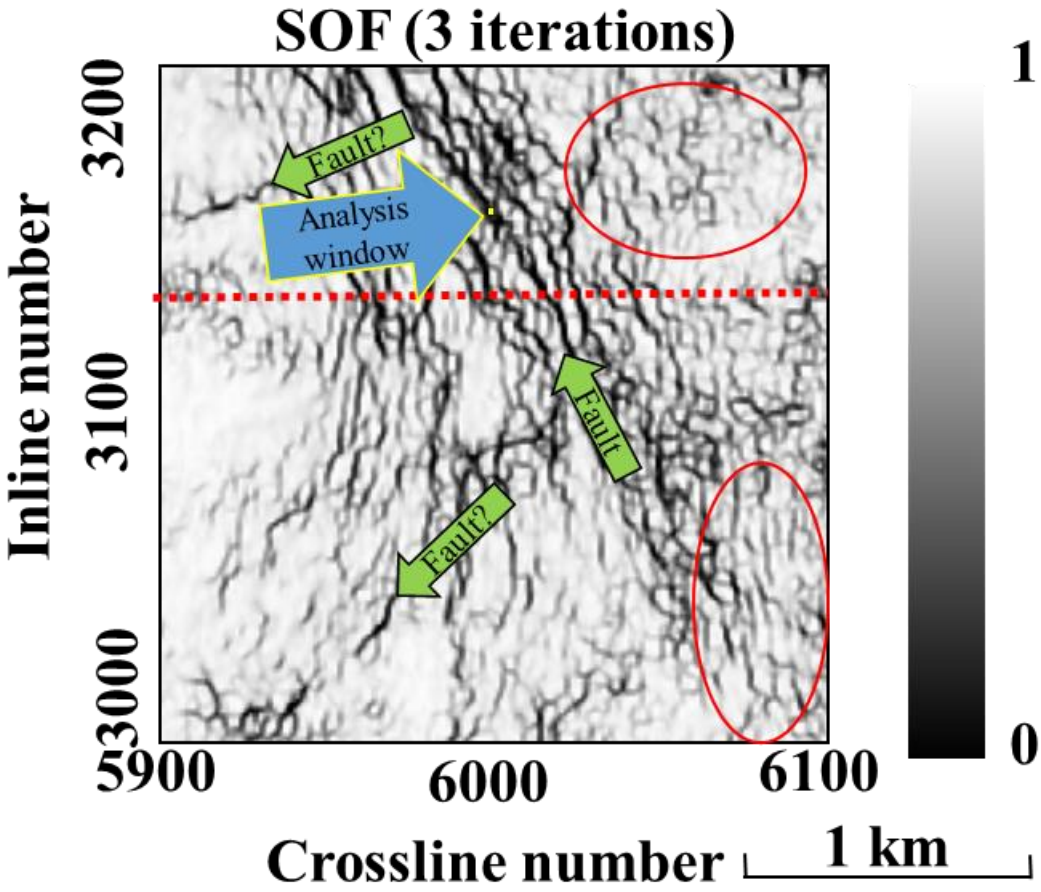

Figure 60. Timeslice through 3 iterations of structural oriented filtering at 2.8 seconds. Along the dominant fault lineation, a yellow square that is roughly the size of a 7x7 trace analysis window is shown. This is shown to emphasize the true geologic nature of the discontinuity features that are being sharpened. As the analysis window only works locally, if these features were noise they would not organize in such a geologically plausible manner on a regional scale.

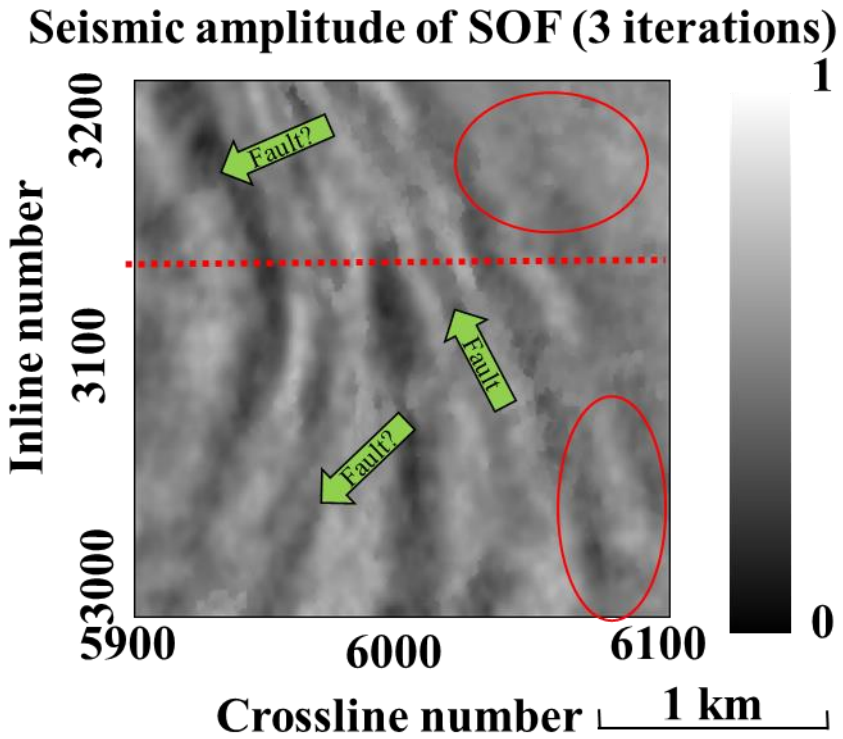

Figure 61. Seismic amplitude data after 3 iterations of SOF. Data is noticeably smoother.

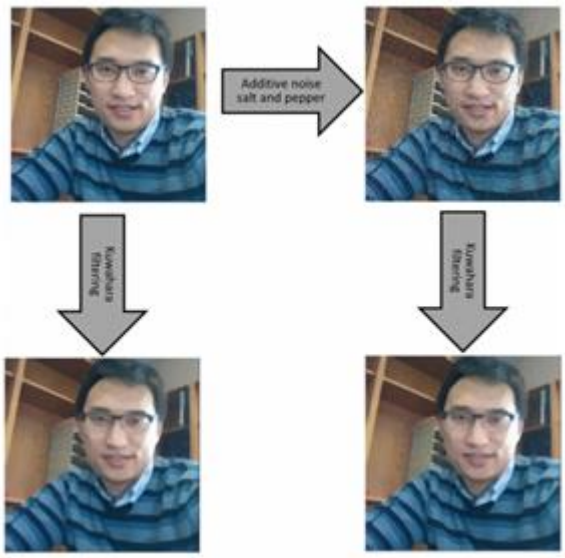

Figure 62. Effects of the Kuwahara filter from Qi et al. (2016). Smoothing by the Kuwahara filter causes polygonal "paint-by-numbers" features to be highlighted. These features appear as polygons of different amplitudes, as if they were painted by different colors.

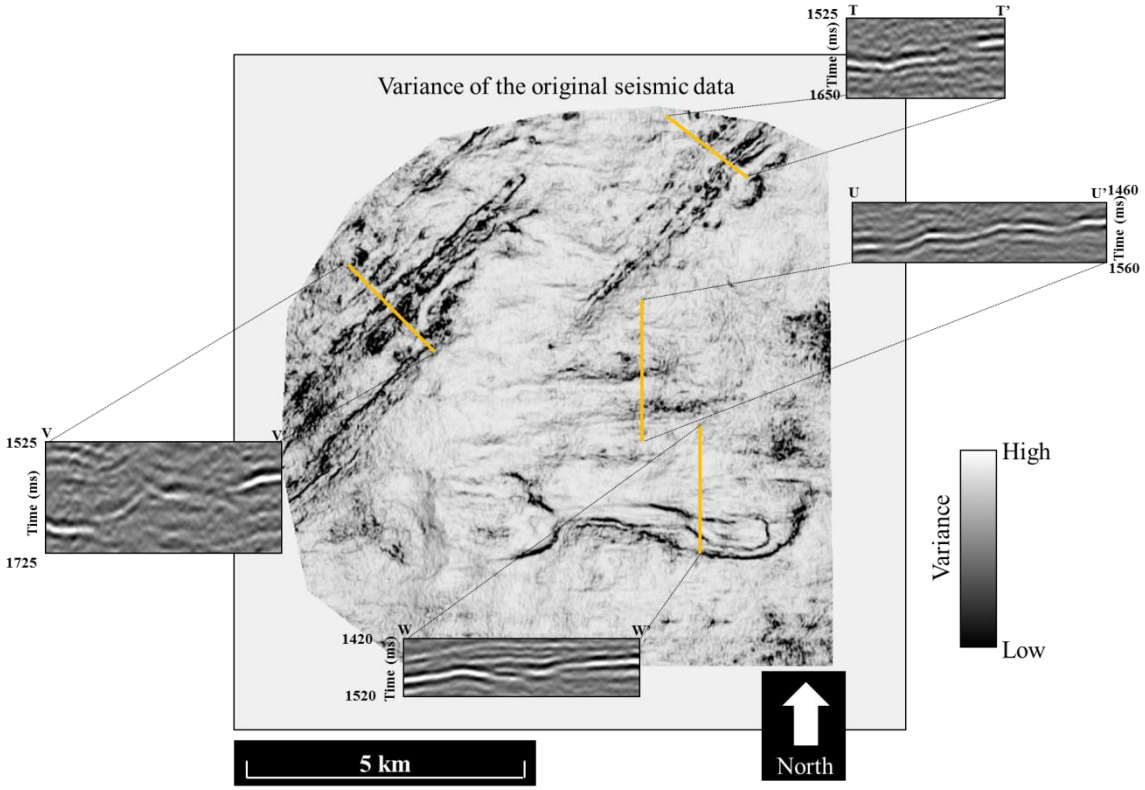

Figure 63. Along the U0SB surface, vertical sections through the data highlighting TT' crosscutting noise in a faulted section of the data, UU' an undulatory surface that could be associated with en echelon faulting, but no offset of the reflector is imaged, VV' a slump feature possibly associated with a mass transport complex, and WW' a faulted zone that is poorly imaged due to diffractions from fault shadow.

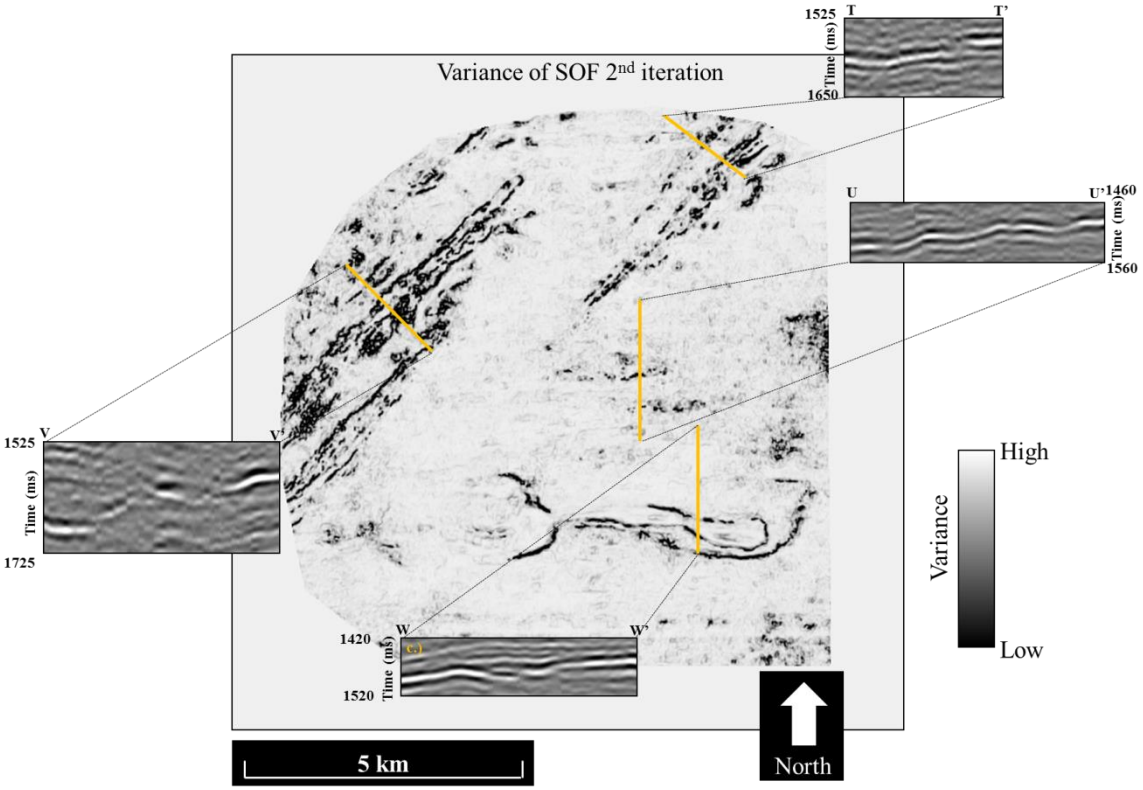

Figure 64. Horizon slice along the U0SB surface through the variance of the structural oriented filtered volume. Cross sections through the seismic volume in TT' showing increased reflector continuity and sharpening of faults. In UU' an undulatory feature shows a listric fault that does not appear in figure UU' of the previous image, and crosscutting noise is diminished. A decrease in crosscutting noise is again seen in VV' In WW' structural oriented filtering has enhanced the continuity in a region where a diffraction hyperbola otherwise skewed the reflector.

Discussion

2D attribute mapping and interpretation

Interpolation is required over large distances to create 2D map surfaces. Thus, if a geologic feature is constant over a large distance, i.e. 1 km, then the feature is likely to be mapped accurately in 2D. Time structure surfaces are the most reliable between 2D and 3D maps. These surfaces depend only on the consistency of a horizon pick along a reflector.

Data Conditioning

Structural oriented filtering is used to sharpen discontinuity features in seismic data, increase reflector continuity, and make interpretation of geology a less challenging task. While, in the P95 2D seismic survey, reflector continuity was increased, in the Pohokura 3D seismic volume, structural oriented filtering significantly reduced the prominence of crosscutting energy and increased the effectiveness of autopickers in horizon tracking.

In the 3D seismic volume, discontinuity features begin to appear within the Pohokura survey after the first run of SOF. Further iterations of SOF sharpen the features, but the question remains as to whether the features are true geology or enhanced artifact. A thorough understanding of the background geologic model is useful in identifying if the faults are real or seismic artifacts. However, an interpreter must be aware of features such as these when interpreting on a seismic volume which has undergone SOF.

Argument for geology

As with any attribute or conditioning performed on seismic data, it is important to consider if the result is meaningful and faithful to the original data. Parallel faulting is apparent in the blue ellipse of Figure 51 through Figure 54. The faults begin appearing after the first iteration of structural oriented filtering. Faults sharpened around 2.8 seconds and a deeper fault block marked by yellow arrows at close to four seconds of depth have a reasonable listric shape and even show some rotation into the fault. The shallower faults about 2.8 seconds converge and do not appear to be periodic discontinuities that would cause a more regular vertical linear feature, as in Figure 56. Since the goal of structural oriented filtering is to smooth along reflectors and preserve edges or, in a more general sense, smooth horizontally and sharpen vertically. Armed with this knowledge, we accept that these faults' appearance is plausible.

Argument against geology

Piecewise vertical discontinuities can be suspicious. Additionally, why reflectors become more discontinuous in certain areas after several iterations of SOF - when one of the primary goals of SOF is to increase reflector continuity - is quite perplexing.

Further testing could prove the true nature of these expressions. If they are shale dewatering features they can be enhanced by a fault enhancement filter such as the directional Laplacian of a Gaussian (Machado et al., 2016). Additionally, footprint suppression could be run on the SOF volume, and if the artifacts are periodic, they will be isolated. The features could also be related to spatial aliasing of the data and exaggeration by SOF, however Figure 56 shows what exaggerated trace offset looks

like. This artifact appears as more of a distant cousin of the discontinuity features in the Pohokura 3D seismic data, not as the same type of feature.

Conclusions

Seismic attributes work best when they extract and highlight features in the data that might otherwise be overlooked. In large 3D surveys, attribute time and horizon slices provide excellent images of tectonic deformation and depositional environment without manual interpretation. By its nature, the number of seismic lines in a 2D survey is smaller than the number in 3D surveys covering the same acreage such that the interpreter has the time to inspect and manually interpret each line. For this reason, a seismic attribute must quantify information that might otherwise be overlooked. Geometric attributes that add value to 2D interpretation include those that delineate faults and unconformities, such as coherence. Single trace attributes that add value include time-frequency spectral analysis and cosine of instantaneous phase. Other attributes such as RMS amplitude and volumetric curvature (in 2D, apparent, or Euler) add little to the interpretation process.

Maps still form a key component of any drilling decision. While modern commercial software makes good maps from picked time horizons, it seems to have lost the flexibility of making maps from attribute extractions that existed in older software when 2D surveys were more common. Specifically, there does not appear to be an effective means of kriging extracted values to use an anisotropic variogram defined by the time-structure map.

Interpolating short wavelength, edge-sensitive attributes such as coherence may never be possible. For this reason, we cannot hope to approach the clarity of channels, slumps, and other stratigraphic features seen on 3D data. Features smaller than the line separation, such as pockmarks and small pinnacle reefs may be totally missed if they

fall between the seismic lines. Nevertheless, good time-structure maps generated from 2D data have considerable value. Long wavelength horizon curvature generated by such maps are also quite useful.

The revolution in seismic stratigraphy began with long regional lines acquired in the 1970s. Interpreters mapped packages on these lines and then hand mapped the distribution of these packages between lines. While coherence is too short wavelength to interpolate between lines, other, longer wavelength stratigraphy measures such as the magnitude of reflector convergence (but not its azimuth) and disorder should make useful maps. Finally, recent advantages in seismic chronostratigraphy and automatic picking of reflectors within an interpreter-defined package should generate a multiple of new time-structure and time-thickness maps.

In summary, many seismic attributes are reliable for interpretation on 2D seismic lines. An average spacing of 1 km between lines leaves a lot of room for error in interpolation. As such, 2D lines are reliable for interpretation of regional geologic structures, such as the Pohokura anticlinal structure. Subtle features such as smaller scale faults and stratigraphic features with great variation cannot be seen with confidence in 2D interpolated surfaces.

At shallow depths of 0 to 1000 ms, 2D data appears higher resolution than 3D seismic data. This could be an effect of higher fold at shallow depth of 2D data than 3D seismic data. At depths greater than 1400 ms, 3D seismic data is higher resolution and is likely related to the increased azimuths and offsets being binned in 3D data at greater depths.

Post stack data conditioning can reduce the effects of crosscutting migration artifacts and smooth reflectors contaminated by such noise. In particular, structural oriented filtering imaged discontinuity features that were not present in the original seismic data. A 3D search window integrates data from multiple seismic lines to better image discontinuities. However, the sharpness of the dipping edge was found to expand the frequency spectrum past 100 Hz. Spectral balancing with an applied Ormsby filter of 8-16-90-120 Hz removed some of the newly imaged discontinuity features and emphasized that a relationship exists between discontinuity features and specific frequencies.

References

Bahorich, M. S. and S. R. Bridges, 1992, Seismic sequence attribute map (SSAM): 62nd Annual International Meeting of the SEG, Expanded Abstracts: 227-230.

Bancroft, J.C., 2009, Comments on diffraction modelling: CREWES Research Report, **21**.

Barnes, A.E., 2000, Attributes for automated seismic facies analysis: 70th Annual International Meeting, SEG, Expanded Abstracts, 553-556.

Biondi, B., 2007, Concepts and applications in 3D seismic imaging: 2007 Distinguished Instructor Short Course, No. 10.

Brown, A. R., 2011, Interpretation of three-dimensional seismic data, 7th edition: AAPG Memoir 42, SEG Investigations in geophysics, No. 9.

Browne, G. H. and R. M. Slatt, 2002, Outcrop and behind-outcrop characterization of a late Miocene slope fan system, Mt. Messenger Formation, New Zealand: AAPG Bulletin, **86**, 841-862.

Chopra, S. and Marfurt, K.J., 2007, Seismic attributes for prospect identification and reservoir characterization: SEG geophysical developments series, No. 11.

Chopra, S. and Marfurt, K. J., 2016, Spectral decomposition and spectral balancing of seismic data: The Leading Edge, **35**, 176-179.

Crowley, J. and S.J. Crocker, 1989, Well completion report Okoki-1 PPL38438, Ministry of Economic Development New Zealand unpublished petroleum report.

Dubrule, O, 2003,Geostatistics for seismic data integration in earth models, 2003 Distinguished instructor short course, No. 6.

Davogustto, O., 2011, Removing footprint from legacy seismic data volumes: M.S. Thesis, University of Oklahoma.

Evans, B. J., 1997, A Handbook for Seismic Data Acquisition In Exploration: Geophysical Monograph Series.

Falconer, S. and K.J. Marfurt, 2008, Attribute-driven footprint suppression, 78th Annual International Meeting, SEG, Expanded Abstracts, 2667-2671.

Fehmers, G., and F. W. Höcker, 2003, Fast structural interpretation with structure-oriented filtering: Geophysics, 68, 1286–1293.

Herron, D., 2016, A simple procedure for handling misties on 2D migrated seismic lines: (To appear in Interpretation).

Hilterman, F. J., 1982, Interpretative lessons from three-dimensional modeling: Geophysics, **47**, 784-808.

Lindsey, J.P., 1989, The Fresnel zone and its interpretative significance: The Leading Edge, **8**, no. 10, 33-39.

Lendzionowski, V., Walden, A.T., and R.E. White, 1990, Seismic character mapping over reservoir intervals: Geophysical Prospecting, **38**, 951-969.

Luo, Y., al-Dossary, S., and M. Marhoon, 2002, Edge-preserving smoothing and applications: The Leading Edge, 21, 136–158.

Hansen, R. J., and P. J. J. Kamp, 2004, Late Miocene to early Pliocene stratigraphic record in northern Taranaki Basin: Condensed sedimentation ahead of Northern Graben extension and progradation of the modern continental margin: New Zealand Journal of Geology and Geophysics, **47**, 645-662.

Marfurt, K., 2006, Robust estimates of 3D reflector dip and azimuth: Geophysics, **71(4)**, 29-40.

Palmer, J., 1985, Pre-Miocene lithostratigraphy of the Taranaki Basin, New Zealand: New Zealand Journal of Geology and Geophysics, **28**, 197-216.

Pigott, J.D., Kang, M.H., and H.C. Han, 2013, First order seismic attributes for clastic seismic facies interpretation: examples from the East China Sea: Journal of Asian Earth Sciences, **66**, 34-54.

Roberts, A., 2001, Curvature attributes and their application to 3D interpreted horizons: First Break, **19**, 85-100.

Rotzien, J. R., Lowe, D. R., King, P. R., and G. H. Browne, 2014, Stratigraphic architecture and evolution of a deep-water slope channel-levee and overbank apron: The Upper Miocene Upper Mount Messenger Formation, Taranaki Basin: Marine and Petroleum Geology, **52**, 22-41.

Ulrych, T., Sacchi, M., Graul, M., and M. T. Taner, 2007, Instantaneous attributes: the what and the how: Exploration Geophysics, **38**, 213-219.

Taner, M.T., 2001, Seismic attributes, CSEG Recorder, 48-56.

White, R.E., 1991, Properties of instantaneous seismic attributes: The Leading Edge, **10**, no. 7, 26-32.

Appendix A: Illumination

The Fresnel Zone

Application of theoretical wave tracing to seismic data, and the spatial resolution at a point in the subsurface can be related to the energy recorded at a receiver. However, in considering reflection seismology in the sense of a seismic wavefront, it becomes apparent that the energy from a "point" is actually generated over an area by integration (Lindsey, 1989).

Lindsey (1989) defines the Fresnel zone as the "area of constructive reflection accumulation surrounding the ray theory reflection point". Thus, the size of the Fresnel Zone is inversely related to the lateral resolution. If geologic features, such as channel-levee systems or overbank deposits are smaller than the Fresnel zone then they will appear as a smeared image prior to seismic migration.

Traditionally, the Fresnel zone has been thought of in a 2 dimensional sense, however, it is more accurate to define the Fresnel zone in 3 dimensions as a circle (for flat reflectors) along a reflector with a specific diameter. The diameter of the Fresnel zone is defined by a threshold where the pathlength differs by a significant amount from the zero offset seismic response. The diameter of the Fresnel zone is defined in two popular ways, one by Sheriff (1980), and a second by Berkhout (1984). Sheriff defines the diameter of the Fresnel zone as being bounded by the point where the pathlength from reflector to CMP is one quarter wavelength out of phase with the zero offset reflection from the point of interest. Because we are considering two-way travel, the reflection bounding the Fresnel zone would then be one half wavelength out of phase with the zero offset reflection. Berkhout defines the limit as the point where the

pathlength is one eighth wavelength out of phase with the direct reflection, creating a reflection response that is one quarter wavelength out of phase. Figure A1 illustrates the differences in pathlength in relation to the direct reflection as well as lists Sheriff and Berkhout's criteria.

Since the Fresnel zone is a numerical approximation, there is not abrupt cutoff in the size of the diameter. As such, Sheriff or Berkhout's Fresnel zone diameter criteria are both viable options. As a matter of choice, I will use Sheriff's equation,

$$F_{Sheriff} = 2\sqrt{(z + \frac{\lambda}{4})^2 - z^2} \quad \text{(A1)}$$

where z is the depth of the reflector of interest and λ is wavelength. However, this equation is challenging to apply because the units are in terms of length, not time. A substitution of $\frac{VT}{2}$ for z and $2V\tau$ for λ relates the equation to time. In these substitutions V is the RMS velocity to the reflector of interest, T is the two-way traveltime, and τ is the half period of the dominant frequency. Substituting these values in, we arrive at

$$F_S = 2\sqrt{(\frac{VT}{2} + \frac{V\tau}{2})^2 - (\frac{VT}{2})^2} \quad \text{(A2)}$$

which is dependent on time values instead of depth, so no depth conversion of the seismic is necessary for this calculation. Making the assumption that $\tau << T$ and regarding the $V^2\tau^2$ term as negligible, a simplified equation

$$F_S = V\sqrt{2T\tau} \quad \text{(A3)}$$

is formed. Velocity, two-way traveltime, and half period length of the dominant frequency can all be measured or estimated in seismic time volumes and an estimation of the Fresnel zone diameter can be calculated.

Hilterman (1982) investigates how the lateral size, of what he terms “Fresnel zone reflectors” alter the wavelet response in 2 dimensions. In Hilterman’s model, Fresnel zone reflectors are discs of varying size at a specified depth of which he finds the wavelet response. Hilterman shows that diffraction events at the edge of his models constructively interfere to form a high amplitude reflector at the center of the disk. Through this example Hilterman states that the lateral extent of a reflector imaged at zero offset in un-migrated data can be defined by one half of the maximum amplitude of the event. Hilterman goes on to make the comparison of small spatial Fresnel zones to thin beds because of tuning these aforementioned effects.

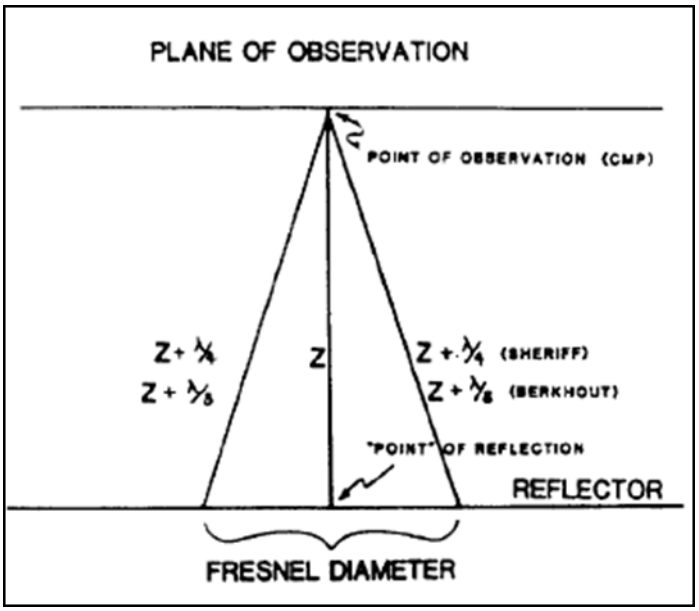

Figure 65. Illustration of the Fresnel zone as defined by Sheriff and Berkhout. Fresnel zone diameter as defined by Berkhout is the zero offset response plus one eighth the wavelength. Sheriff’s response is used in this document, and states the Fresnel zone diameter is bounded by the circle with the reflection response that is one fourth wavelength longer than the zero offset response (Lindsey, 1989).

Leverage of offset against multiples

Water bottom multiples are common in marine data. They are caused by a seismic wave reflecting off the water bottom then back to the receiver. However, one approach to dealing with water bottom multiples is having longer offset data. At longer offsets the moveout of faster seismic reflections is less than the moveout of slower multiple events. During processing of the data, when NMO is applied to the data, the primary reflectors will flatten, but multiples will show a residual dip. When the data is NMO stacked, the primary reflection will constructively stack, while the multiple will attenuate. The difference in moveout occurs because the multiple has a different average velocity than the primary reflections. A multiple will travel two or more times through a (generally slower) shallow velocity media, while a primary reflection arriving at approximately the same time travels through (generally faster) deeper layers. Therefore, a longer cable length in marine acquisition is ideal for separating multiples from primary reflections and can aid in the process of multiple suppression. The cable length used in the P95 2D seismic data acquisition of 4000 m is of sufficient length as multiples appear to be at a minimum in the seismic data.

Appendix B: Single Trace Attributes

Instantaneous Attributes

Based on complex seismic trace analysis, instantaneous attributes are computed sample by sample to represent instantaneous variations of assorted properties of seismic data (Taner, 2001). According to White (1991), the three main attributes are instantaneous envelope which gives the strength of a reflection, instantaneous phase which gives the polarity of the data and symmetry of the wavelet, and instantaneous frequency, which represents the average spectrum of an isolated wavelet.

Instantaneous attributes are based on the analytic or "complex" trace. Taner (1979) describes a complex seismic trace as conveying both the real and imaginary components of a seismic trace, whereas the conventional seismic trace only conveys the real information. This real information is what commonly comes to one's mind when visualizing a seismic attribute – squiggles at a given receiver location recording two way traveltime. Figure 66 reproduces Taner's (1979) cartoon of a complex trace, and shows wave motion outside of the 2 dimensional plane in which a seismic trace is commonly considered. Defining the complex trace as

$$\hat{x}(t) = x(t) + iH[(t)] = x_R(t) + ix_I(t)\ , \tag{B1}$$

the instantaneous envelope is defined as

$$e(t) = \sqrt{x(t)^2 + H[x(t)]^2}\quad , \tag{B2}$$

the instantaneous phase as

$$\varphi(t) = \tan^{-1}\frac{\widehat{x_I}(t)}{\hat{x}_R(t)}, \tag{B3}$$

And the instantaneous frequency as

$$\hat{\omega} = 2\pi\hat{f}(t) = \frac{d}{dt}\varphi(t) \ . \quad \text{(B4)}$$

One more often used instantaneous attribute is RMS amplitude which is defined as

$$RMS = \sqrt{\frac{x_n(t)^2 + H_n[x(t)]^2}{N}} \quad \text{(B5)}$$

where N is the number of samples in a defined window.

The Hilbert transform in equation 1 is a 90° phase rotation of the measured (or real) seismic trace, or "quadrature" representation of a seismic trace. This rotation represents the imaginary portion of a seismic trace, and when the real and Hilbert transformed (imaginary) portion of the seismic trace are summed this represents the entirety of the data represented in a seismic trace.

The instantaneous envelope of a seismic trace calculated at a specific time, t, is represented in equation 2. If the relationship between the real and imaginary portions of a seismic trace can be thought of as a triangle, then instantaneous envelope can represent an implementation of Pythagorean's theorem. In this sense, the instantaneous envelope is equal to the magnitude of the vector between the real and imaginary components of the seismic trace, or the absolute value of the magnitude of the real and imaginary components of the seismic trace.

Using the same triangle analogy, the instantaneous phase would represent the angle between the vector of real portion of the seismic trace, *x(t)*, and the imaginary portion, *H[x(t)]*. The equation for instantaneous frequency is shown in equation 4. Instantaneous frequency is simply the derivative of the instantaneous phase. In simpler terms, the frequency is the measure of how often a full cycle of the waveform occurs. It is easy for one to dismiss calculations related to the imaginary portion of data as irrelevant. However, in an effort to validate the physical connection of instantaneous

attributes, Ulrych et al. (2007) define the wave equation. Ulrych et al. state that the disturbance of the wavefield of a seismic source convolved with the Green's function can be represented as a function of the instantaneous envelope and instantaneous phase. Ulrych et al. cite this relationship as proof that instantaneous attributes are "not merely the result of a clever mathematical trick via the Hilbert transform".

Further, White (1991) provides applicable relationships of instantaneous attributes in regards to gas hydrocarbon reservoirs. In particular, White uses characteristics of instantaneous attributes to define the extent of gas hydrocarbon reservoirs. For example, because of the obvious reflection coefficient change, a strong seismic reflection would be expected at the top of a gas sand and thus a fair approximation of the phase of the seismic wavelet would be represented. At the lateral extents of the gas sand reservoir where water becomes a more common pore fluid than the gas, the instantaneous phase and envelope would change. Expected instantaneous envelopes of water filled sands are less than gas sands, and as the shift from gas to water occurs, the phase response will become complicated and less representative of the seismic wavelet. The weaker reflection of the water filled sand will not represent the phase content as well.

Because these attributes are only computed with regards to a single trace (although both real and imaginary components), they have not spatial dependency. The lack of spatial dependency will allow for correct calculation in both 2D and 3D seismic volumes, without variations between the datasets.

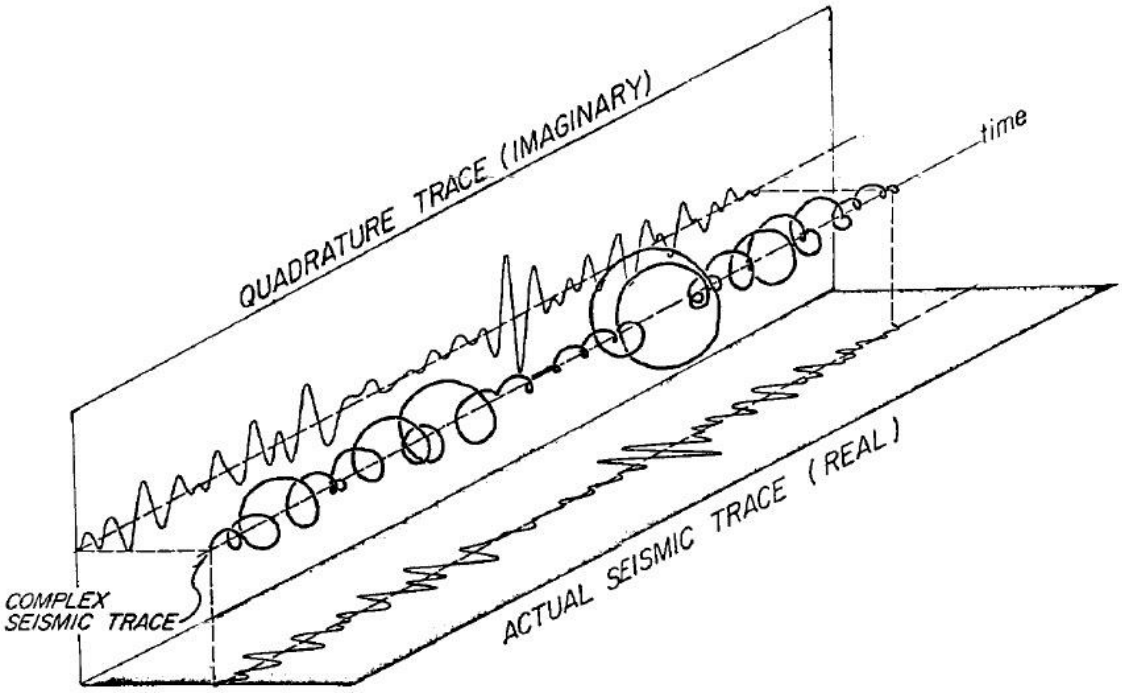

Figure 66. Complex trace as depicted by Taner (1979).

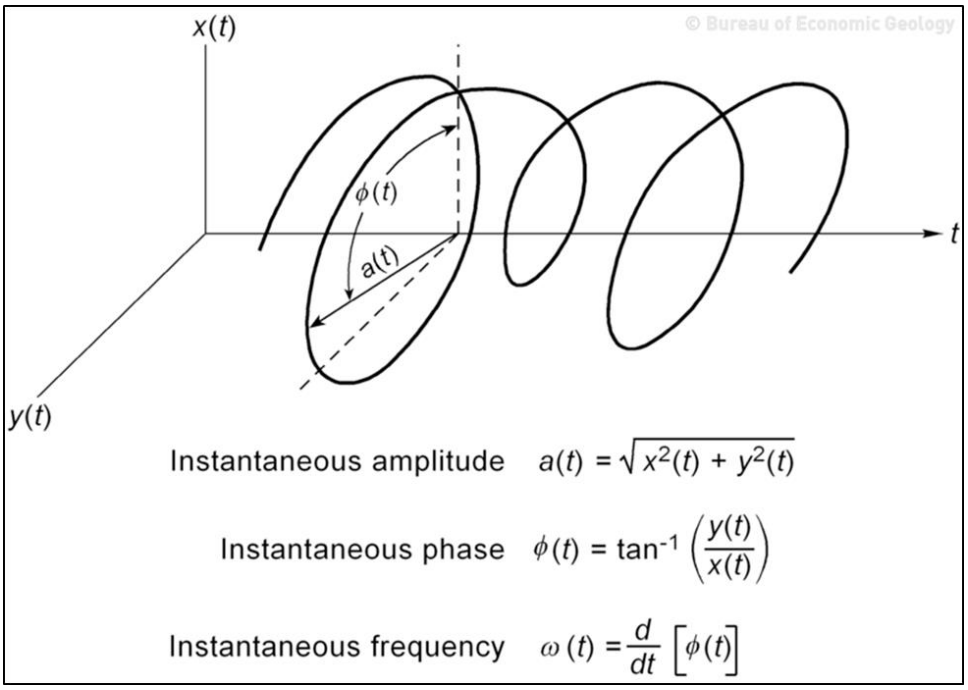

Figure 67. An additional image of the complex trace from the Hardage (1996). This cartoon builds upon Taner's image by showing the relationship between instantaneous attributes in multi-dimensional space.

Spectral Decomposition

Two primary methods are available for spectral decomposition, the short window discrete Fourier transform (SWDFT) and the continuous wavelet transform (CWT). The main differentiator between the two is the window size, which is constant for all frequencies in SWDFT and varies in CWT. In SWDFT, a fixed-length analysis window is used for all frequencies to determine what the dominant frequency component is in a geologic formation. The short window discrete Fourier transform (SWDFT) is ideal for formation based attributes, such as estimating tuning thickness and stratigraphic variability (Chopra and Marfurt, 2007). Because of data reconstruction and minimal mixing of temporally separate events, the CWT is thought of as the best method for evaluating direct hydrocarbon indicators, seismic-attenuation, and enhancement of seismic bandwidth. Since spectral decomposition only includes calculations on the seismic trace and Hilbert transformed complex trace it should work equally well on 2D and 3D seismic data.

Post Stack Impedance Inversion

The traditional convolution of a seismic wavelet with a reflectivity series is shown in Figure . This commonly understood process represents the opposite of the inversion process. Seismic inversion is used to determine the acoustic impedance of individual layers, in particular, in an effort to replicate the broader frequency bandwidth of the well log data, impedance inversion is performed on seismic data. Most inversion methods are based on sparse spike, or parametric, inversion. Colored inversion will be used in this research. Sparse spike inversion provides the basis for colored inversion. One of the primary assumptions of colored inversion is that sparse spike inversion can

be modeled by a convolution. In colored inversion, the seismic is convolved with an operator wavelet that converts the seismic spectrum to the Earth's acoustic impedance spectrum as recorded in well logs. Colored inversion is a swift option to extract an acoustic impedance volume from the seismic data volume. Petrophysical properties like V_p, V_s, and density can be calculated from the acoustic impedance volume. Additional benefits of inversion include mitigation of the effects of the seismic wavelet in the seismic bandwidth, possibility of extending beyond the seismic bandwidth because of the larger bandwidth of the well data, and improved stratigraphic interpretation.

In general, seismic inversion can best be broken down into four steps. First a model is formulated based on the initial estimate of parameters. Next, a function is derived to emphasize the differences between the current model and the desired model. Then the model is updated to better resemble the desired model and multiple iterations are run until the error reaches an acceptable minimal level. Colored inversion is a simplified version of this general process. Colored inversion requires merely extracting the frequency spectrum for the seismic data over an interval of interest then extracting the spectrum of the well logs. Next a convolution operator is defined to convolve the seismic frequency to closely resemble the spectrum of the well logs.

Colored inversion is of particular use because it is a much quicker process than traditional sparse spike inversion methods, and it has been shown to have comparable results. Only one inversion operator is derived and it globally honors the well log data. One potential downfall of colored inversion is that the data is assumed to be zero phase, which is not usually the case.

A low pass filter is applied to the data to ensure that the detailed results are coming from the seismic and not the well logs.

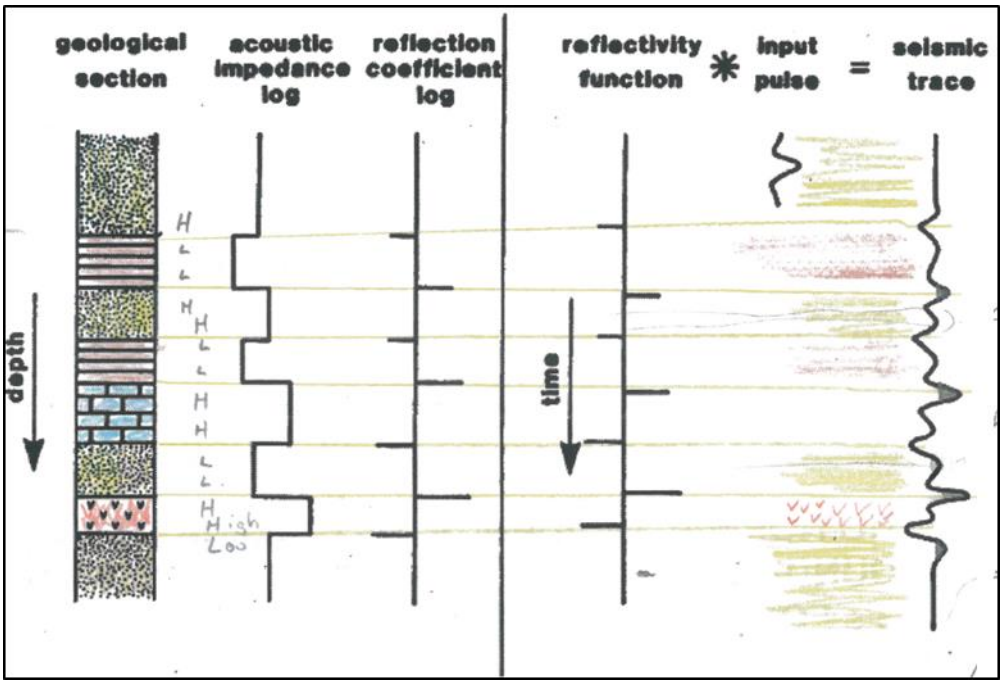

Figure B3. A depiction of the convolution of a wavelet with a reflectivity series to form a seismic trace. Modified from Pigott (2015).

Appendix C: Multi-trace Attributes

Multi-trace attributes are also commonly referred to as “geometric attributes”.

Dip Azimuth and Dip Magnitude

The dip and azimuth of a planar seismic reflector can be quantified by a point in space and a unit normal to that surface (Chopra and Marfurt, 2006). Dip magnitude and dip azimuth are calculated in seismic data as apparent dip components along the inline and crossline direction. Dip azimuth is measured clockwise from North, which is the y-axis defined in the SEGY header . An overlapping search window method (Marfurt, 2006) is used to define the dip of the reflector for dip calculations. This method is described in further detail in the Data Conditioning chapter.

For 2D lines, there is only one apparent dip, such that one can find neither the true dip magnitude nor dip azimuth. However, 2D lines are usually designed to acquire a grid of lines oriented parallel and perpendicular to the regional dip azimuth. This is apparent in the 2D lines in Figure 9 which show the high dipping angle of the Pohokura structure.

In the Pohukura 3D, the inline and crossline reflector dip was initially overprinted by the dip relationships of moderate amplitude crosscutting noise. I evaluated multiple window sizes to determine which size best captures the true dip of the reflected signal with the ±0.040 s by 12.5 m radius window size provide a good balance between increasing signal-to-noise ratio while preserving lateral and vertical resolution. This window is a little bit greater than twice as large as the “optimum” window containing a full dominant period (29 ms for a dominant period of 35 Hz) and therefore vertically smooths over short wavelength vertical changes of dip.

Curvature

Curvature is a second derivative of a time surface. The curvature attribute is known to exacerbate acquisition footprint and random seismic noise. Curvature defines how curved a seismic surface is, it is good for highlighting faults, anticlines, synclines, and other curved geologic features seen in seismic data. Measurements of curvature are symmetric about zero. Positive measures of curvature are related to anticlines and synclines are defined by negative curvature values.

According to Chopra and Marfurt (2006), in three dimensions, the first step in mathematically defining curvature is by using least squares fitting to estimate a quadratic surface, z(x,y), of the form

$$z(x,y) = ax^2 + cwy + by^2 + dx + ey + f, \quad \text{(C1)}$$

to an interpreted horizon. From Roberts (2001), the mean curvature:

$$k_{mean} = [a(1+e^2) + b(1+d^2) - cde]/(1+d^2+e^2)^{\frac{3}{2}}, \quad \text{(C2)}$$

and the Gaussian curvature:

$$k_{Gaussian} = (4ab - c^2)/(1+d^2+e^2)^2, \quad \text{(C3)}$$

are used to define the principle curvatures:

$$k_1 = k_{mean} + ({k_{mean}}^2 - k_{Gaussian})^{\frac{1}{2}}, \quad \text{(C4)}$$

$$k_2 = k_{mean} - ({k_{mean}}^2 - k_{Gaussian})^{\frac{1}{2}}. \quad \text{(C5)}$$

Multiple types of curvature are calculated and interrelated to each other, understanding the difference in these is critical to understanding what value curvature can provide to 2D seismic data lines. First, the principal curvatures (k_1 and k_2) are

k_{max} and k_{min} are defined by measuring the radius of vertical circles. K_{max} is defined by the radius of the smallest circle that can outline the curved structure. K_{min} is defined by a circle perpendicular to the circle that defines k_{max} and always has a radius larger than or equal to that of k_{max}. The maximum curvature, k_{max}, is the principal curvature which has the largest absolute value. Dip curvature and strike curvature are also defined by Chopra and Marfurt (2006). We will look at the k_1, most positive, and k_2, most negative curvature in this research, to ascertain the boundaries of a hydrocarbon accumulation. In 2D seismic lines, only the apparent curvature can be calculated.

Euler Curvature

Euler curvature is simply the apparent curvature in a given azimuthal direction, and hence the curvature measured on a 2D seismic line. As defined by

$$k\psi' = k_1\cos^2(\psi' - \psi'_2) + k_2 \sin^2(\psi' - \psi'_2) \quad \text{(C6)}$$

where ψ' represents the azimuth of choice, and k_1 and k_2 are principal curvatures with corresponding azimuths.

Reflector Convergence

One of the first steps in seismic stratigraphic interpretation is picking reflector terminations. Onlap, downlap, and offlap, are key in deciphering progradational from transgressive packages in the stratigraphic environment. These seismic stratigraphic features were first quantified by Barnes (2000). Barnes showed convergence and divergence of reflectors with a color bar where blue represents convergence and divergence (or negative convergence) is shown in yellow.

Convergence is a vector, just like dip and azimuth. As such, one can only measure apparent reflector convergence on a 2D seismic line.

Coherence

Coherence or similarity is a measure of the consistency of the waveform from trace to trace. Accurate calculations of coherence require computation along local dip and azimuth. Two main types of coherence were used in this study. Those are energy ratio similarity and Sobel filter similarity.

Energy ratio similarity gives results similar to that of an eigenstructure coherence algorithm. Eigenstructure coherence, in the simplest terms, is a ratio of the energy of the coherent component of seismic data to the original traces within a specified analysis window (Chopra and Marfurt, 2007). For 3D seismic data, the analysis window includes traces centered around the analysis point. In 2D seismic data, the analysis window will only exist in the plane of the data. Energy ratio similarity is computed along structure and, similar to instantaneous attributes, is compute using both the real and complex seismic trace.

The Sobel filter has been traditionally applied in photography, but Luo et al. (1996) modified the filter to work with seismic data. They first took the derivatives along a plane defined using reflector dip and azimuth. Next, they stacked the derivatives in a vertical window to improve the signal to noise ratio. Finally they normalized the stacked trace by dividing by the energy of the input trace, to normalize the result to local amplitude variation rather than absolute amplitude variation (Chopra and Marfurt, 2007).

Amplitude Gradients

Coherent amplitude gradients are calculated using eigenstructure techniques applied in coherence calculations and structural oriented filtering. The first step is to

calculate the energy of the input traces in the analysis window. Next a waveform that best approximates the waveform of each input trace is calculated. Then each trace is replaced with a scaled version of the average waveform that best fits each input trace of the analysis window. The amplitudes of the traces in the analysis window make up the components of a principal-component eigenvector. In fact the concept of amplitude gradients is based in 2D as seen in Figure 68.

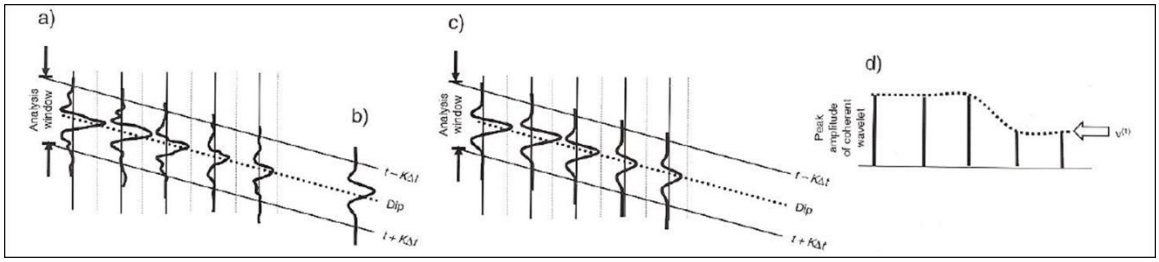

Figure 68. Computation of the principal-component eigenvector for amplitude gradient analysis. In (a) the energy of the traces in a centered analysis window in 2D is calculated, (b) shows the seismic waveform that best approximates the waveform of each input trace. In (c) each trace in the analysis window is replaced by a scaled version of (b) that best matches the each individual trace amplitude in the analysis window. Shown in (d) is the peak amplitude of each coherent wavelet in the analysis window. The energy-weighted coherent-amplitude gradient is then calculated by taking the derivative of the curve shown by the dotted line. That derivative is then weighted by the sum of the coherent energy in the analysis window. From Chopra and Marfurt (2007).